HELSINKI INSTITUTE OF PHYSICS INTERNAL REPORT SERIES

HIP – 2005 – 01

MULTISCALE MODELING OF BIOLOGICAL AND SOFT MATTER

EMMA FALCK

Laboratory of Physics and Helsinki Institute of Physics
Helsinki University of Technology
Espoo, Finland

Academic Dissertation

Dissertation for the degree of Doctor of Science in Technology to be presented with due permission for public examination and debate in Auditorium E at Helsinki University of Technology (Espoo, Finland) on the 15th of March, 2005, at 12 o'clock noon.

Helsinki 2005

ISBN 952-10-1687-6 (print)
ISBN 952-10-1688-4 (electronic)
ISSN 1455-0563
Helsinki 2005
Yliopistopaino

Abstract

The large range of spatial and temporal scales inherent in biological and soft matter is a challenge to modeling. To understand the physics of a cell membrane, one needs to start from Ångström-sized atoms and their motions in the femtosecond range, and go all the way to whole cells, whose diameters can be tens of micrometers and lifetimes of the order of days. All these scales can neither be probed by a single experimental technique, nor modeled using one simulation approach. What is needed is a range of techniques.

Describing matter by a hierarchy of computational models, systematically linking the models at lower resolution to those at higher resolution, is termed multiscale modeling. Depending on the phenomenon one wishes to study, one may choose atomic-level models and algorithms, opt for a simplified or coarse-grained description, or decide on a combination of these. The aim of this Thesis is to describe modeling at atomic scale and mesoscale, i.e., at scales in the range 1–1000 nm and 1–1000 ns. We also focus on the systematic linking; how to reduce the degrees of freedom in an atomic-scale model to arrive at a coarse-grained description. Further, use of hybrid models that combine atomic and coarse-grained descriptions is discussed.

We approach multiscale modeling through examples from biological and soft matter physics. Atomic-scale modeling is illustrated through molecular dynamics simulations of phospholipid/cholesterol bilayers. The effect of cholesterol on the free volume, packing, and diffusive properties of bilayers is investigated. We then link the atomic-scale model to one allowing us to reach length scales significantly larger than those reached in current-day state-of-the-art atomic-level simulations: the new model offers an eight-order-of-magnitude speed-up, enabling us to study the lateral structure of bilayers at length scales up to hundreds of nanometers at a modest computational cost. The simulation results point at the existence of cholesterol-rich domains with sizes in the ten-nanometer-range.

From membrane systems we move to the realm of complex fluids. We use polymer chains and colloids in solution as examples of systems where hybrid models should be used. The solutes are modeled in microscopic detail, while the solvent is coarse-grained. The solvent model is cost-effective, yet correctly describes the hydrodynamic interactions between the solute particles. Using these models we are able to resolve a long-standing debate about dynamic scaling of two-dimensional polymers in solution, and obtain interesting results for collective diffusion in colloidal suspensions.

Preface

The work reported in this Thesis has been carried out at the Laboratory of Physics and Helsinki Institute of Physics at Helsinki University of Technology. I first wish to thank my Thesis supervisors Dr. Ilpo Vattulainen and Prof. Tapio Ala-Nissilä. Ilpo has taught me a lot about the art of computational physics, and drilled me in publishing scientific results and producing attractive grant proposals. Even more important: he has been an excellent role model of a young scientist, showing how optimism, confidence, and hard work may take one a long way. Tapio, besides being a great statistical mechanic and an articulate lecturer, is a man of great integrity.

I also wish to thank all the coauthors of the publications included in this Thesis. Marru's experience and courage, Michael's efficiency, Mikko's mentoring, Olli's analytical talent, and Teemu's talent for just about anything have been much appreciated. My hard-working Thesis pre-examiners, Prof. Kai Nordlund and Prof. Roland Faller, deserve a special thanks for their excellent suggestions and comments. So does Dr. Jones, my orthopedist, who, by means of plica surgery, accelerated the progress of the final stages of this Thesis project.

I have had the pleasure to work in a wonderful group and get to know many fine colleagues. It is therefore in order to extend a thanks to Prof. Risto Nieminen for making COMP such a well-functioning workplace. I would also like to thank all the COMP group members for a creative and friendly working atmosphere. Emma T. and I have had a nice time sharing an office.

The computational resources provided by the Finnish IT Center for Science and the HorseShoe supercluster at the University of Southern Denmark have enabled the extensive studies presented in this Thesis. Financial support from the National Graduate School in Materials Science; the Vilho, Yrjö, and Kalle Väisälä Foundation; Tekniikan Edistämissäätiö; and the Ehrnrooth Foundation is gratefully acknowledged.

Finally, I would like to thank my family for their support. My brave grandmother Kerttu and my dear aunt Maija should really be on the list of financial benefactors. Mum, Dad, and my brother Michael comprise a most fun, athletic, cultivated, and culinary family. My fiance Timo deserves the warmest thanks of all: his patience, intelligence, versatility, and charm have made my time as a PhD student most enjoyable.

Otaniemi, February 2005

Emma Falck

Contents

List of Publications

This thesis consists of an overview and the following publications:

I. E. Falck, O. Punkkinen, I. Vattulainen, and T. Ala-Nissila, *"Dynamics and Scaling of 2D Polymers in a Dilute Solution"*, Phys. Rev. E Rapid Comm. **68**, 050102(R)-1–050102(R)-4 (2003).

II. E. Falck, J. M. Lahtinen, I. Vattulainen, and T. Ala-Nissila, *"Influence of Hydrodynamics on Many-Particle Diffusion in 2D Colloidal Suspensions"*, Eur. Phys. J. E **13**, 267–275 (2004).

III. E. Falck, M. Patra, M. Karttunen, M. T. Hyvönen, and I. Vattulainen, *"Lessons of Slicing Membranes: Interplay of Packing, Free Area, and Lateral Diffusion in Phospholipid/Cholesterol Bilayers"*, Biophys. J. **87**, 1076–1091 (2004).

IV. T. Murtola, E. Falck, M. Patra, M. Karttunen, and I. Vattulainen, *"Coarse-Grained Model for Phospholipid/Cholesterol Bilayers"*, J. Chem. Phys. **121**, 9156–9165 (2004).

V. E. Falck, M. Patra, M. Karttunen, M. T. Hyvönen, and I. Vattulainen, *"Impact of Cholesterol on Voids in Phospholipid Bilayers"*, J. Chem. Phys. **121**, 12676–12689 (2004).

The author has played an active role in all stages of the research reported in this Thesis.

Publication I was co-authored by Olli Punkkinen, Ilpo Vattulainen, and Tapio Ala-Nissila. The author participated in the planning of the simulations, developed the necessary simulation and analysis tools, conducted the major part of the simulations, and analyzed and interpreted the results. In addition, she participated in the analytical work, the major part of which was Olli Punkkinen's. The first draft of Publication I was written by the author.

Publication II was co-authored by Jukka Lahtinen, Ilpo Vattulainen, and Tapio Ala-Nissila. The author played an important role in designing the computer experiments. The simulation software and part of the analysis tools were the author's. She ran test simulations of the solvent model

necessary for the actual experiments with colloids, and participated actively in the interpretation of the results. The first draft of the manuscript was written by the author and Jukka Lahtinen.

Publication III was co-authored by Michael Patra, Mikko Karttunen, Marja Hyvönen, and Ilpo Vattulainen. The atomic-scale molecular dynamic simulation data used in this Publication, as well as Publications IV and V, was contributed by Michael Patra. The author planned the free area and packing analysis, implemented the necessary software tools, performed the analysis, and interpreted the results. The first draft of Publication III was written by the author.

Publication IV was co-authored by Teemu Murtola, Michael Patra, Mikko Karttunen, and Ilpo Vattulainen. The author calculated the radial distribution functions used as starting point for coarse-graining. She wrote and tested the Inverse Monte Carlo (IMC) code for coarse-graining membrane systems, and implemented the Monte Carlo code for large-scale simulations of coarse-grained systems, including part of the analysis tools. She supervised the work of Teemu Murtola, who conducted most of the production runs and data analysis. The author participated in the interpretation of the results of both IMC and MC runs and played an active role in writing the manuscript. The first draft of the manuscript was written by Teemu Murtola.

Publication V was co-authored by Michael Patra, Mikko Karttunen, Marja Hyvönen, and Ilpo Vattulainen. The idea to extend the free area analysis to the detailed properties of the voids was the author's. She designed and implemented the necessary software tools for detecting and characterizing voids, performed the analysis, an interpreted the results. Publication V was written by the author.

In addition to these Publications, the author has participated in research described in Refs. [1–4]. These studies are related to Publications I–V.

List of Abbreviations

BD	Brownian dynamics
CM	center of mass
DLPE	dilauroylphosphatidylethanolamine
DMPC	dimyristoylphosphatidylcholine
DMTAP	dimyristoyltrimethylammoniumpropane
DOPC	dioleylphosphatidylcholine
DOPE	dioleylphosphatidylethanolamine
DPD	dissipative particle dynamics
DPPC	dipalmitoylphosphatidylcholine
DPPS	dipalmitoylphosphatidylserine
DPhPC	diphytanoylphosphatidylcholine
FCS	fluorescence correlation spectroscopy
FRAP	fluorescence recovery after photobleaching
IMC	inverse Monte Carlo
LJ	Lennard-Jones
MC	Monte Carlo
MD	molecular dynamics
NEMD	non-equilibrium molecular dynamics
NMR	nuclear magnetic resonance
PC	phosphatidylcholine
PCA	principal component analysis
PE	phosphatidylethanolamine
PME	particle mesh Ewald
POPC	palmitoyloleylphosphatidylcholine
POPS	palmitoyloleylphosphatidylserine
QENS	quasi-elastic neutron scattering
QM	quantum mechanical
RDF	radial distribution function
SPC	simple point charge
SRD	stochastic rotation dynamics

1

Introduction

Biological systems feature a multitude of spatial and temporal scales. Cell membranes [5] are a case in point. Membranes are thin, flexible sheets consisting of different kinds of lipid and protein molecules. They are found in various parts of the cell, perhaps the most prominent one being the plasma membrane surrounding the cell. A quick illustration of the length scales in membrane systems is provided by the dimensions of a typical plasma membrane: the membrane itself is approximately five nanometers thick, but it may be wrapped around a cell whose diameter is of the order of tens of micrometers or more. The separation of time scales is equally impressive, ranging from molecular bond vibrations at picosecond time scale to a few days or longer, a typical life time of a cell.

Understanding membrane structure gives more insight into the *length scales* encountered in membrane systems. At atomic level, their most important building blocks are the Ångström-sized atoms of carbon, hydrogen, oxygen, nitrogen, and phosphorus. Atoms make up molecules: at molecular level cell membranes are comprised of lipids and proteins [5]. These molecules can be rather large, consisting of hundreds or thousands of atoms. The molecules are thought to exhibit lateral long-range ordering; according to the so-called raft hypothesis [6–9], they are organized in rafts, whose dimensions are believed to range from tens to hundreds of nanometers. Rafts have been suggested to be dynamic, ordered, lateral domains rich in saturated glycerophospolipids, sphingomyelin, and cholesterol. Membrane proteins are believed to attach to or be embedded in rafts to perform various important tasks in transport and signaling.

Lateral diffusion of lipids in membranes [10] provides a more detailed example of the manifold of *time scales* in biological systems. The fastest local motions of whole lipids are dubbed rattling-in-a-cage; the lipid molecule vibrates in a cage formed by its neighbors. The length scales

associated with this motion are less than the size of the lipid and the time scales of the order of nanoseconds. The lipids may jump from one cage to another: at time scales between 1 and 100 ns we expect to observe jump diffusion within a single domain. This motion is intermediate-time diffusion. At time scales of the order of microseconds, or larger, lipids may cross domain boundaries or encounter networks of proteins. This is true long-time diffusion.

Experimentalists measure lateral diffusion of lipids using a variety of techniques, e.g., quasi-elastic neutron scattering (QENS) [11, 12], fluorescence correlation spectroscopy (FCS) [13], and fluorescence recovery after photobleaching (FRAP) [14, 15]. Each of these techniques has a certain resolution; different techniques are used to explore diffusion at different spatial and temporal scales. Together they cover the range of motions from the fast rattling-in-a-cage movement to the slower long-time jump diffusion over domain boundaries. As motions at sub-nanosecond time scales are much faster than those at the microsecond time scale, the different experimental techniques yield lateral diffusion coefficients that may differ by several orders of magnitude [10].

QENS is a microscopic technique, covering time scales of a few nanoseconds at most. Hence, QENS experiments probe the fast rattling-in-a-cage movement and yield high values for the lateral diffusion coefficient. FRAP, on the other hand, cannot be used for studies of short-time diffusion: its spatial resolution is of the order of 100 nm and the temporal resolution 100 ns. The same applies for FCS, the spatial resolution being approximately 50 nm and the temporal resolution 5 ms. FCS and FRAP are therefore more macroscopic methods that probe intermediate- and long-time diffusion. These are typically much slower than the local rattling-in-a-cage movement [10]. It is not a fundamental problem that diffusion coefficients measured using different techniques differ. It is, however, important to keep this in mind when comparing results from different studies.

There are other much more severe reasons for the interpretation of diffusion experiments being problematic, see Ref. [10]. As an example, many techniques rely on attaching bulky molecules to the lipids: pyrene molecules are often linked to the hydrocarbon chains of the lipids or large colloidal particles with diameters of the order of tens of nanometers to the lipid headgroup. These molecules allow experimentalist to track the motion of the lipids, e.g., pyrenes are fluorescent. The downside is that it is not clear how a probe such as pyrene really affects the lateral diffusion of lipids.

It is quite plausible that a substantial probe molecule significantly slows down diffusion. Even worse, the pyrene molecules may alter the microscopic diffusion mechanisms of the lipid molecules. How does an experimentalist find out whether the microscopic diffusion mechanisms are affected, or indeed, what those mechanisms are in the first place?

Computer modeling [16–18] offers solutions to these dilemmas. A computer simulation typically results in a trajectory for the system being studied, i.e., the velocities and positions of the particles comprising the system as functions of time. In principle, any structural or dynamic quantity, e.g., the lateral diffusion coefficient, can be extracted from this trajectory. In addition to providing access to averages, trajectories reveal the microscopic mechanisms behind experimental phenomena, say, how a lipid jumps from one cage to another. Such microscopic information cannot be accessed in experiments, at least not directly.

Computer modeling is not only a tool for interpreting experimental results. It definitely has predictive power of its own [17, 18]: novel phenomena first observed in simulations can be verified in experiments. It also allows one to try things impossible to realize in experiments. Studying the role of hydrodynamic or solvent-mediated interactions in colloidal systems, see Chapter 4, is an example of such a case. Ideally, one should compare two otherwise similar colloidal systems, but with and without hydrodynamic interactions. Switching off the hydrodynamic interactions in an experimental setup with colloidal particles immersed in a solvent is not possible. In a computer simulation, hydrodynamic interactions can easily be switched on and off.

The wide range of spatial and temporal scales in soft and biological systems is a challenge to modelers. As in experiments, structures and phenomena at different scales should be studied using different computational techniques. It is neither feasible nor sensible to study, e.g., the long-time lateral diffusion of lipids in membranes using quantum mechanical (QM) simulation methods, see Chapter 2. Depending on the approximations used, state-of-the-art QM simulations would enable one to follow at most 10^4 atoms during a few picoseconds [18]. Such a simulation would be very expensive, but a far cry from the 10^6 atoms and several microseconds needed in studies of long-time diffusion. Even if future computers did allow us to use QM methods to study large enough systems for times long enough, QM simulations would in this case be largely pointless. That is because most of the relevant physics involved here can be captured by a classical description. Using the finest

possible detail without any discretion is a very bad idea: the design of models and choice of techniques should be tailor-made for each separate problem.

Tailoring the models and methods to each specific system and carefully considering the desired level of accuracy may sound simple. In practise, it is not. As an example, suppose we should wish to study the raft hypothesis presented above. We would need an at least micron-sized patch of membrane with phospholipids, sphingolipids, and cholesterol, surrounded by a substantial number of water molecules. Proteins might be nice to include, as well. With state-of the-art computers, there is no way we could afford to use a classical atomistic description: the computational load would be simply enormous. A possible solution would be to try to reduce the degrees of freedom by modeling the molecules by, e.g., interacting point-like particles, see Chapter 3. How should these point-like molecules interact with each other? Would it be better to include a few more degrees of freedom by letting each molecule consist of a number of point-like particles attached to each other? What about the form of interactions in such a model?

Coarse-graining is the term used for moving from one level of accuracy to another. As in the raft example, we may wish to progress from a microscopic all-atom description to a simplified description where the interacting units may consist of tens of atoms. The physicist's dream is to start from electron densities and smoothly, level by level, go all the way to interacting elephants. This should be realized in a controlled fashion such that at each level the essential physics and chemistry are included, but most of the unnecessary detail is discarded. Systematically linking different levels of description and using these to model condensed matter has a fashionable name, *multiscale modeling*.

Practitioners of multiscale modeling are bound to encounter systems with parts that need to be considered using fine detail, while a large portion of the system could be treated in a less accurate manner. These situations are particularly challenging, since in most cases it is quite intractable to include the whole system in the more detailed description. An example of such a case is studying the dynamics of polymers or proteins in solution, see Chapter 4. The detailed interactions between the monomers constituting the biopolymer may be very important: certain monomers could be hydrophobic and others hydrophilic, and this should have an impact on the physics of our model. As for the solvent, simulating its detailed dynamics is very expensive and rather uninteresting. The solvent cannot be left out

completely, since the solvent-mediated hydrodynamic interactions between the monomers are very important for the dynamics of the polymer [19]. A solution to this kind of problems is to use so-called *hybrid models*, where two or more descriptions with different levels of accuracy are combined. In the case of the polymer in solution, we may wish to carefully include the direct monomer-monomer and monomer-solvent interactions in our model and take care of the solvent-solvent interactions in an effective, less accurate manner, see Chapter 4 for details. An interesting challenge would be to study a protein, most of which could be described by a classical atomistic model, and a few details, whose electronic degrees of freedom could not be neglected, should be modeled quantum mechanically. In addition, there would be a more coarse-grained solvent.

This Thesis is about modeling biological and soft systems by means of computer simulations. Modeling of soft condensed matter at different spatial and temporal scales is illustrated through case studies. There are examples of atomistic modeling, systematic coarse-graining, and hybrid models. Part of the emphasis will be on model design; the advantages and limitations of each model will be considered. Another important theme is the analysis and interpretation of simulation results.

Chapter 2 deals with classical atomistic modeling, and in particular, atomic-level modeling of lipid membranes. We will first recount the basics of classical molecular mechanics in biological systems [18], i.e., describe the use and origins of force fields employed in state-of-the-art simulations of membranes. A brief description of the classical molecular dynamics method follows. After an account of the current research focus in computational modeling of membrane systems, we will describe our case study into classical atomic-level membrane modeling, a study of the effects of cholesterol on the free volume and related properties of phospholipid bilayers. Our first contribution here is systematically studying the impact of cholesterol on the free volume, packing, and diffusive properties of phospholipid bilayers, and probing the validity of simple free area theories for lateral diffusion of lipids. The second main contribution is a careful analysis of the effect of cholesterol on the detailed structure of the free volume pockets or voids in phospholipid bilayers.

The atomistic models introduced in Chapter 2 do not allow us to explore very large bilayer systems; as explained above, studying structures with linear sizes larger than tens of nanometers is at least currently out of the question. To study large-scale ordering or domains, we need a model with

fewer degrees of freedom. This model is obtained from the atomistic model used in Chapter 2 by systematic coarse-graining.

Chapter 3 is about coarse-graining in membrane systems, with emphasis on systematic approaches. We will first sketch some of the basic principles of coarse-graining. This sketch is followed by a survey of the latest developments in the use of coarse-grained models in studies of membrane systems. Next, a promising method for systematic coarse-graining in soft condensed matter, inverse Monte Carlo (IMC) [20], is presented. The case study in this Chapter is an application of the IMC technique to systematically coarse-grain the atomistic phospholipid/cholesterol system from Chapter 2. We will describe the construction, validation, and application of the coarse-grained model. The main contributions here are the first application of IMC in membrane systems, and the construction of a coarse-grained model for phospholipid/cholesterol systems, easily applicable to large-scale studies in the hundred-nanometer-range. At certain cholesterol concentrations we observe cholesterol-rich domains.

The themes of Chapter 4 are coarse-grained dynamics and hybrid models. The basic question in this Chapter is how to study the dynamics of molecules immersed in solvents. As explained above, simulating the details of solvent motion is expensive and often unnecessary, but the hydrodynamic interactions between the solvated molecules should be described in a correct manner. A solution is a hybrid model where the solute is described in detail and the solvent in a less accurate fashion using a novel solvent model called stochastic rotation dynamics (SRD) [21]. The Chapter contains an introduction to SRD and its hybrid extension, so-called MD/SRD [22]. The two case studies presented in this Chapter are of very generic models, and the results applicable to a wide range of systems. We will first discuss the dynamics of a two-dimensional polymer in solution, followed by a description of studies into the dynamics of a related system, a two-dimensional colloidal suspension. These are a few of the first attempts to use the novel MD/SRD model to solve real, albeit rather generic and theoretical, problems. In addition to this testing and validation aspect, an important contribution here is solving the dispute on dynamic scaling in two-dimensional dilute polymer solutions. We also obtain interesting preliminary results for the effect of hydrodynamic interactions on collective diffusion in colloidal suspensions.

2

Microscopic Modeling

2.1 From Quantum to Classical

In the non-relativistic limit, we could study the nuclei and electrons in any molecular system by writing down a suitable Hamiltonian for the system and subsequently solving the corresponding Schrödinger equation. Quantum mechanical (QM) simulation methods are based on this seemingly simple idea. Unfortunately, brute-force solution of the Schrödinger equation, where the nucleic and electronic degrees of freedom are coupled, is prohibitively expensive [18]. Present-day QM simulations are based on the so-called Born-Oppenheimer approximation: the motion of the heavy, slow nuclei and the light, fast electrons are separated. Depending on the additional approximations used, QM simulations come in two major flavors; there are ab initio and semi-empirical calculations.

Examples of biologically relevant QM calculations include, among other things, studies of vancomycin resistance in bacteria [23] and a description of the HIV-1 protease cleavage site [24], see Refs. [18, 24–26] for further examples. The major drawback of such studies is their, despite the approximations, still enormous computational expense. The largest systems that can be currently studied using ab initio methods are of the order of 10^3 atoms, while semi-empirical models may be extended to systems with 10^4 atoms. The time scales reached in QM simulations, 1–10 ps, are likewise much shorter than one should hope for. For these reasons it is unrealistic, using bare QM methods, to include solvent molecules in the vancomycin resistance model, or to simulate the reaction mechanisms of the HIV-1 protease [24].

Because of their computational requirements, QM methods should be used only when necessary, i.e., in modeling processes where electronic degrees of

freedom cannot be neglected. In all other cases, the electronic degrees of freedom are integrated out, and the description becomes classical; the basic building blocks are now atoms and ions. Large systems where both a QM description for part of the system and long time scales are necessary, can in some cases be handled by a combined QM and classical approach, see Refs. [18, 24, 25, 27].

This Chapter deals with modeling classical many-body systems, with emphasis on classical atomic-scale simulations of membrane systems. After an introduction to the basic principles of classical modeling, we will describe the state of the art of atomic-scale membrane modeling. We will then proceed to introduce the DPPC/cholesterol system as an example of current modeling efforts in lipid membrane systems. Here the focus will be on packing, free volume, and diffusion in lipid bilayers, and the impact of cholesterol on these.

2.2 Force Fields

In classical modeling the quantum effects are implicit in the intramolecular and intermolecular interactions. The underlying idea is to describe a molecular system in terms of a potential energy or force field, which is a function of the atomic positions. The form of the force field, as well as the associated parameter values, must be chosen to capture the essential physics of the system. Ideally, each term in the force field has an intuitive physical meaning.

A potential energy describing a molecular model can be written as a sum of different contributions [18, 28]:

$$E = E_{\mathrm{bond-length}} + E_{\mathrm{bond-angle}} + E_{\mathrm{torsional}} + E_{\mathrm{Lennard-Jones}} + E_{\mathrm{Coulomb}}. \quad (2.1)$$

This is a simple example where, e.g., cross terms, polarization effects, and the effect of external fields have been omitted, see Refs. [18, 28] for details. The first three terms represent so-called bonded interactions, and the latter two represent non-bonded interactions. The exact form of the terms in Eq. (2.1) may vary. In the following we will describe the physical interpretation of each term, and give examples of commonly used forms. For alternative expressions and additional terms, see Refs. [18, 28].

Bonded interactions are based on a fixed list of atoms. The bond-length interactions control bond deformations and can, as a first approximation, be described by harmonic springs,

$$E_{\mathrm{bond-length}} = \sum_{i,j} \frac{k_{ij}^{\mathrm{b}}}{2} \left(r_{ij} - b_{ij}\right)^2 , \tag{2.2}$$

where r_{ij} is the distance between the atoms i and j, k_{ij}^{b} is a spring constant, and b_{ij} a reference bond-length value. The sum is taken over the set of all bonds.

The bond-angle term governs the bond angle arrangements around atoms and contains three-body interactions. It can be written as a sum of harmonic potentials,

$$E_{\mathrm{bond-angle}} = \sum_{i,j,k} \frac{k_{ijk}^{\theta}}{2} \left(\theta_{ijk} - \theta_{ijk}^{0}\right)^2 , \tag{2.3}$$

where θ_{ijk} is the angle formed by atoms i, j, and k. The sum is taken over all bond angles.

The torsional potential describes the rotational flexibility of sequences of atoms. One formulation for the torsional potential is

$$E_{\mathrm{torsional}} = \sum_{i,j,k,l} \sum_{n} \frac{V_n}{2} \left(1 \pm \cos n\tau_{ijkl}\right) . \tag{2.4}$$

Here τ_{ijkl} is the angle between the planes formed by atoms i, j, and k and atoms j, k, and l. The first sum is over all dihedral angles. Integer n, which typically assumes values between one and three [18], but can be higher in some force fields [18, 29], describes the periodicity of the rotational barrier. V_n is the height of the barrier. There are several other, equally popular, descriptions available, see, e.g., Refs. [18, 28].

Non-bonded interactions are pair-additive in the current force fields. The Lennard-Jones (LJ) term describes the steep short-range repulsion between a pair of atoms, together with an attractive tail attributed to dispersion forces,

$$E_{\mathrm{Lennard-Jones}} = \sum_{i,j} 4\epsilon_{ij} \left[\left(\frac{\sigma_{ij}}{r_{ij}}\right)^{12} - \left(\frac{\sigma_{ij}}{r_{ij}}\right)^{6} \right] . \tag{2.5}$$

The sum runs, in principle, over all pairs of atoms separated by, e.g., at least three bonds [18]. A similar sum appears in the Coulomb term, that

describes the electrostatic interactions between charged particles,

$$E_{\text{Coulomb}} = \sum_{i,j} \frac{q_i q_j}{4\pi\epsilon_0 r_{ij}}, \tag{2.6}$$

where q_i is the effective charge of atom i.

The form of the potential energy function is not enough for the specification of a force field, since Eqs. (2.2)–(2.6) contain a plethora of parameters: b_{ij}, V_n, σ_{ij}, q_i, to mention a few. These should ideally be determined using spectroscopic methods, crystallography, or in some cases QM calculations [18]. For instance the reference values for bond lengths are determined from solved X-ray crystal structures or obtained from QM solutions of equilibrium structures of small molecules. Certain parameters such as those associated with dispersion forces or torsional potentials are supremely difficult to determine [30]. In practice, the patchwork of more or less accurately determined parameters needs to be fine-tuned by comparing the predictions a force field gives for simple systems, e.g., liquid hexadecane, with experimental results. In this manner, so-called effective potentials between the various kinds of atoms in a molecular model are acquired. The potentials are dubbed effective, since they implicitly contain non-bonded many-body interactions, QM contributions, and are, after all, a compromise resulting from simultaneous optimization of several parameters.

Several different force fields are used to describe biologically relevant systems: GROMOS, OPLS, CHARMM, AMBER, and many others. The bad news is that the details—functional form and parameter values—of all these force fields vary. Disappointingly, they do not seem to be converging towards each other [18]. What is more important and very encouraging however is that the different force fields seem to be yielding similar end results. Furthermore, these results are in agreement with experimental data. Current force fields can therefore be considered highly useful, but still far from perfect. The most important limitations, apart from the variability of the force fields, are the treatment of all particles as simple point charges and the limited use of QM information in deriving the force fields, see Refs. [18, 28, 30] for a more comprehensive discussion. Despite the limitations, as Vattulainen and Karttunen point out in Ref. [31], force fields, even though not always valid for accurate quantitative predictions, do give us qualitative insights into the properties of soft condensed matter and help us interpret puzzling experimental results.

2.3 Molecular Dynamics

From a complete force field for a given molecular system, there are several ways to proceed. For instance minimization approaches or basic Metropolis Monte Carlo (MC) can be used to study the equilibrium or static properties of a system with a given force field [16–18]. Molecular dynamics (MD) is the method of choice whenever both static and dynamic quantities at atomic level are being targeted.

The underlying idea of classical MD is simple: Hamilton's equations of motion [32] for the N particles comprising a molecular system with a given force field are solved. If the generalized coordinates are chosen to be the Cartesian components of the positions of the N particles, Hamilton's equations for an assembly of N particles with positions $\{\mathbf{r}_i\}$, momenta $\{\mathbf{p}_i\}$, and masses $\{m_i\}$ can be formulated as follows:

$$\frac{\partial \mathbf{r}_i}{\partial t} = \frac{\mathbf{p}_i}{m_i}, \tag{2.7}$$

$$\frac{\partial \mathbf{p_i}}{\partial t} = \mathbf{F}_i \equiv -\frac{\partial E\left(\{\mathbf{r}_i\}\right)}{\partial \mathbf{r}_i}. \tag{2.8}$$

The total force on particle i, $\mathbf{F}_i$, is computed from the potential energy function $E\left(\{\mathbf{r}_i\}\right)$. The potential energy function is given by Eqs. (2.1)–(2.6) and is a function of the positions of all N particles. Hence, in three dimensions the dynamics of our system is governed by $6N$ coupled first-order differential equations.

A so-called integrator, that means, a finite difference scheme, is needed to numerically solve the set of equations. A reliable choice is an integrator of the Störmer/leap-frog/Verlet type [16–18, 28]. A popular integrator in this class is the so-called velocity Verlet scheme. The positions $\{\mathbf{r}_i\}$ and velocities $\{\mathbf{v}_i\}$ at time t yield series estimates for the corresponding quantities at time $t + \delta t$,

$$\mathbf{r}_i(t+\delta t) = \mathbf{r}_i(t) + \delta t \mathbf{v}_i(t) + \frac{(\delta t)^2}{2m_i}\mathbf{F}_i(t), \tag{2.9}$$

$$\mathbf{v}_i(t+\delta t) = \mathbf{v}_i(t) + \frac{\delta t}{2m_i}\left[\mathbf{F}_i(t) + \mathbf{F}_i(t+\delta t)\right]. \tag{2.10}$$

Starting from $\{\mathbf{r}_i(0)\}$ and $\{\mathbf{v}_i(0)\}$, the trajectories of the N particles are generated iteratively using Eqs. (2.9) and (2.10). The by far most time-consuming part of each iteration is to calculate the forces $\mathbf{F}_i(t)$ from the positions.

In addition to the ingredients discussed so far—force fields and integrators—an MD simulation needs a lot of other input. There is the initial configuration to consider: because of their computational expense, MD simulations conducted at temperatures low compared to the typical energy barriers in the system will not get extremely far from their initial state [30]. Hence, this initial state cannot be chosen arbitrarily. The topology of the system, i.e., a map of which atoms are connected by bonds, should be specified. Further, there are lots of important methodological choices that should be made. Even if MD calculations are no better than the governing force field [18], they can certainly be a lot worse! This will be the case if enough attention is not devoted to a number of critical details.

The art of molecular dynamics lies in choosing the correct methods and algorithms for each system. In most biological systems, the appropriate statistical ensemble is not the microcanonical (NVE) ensemble that results from the straight-forward integration of Eqs. (2.7) and (2.8). By using, e.g., the weak-coupling algorithm of Berendsen et al. [33], we can instead opt for constant pressure P and temperature T, a much more realistic condition for, say, membrane systems. The weak-coupling scheme does not produce a well-defined ensemble [28]. This problem can be mended by using a combination of Nosé-Hoover [34, 35] and Parrinello-Rahman [36, 37] thermostats.

Another important choice regards the treatment of the boundaries of small systems. In most present-day simulations the so-called periodic boundary conditions are used [16, 17]; instead of simulating an isolated system, we consider an infinite, periodic array of systems. Periodic boundaries are closely related to a persistent problem in all condensed matter simulations: the treatment of long-range interactions. The force calculations are the expensive part of MD simulations. Without neighbor list algorithms, see Refs. [16,17], the cost of the non-bonded force computation grows as $\mathcal{O}(N^2)$ with the number of particles. In the case of short-range interactions, i.e., interactions that decay faster than r^{-d}, where d is the dimensionality, truncation and neighbor lists help to reduce the growth to $\mathcal{O}(N)$ [17]. If the forces are long-ranged, the situation is at first sight intolerable: we cannot ignore the interactions of a given particle with any particle in the infinite periodic images of the original system. This is the case for the Coulomb interactions, see Eq. (2.6). Simple truncation of the long-distance tails of the Coulomb interactions will not do, as it leads to artifacts in membrane [1–3] and other systems [17, 18]. In membrane simulations, Ewald summation techniques such as particle mesh Ewald (PME) [17, 38] have been found

to faithfully reproduce the experimental results [1–3]. PME and related schemes reduce the growth of the computational cost to $\mathcal{O}(N \log N)$ [17].

Most difficulties in MD simulations really stem from the computational expense. Yet another such issue is the choice of integration step δt. On one hand, to reach longer time scales, δt should be as large as possible. On the other hand, too large a time step will lead to instabilities and inaccuracies in the simulations [18]. By using multiple-timestep schemes [17], where the fastest degrees of freedom are attended to more frequently than the slower ones, the time step for the slow degrees of freedom may be increased. Another way of extending δt is to constrain the fastest degrees of freedom using algorithms such as SHAKE, RATTLE, or LINCS [18,28,39]. Constraining the fastest motions, e.g., certain bond vibrations with very high frequencies f, is often necessary in any event. Classical physics should not be used if $hf \gg k_{\mathrm{B}}T$, where h is Planck's constant and $k_{\mathrm{B}}T$ the thermal energy [18]. For instance all bond lengths in phospholipids at room temperature should preferably be constrained.

The expense of MD simulations has been mentioned several times. What are state-of-the-art MD simulations capable for and at what cost? The largest biological systems currently being studied by basic classical MD consist of $\sim 10^5$ atoms, which, e.g., in fully hydrated membrane systems corresponds to a bilayer patch of $20\,\mathrm{nm} \times 20\,\mathrm{nm}$. The duration of such simulations for pure lipids may be up to tens of nanoseconds. A commonly used size, approximately $5\,\mathrm{nm} \times 5\,\mathrm{nm}$, allows one to sample for 100 ns or more. The wall clock time of such a simulation is approximately one CPU year. Given these limited spatial and temporal scales, one should consider carefully what can and cannot be studied using MD, see Ref. [30] for a discussion of feasible phenomena in bilayer systems. For instance the so-called flip-flop of lipids from one monolayer to the other, with characteristic time scales of the order of seconds, is not within reach of MD. The following Sections contain examples of the most recent high-profile atomic-scale MD studies of membrane systems, concretizing the possibilities of classical MD.

2.4 Atomistic MD Simulation of Membranes

The first atomistic lipid bilayer MD simulations were published in the 1980s [30, 40]. At the beginning, the focus was on single-component lipid bilayers in the liquid-disordered phase. Early benchmark bilayers were the

saturated DPPC, DMPC, and DLPE. Soon after came the first unsaturated bilayer simulations with lipids such as POPC, DOPC, and DOPE. These simulations were typically tens or at most hundreds of picoseconds long, three or four orders of magnitude shorter than today.

The review paper of Tieleman et al. [30] gives a detailed picture of the history and state of the art of membrane simulations in 1997. The review is still a highly relevant account on the fundamentals of membrane modeling, with insights into model design, data analysis, and comparison of simulation results with experimental ones. Further, some of the topics that have become more feasible and therefore popular during the 2000s—composite bilayers, lipid-protein interactions, transport properties—are already discussed in this review.

Since the 1990s, there has been a rapid development in the field of membrane modeling. The time scales have been extended to 100 ns and more, the simulations agree better with experimental data, and the systems have grown more complex. This is thanks to faster processors and, perhaps more important, methodological development: more sophisticated force fields, as well as effective and accurate treatment of electrostatic interactions. Up to 2002, the development has been accounted for in the reviews by Forest and Sansom [41], Feller [42], Scott [43], and Saiz et al. [44, 45]. In the following, we shall briefly discuss the most recent trends in membrane modeling.

Common to all computational membrane studies is that the models of cell membranes are steadily becoming more realistic. As real cell membranes may contain some two hundred different lipid species, as well as sterols, carbohydrates, and proteins [5, 46], the approach must be gradual: everything cannot be incorporated at once. Furthermore, membranes are not isolated, and thus their interaction with, e.g., solutes such as anesthetics, ions, and DNA must be studied further.

An important step towards more realistic systems is the modeling of biologically relevant binary and ternary mixtures of lipids. Phospholipid/cholesterol [47–51] studies and sphingomyelin simulations [52–54] pave the way for ternary systems containing phospholipids, sphingomyelin, and cholesterol [55, 56]. The interest in such ternary systems has its origins in a desire to understand lipid rafts, i.e., domains rich in saturated phospholipids, sphingomyelin, and cholesterol [7, 9, 57]. In cells, rafts are thought to confine proteins involved in, e.g., signal transduction, and therefore act as platforms for adhesion and signaling. Even without

proteins, simulations of ternary mixtures are challenging, since both the spatial and temporal scales targeted in these simulations must be very large. The sizes of rafts *in vivo* are probably less than ten nanometers [7], while domains in model lipid bilayers appear to be larger, see Ref. [7]. In addition, it is unrealistic to expect rafts to assemble and the system to fully equilibrate during a mere 100 ns. Hence, although MD simulations certainly give valuable insights into rafts, less detailed approaches will be needed.

Another interesting direction is to model the interaction of solutes with lipid bilayers. For instance the molecular mechanisms of anesthesia are not yet understood. It is, however, possible that the interaction between lipids and anesthetics plays a critical role here [58,59]. Pasenkiewicz-Gierula et al. [60] have recently published an MD study of the interaction of carane derivative local anesthetics with POPC lipids. Koubi et al. [61] have studied the effect of halothane and hexafluoroethane on polyunsaturated lipid bilayers. A closely related topic is the interaction of short-chain alcohols with bilayers. Patra et al. [62] have used MD to investigate the effect of methanol and ethanol on DPPC and POPC bilayers. Other recent MD studies of the interaction of solutes with bilayers have featured solutes such as trehalose [63,64], sucrose [64], pentacholophenol [65], dimethylsulfoxide [64], and diphenylhexatriene [66], see also Ref. [67].

Membranes *in vivo* are immersed in an aqueous solution containing ions, typically Na^+, Ca^{2+}, K^+, and Cl^- [5, 46]. Approximately 10–30 % of all lipids in real membranes are charged [31, 68], and hence counterions have to be present to compensate for the charge. The presence of ions has been shown to significantly affect the electrostatic, structural, and dynamic properties of bilayers, see e.g., Ref. [69]. Therefore the interaction of ions with bilayers is an important, although computationally demanding, subject. Recently, MD studies of the effect of sodium chloride on neutral bilayers have been reported by Böckmann et al. [69,70] and Pandit et al. [71]. Sachs et al. [72] have investigated the effect of a series of monovalent Na^+ salts on a POPC bilayer. Charged bilayers have also been studied using MD: Pandit and Berkowitz [73] have published simulations of DPPS bilayers with Na^+ counterions, Mukhopadhyay et al. [74] of POPS bilayers with Na^+ counterions and NaCl, and Pandit et al. [75] of mixed bilayers of DPPC and DPPS in NaCl solutions of different concentrations.

A particularly interesting class of charged bilayers are those consisting of cationic lipids. This is because of their relevance in gene therapy, drug delivery, and our general understanding of DNA-membrane interactions.

A slightly older, highly interesting study of Bandoyopadhyay et al. [76], where a short strand of DNA is intercalated into a DMPC/DMTAP bilayer, has been recently complemented by Gurtovenko et al. [77]. They have studied DMPC/DMTAP bilayers with DMTAP concentrations from 0 to 100 %, paying particular attention to the behavior of the positively charged DMTAP and zwitterionic DMPC headgroups. Their findings will be useful in future studies of membrane systems with DNA. Currently, DNA/lipid complexes are receiving comparatively little attention, especially compared with the surging numbers of membrane protein simulations.

Simulations of membrane proteins have recently been reviewed by Ash et al. [68]. An increasing number of experimental high-resolution structures of membrane proteins, together with advances in simulation methodology and hardware, have made these studies worthwhile. There are now MD simulations of a wide variety of proteins, e.g., G-protein-coupled receptors, aquaglyceroporins, ion channels, ATPases, and outer membrane proteins. Also membrane binding peptides such as toxins and antibiotics, model transmembrane helices, as well as natural and synthetic ion channel forming peptides are being studied. For instance in the case of antibiotics and toxins, the influence of the peptides or proteins on the surrounding bilayer is investigated. In most cases, however, the function of the protein in its lipid environment is the primary target. Examples include trying to understand why aquaporins allow water and glycerol to pass through, but block the entrance for protons [78], how the structure of a mechanosensitive channel from *E. coli* changes under the influence of membrane tension [79], or how different ions interact with the selectivity filter of a KcsA potassium channel [80].

Transport of ions and small molecules, not only through channels, but also through the lipid component of the membrane, is vital to cells. Permeation of solutes through the lipid matrix is particularly challenging to simulate: several seconds would be required to observe the spontaneous transport of water across a 4 nm × 4 nm bilayer patch [30]. The standard procedure is therefore to constrain the solutes to different depths in the heterogeneous membrane, and measure the local diffusion coefficients and solubilities to arrive at the overall permeability coefficient of the membrane to a given solute [81, 82]. Recently, Bemporad et al. [83, 84] have reported MD simulation results for the permeation of eight small organic molecules, both hydrophilic and hydrophobic ones, through a DPPC bilayer. Although the results are not in quantitative agreement with experiments, the relative

permeabilities of the molecules were reproduced. For both hydrophobic and hydrophilic components, the permeability coefficient of the membrane is predominately determined by the solubility, i.e., the free energy profile. In addition, it appears as if the diffusion depended less than expected on the size of the solute, and the partitioning more so. Ulander and Haymet [85] have studied the permeation of valproic acid—a small, branched fatty acid used as an anticonvulsant and mood stabilizer—across DPPC bilayers. Their results highlight the importance of sampling along the bilayer normal and abandoning simplified mean-field approaches. Finally, Shinoda et al. [86] have published an MD study of the effects of chain branching on permeation of water and small, nonionic solutes, comparing transport through DPPC and branched-chain DPhPC bilayers.

Other recent topics in membrane simulations include the structural properties of branched-chain lipid bilayers [87], polyunsaturated lipids [61, 88–90], and binary mixing of PC and PE lipids [91]. Further, formation of hydrophilic pores [92] and the properties of bilayer edges [93, 94] have been studied, as have the static and dynamic properties of the lipid/solvent interface [95–97]. A highly interesting investigation into the spontaneous formation and final structure of a small DPPC vesicle in water has also been reported [98].

2.5 Case Study: Cholesterol in Phospholipid Bilayers

2.5.1 DPPC/Cholesterol System

The lipid component of a cell membrane of a higher organism may consist of different kinds of glycerophospholipids, sphingolipids, glycolipids, and cholesterol. To eventually understand the rich physics and chemistry of such mixtures—the complicated phase behavior, rafts, and all—it is a good idea to start with binary mixtures. Studying dipalmitoylphosphatidylcholine (DPPC)/cholesterol systems is particularly useful, on one hand because cholesterol is such an interesting and abundant molecule, and on the other hand because binary mixtures of saturated phospholipids and cholesterol have been extensively characterized in experiments [99–103].

Experiments have shown that cholesterol modulates the physical properties of real cell membranes, as well as those of the simpler model bilayers [99].

The phase diagram in Fig. 2.1 summarizes the structural changes cholesterol brings about in DPPC/cholesterol bilayers.

Pure DPPC bilayers are, at low temperatures, in the gel or solid-ordered (**so**) phase, characterized by hexagonally arranged PC headgroups and all-trans hydrocarbon tails. Above the main transition temperature $T_{\mathrm{M}} = 314.5\,\mathrm{K}$, the pure bilayer is in the liquid crystalline or liquid-disordered (**ld**) state with the headgroups forming a two-dimensional liquid and with gauche defects in the tails. The main phase transition thus couples two order-disorder transitions, translational and orientational ones. The presence of cholesterol decouples these two, and leads to the introduction of a new phase, the liquid-ordered (**lo**) one. The **lo** phase is distinguished by a liquid-like arrangement of the PC headgroups and tails with a high degree of ordering. In addition there are **ld-lo**, **ld-so**, and **so-lo** coexistence regions.

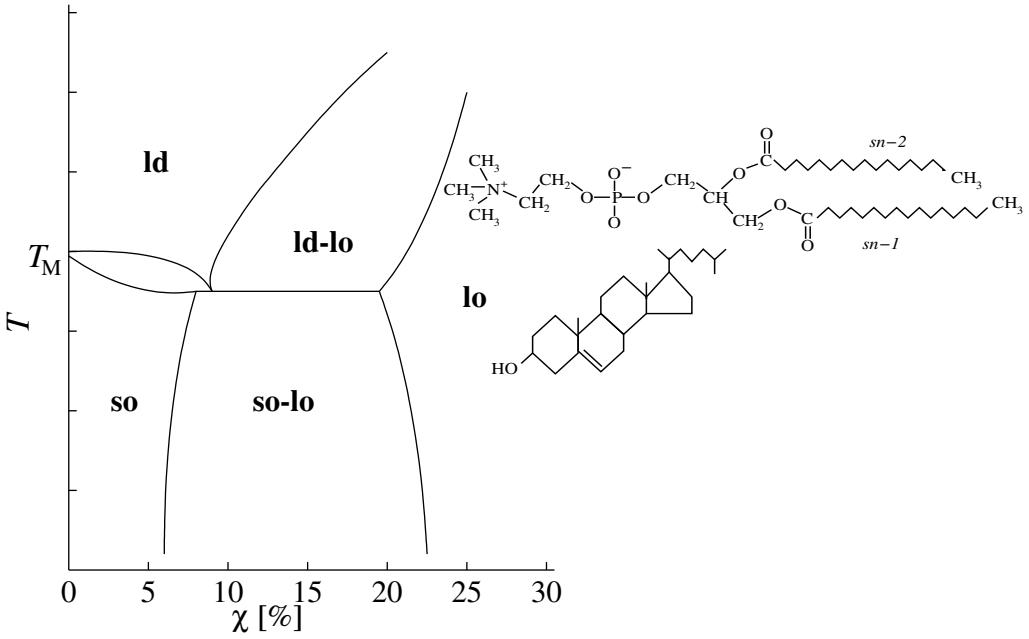

Figure 2.1. Schematic phase diagram of DPPC/cholesterol system after Refs. [103, 104], see the text for details. On the right hand side are the structural formulae for the saturated DPPC (di(16:0)PC) (above) and cholesterol (below).

In the physiologically relevant **ld** phase, adding cholesterol to a DPPC bilayer alters the molecular packing: the orientational order of the hydrocarbon tails increases [47–49,99,102] and the average area per molecule

decreases [105]. These changes lead to the introduction of the **ld-lo** and **lo** regions in the phase diagram.

An increasing cholesterol content also effects changes in the dynamic properties of bilayers. In the case of saturated phospholipids the passive permeation of small solutes [106–110] and the lateral diffusion of phospholipids [10, 49, 111–113] are affected. Such dynamic processes in bilayers are intimately connected to the amount, distribution, and fluctuations of free volume [111, 112, 114–117], i.e., space not occupied by phospholipids, cholesterols, or water. It is therefore reasonable to anticipate that cholesterol modifies the free volume properties of bilayers. Further, the changes in packing, free volume, and transport properties can be expected to be coupled.

We have studied the cholesterol-induced changes in packing, free volume, ordering, and lateral diffusion in DPPC bilayers. To this end, 100 ns MD simulations of DPPC/cholesterol bilayers, with cholesterol concentrations from 0 to 50 mol %, have been performed. The first part of the work included validating the computational model by comparing key empirical quantities such as average areas per molecule, NMR order parameters, and electron density profiles with experimental findings [48]. As such quantities often are [47, 49], and indeed should be, computed in simulation studies, we will not discuss them explicitly. In the second part, inspired by free area theories [111, 112, 118], we investigated the interplay of packing, average free area per molecule, and lateral diffusion [48]. In the final phase, we studied the detailed distribution of free volume in bilayers, characterizing the size, shape, and orientation of free volume pockets or voids [119].

2.5.2 Model and Simulations

We simulated fully hydrated lipid bilayers with 128 macromolecules, i.e., DPPCs and cholesterols, and 3655 water molecules. In addition to pure DPPC, we studied systems with five different cholesterol molar fractions: $\chi = 4.7\,\%$, $12.5\,\%$, $20.3\,\%$, $29.7\,\%$, and $50\,\%$. A snapshot of the system containing $20.3\,\%$ cholesterol is shown in Fig. 2.2. The underlying MD simulations have been described in Ref. [48], and we shall only give a brief summary of the most important details here. As for validation, the results have been shown to be in good agreement with experimental studies, see Ref. [48], and other simulation studies [47, 49, 120–123].

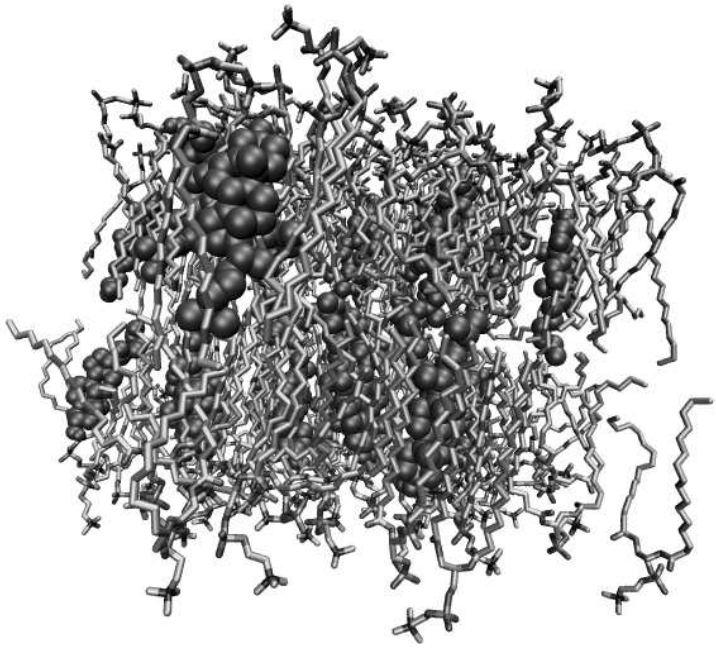

Figure 2.2. Snapshot of DPPC/cholesterol system with $\chi = 20.3\,\%$. The water has been omitted for clarity. DPPCs have been drawn using sticks and cholesterols using spheres.

The united atom force fields for the DPPC and cholesterol molecules were adopted from earlier studies [124–126], and the SPC model was used for water molecules [127]. The initial configuration for the pure DPPC bilayer was taken from the final structure of run E in Ref. [126]. For systems with finite cholesterol concentrations, the initial configurations were constructed by replacing randomly selected DPPC molecules with cholesterols such that the same number of DPPC molecules was replaced in each monolayer. To fill the free volume left by replacing DPPCs by the smaller cholesterols, the system was thoroughly equilibrated, see Ref. [48] for details. The bilayer was aligned such that it lies in the xy plane and the bilayer normal is parallel to the z axis.

The MD simulations were run at a temperature $T = 323\,\mathrm{K}$, which is above the main phase transition temperature of DPPC at $T_\mathrm{M} \approx 314.5\,\mathrm{K}$. We used the GROMACS [28, 128] molecular simulation software. After the initial equilibration, the system was kept at constant temperature at a pressure of 1 bar using the Berendsen thermostat and barostat [33]. For long-range electrostatic interactions we used the PME method [129], which has been

shown to yield reliable results for bilayers [1, 2]. The time step was chosen to be 2.0 fs and the duration of each simulation was 100 ns.

For all systems up to and including the system with $\chi = 29.7\,\%$, a simulation time of 100 ns guarantees a reasonable sampling of the phase space. The results for 50 % cholesterol should be regarded with some caution: the diffusion of the DPPC and cholesterol molecules is rather slow in this system [48] and the system probably bears traces of its initial configuration. This applies to all state-of-the-art simulation studies of phospholipid/cholesterol systems, and has been mentioned by other authors [122]. In the following we will focus on $\chi = 0 - 29.7\,\%$.

2.5.3 Diffusion, Free Volume, and Packing

In this Section, we will discuss cholesterol's effect on lateral diffusion of DPPCs and cholesterols, free volume, and packing. In particular, we will focus on the interplay of these effects. A first step in studying the interplay is to consider simple free area theories for diffusion in lipid bilayers.

Free volume theory was developed to describe the transport properties of glass-forming fluids [118, 130–132], and later adapted to modeling lateral self-diffusion in lipid bilayers [111, 112, 133, 134]. In this approach lipid bilayers are assumed to be homogeneous in the normal direction: lipids and sterols are viewed as cylinders or disks diffusing in the plane of the membrane. The model thus becomes essentially two-dimensional, and is in this context usually called free area theory.

According to free area theory, lateral diffusion of a lipid or sterol in a bilayer is restricted by the occurrence of large enough free areas next to it. A diffusing molecule spends tens of nanoseconds [10, 30] rattling in a cage formed by its neighbors, and according to free area theory, given a large enough activation energy and an adjacent free area, jumps to that nearby free site. Hence, for the lateral tracer diffusion coefficient of a lipid or sterol, we can write [111]

$$D_{\mathrm{T}} \sim \exp\left(-\frac{a_0}{a_{\mathrm{f}}}\right). \tag{2.11}$$

Here a_{f} the average amount of free area per molecule in the bilayer and a_0 is the cross-sectional close-packed area of a cylindrical DPPC or cholesterol molecule.

To study the pertinence of Eq. (2.11), we will first look at the lateral diffusion coefficients for DPPCs and cholesterols at different cholesterol concentrations. The lateral tracer diffusion coefficients can be computed from an Einstein relation

$$D_{\mathrm{T}} = \lim_{t\to\infty} \frac{1}{4tN_{\mathrm{species}}} \sum_{i=1}^{N_{\mathrm{species}}} \langle [\mathbf{r}_i(t) - \mathbf{r}_i(0)]^2 \rangle. \tag{2.12}$$

Here the sum runs over all molecules of a given species, and $\mathbf{r}_i(t)$ is the center of mass (CM) position of molecule i. The diffusion coefficients have been calculated by following the position of a molecule in a given monolayer with respect to the CM of that monolayer. By taking into account the motion of the CM of each monolayer, we have ensured that, e.g., drift should not be a problem. Note that in the case of lateral diffusion all positions are projected to the plane of the bilayer.

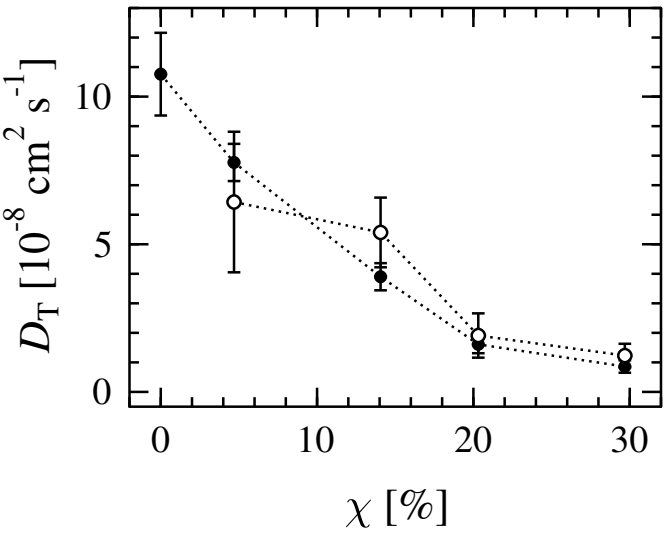

Figure 2.3. Lateral diffusion coefficients of DPPCs (•) and cholesterols (◦) as functions of cholesterol concentration [48].

Lateral diffusion coefficients for DPPC and cholesterol as functions of cholesterol concentration χ are shown in Fig. 2.3. Both decrease monotonically when χ increases, in qualitative agreement with experiments [11, 13, 111, 135].

Having established that cholesterol suppresses lateral diffusion of both DPPCs and cholesterols, we will focus on the average free area per molecule

a_{f}. Figure 2.4 shows the total empty free volume in the bilayer, computed using a grid approach explained in Ref. [48], as a function of χ. By empty free volume we simply mean all space outside the van der Waals radii of the atoms. Assuming, in the spirit of free area theory, that the bilayer is homogeneous in the normal or z direction, it does not matter whether we consider free volume or area: *if our assumption is correct*, the latter is linearly proportional to the former. Further, as the total number of DPPCs and cholesterols is constant for all χ, the total free volumes portrayed in Fig. 2.4 are linearly proportional to the average free area per molecule a_{f}.

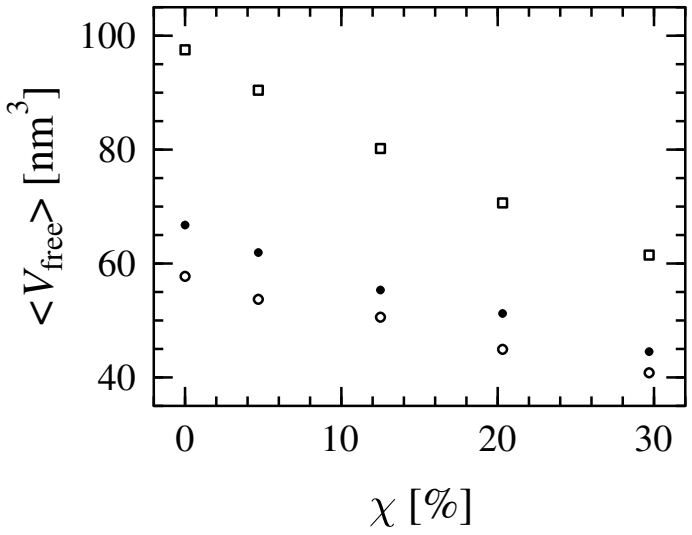

Figure 2.4. Empty free volume as function of cholesterol concentration [48]. As the lipid/water interface is very broad, there is no unique definition for the thickness of a bilayer. Hence, we have used three different definitions. The thicknesses have been defined as the distance between the points where the density of water starts to deviate from the bulk value (□), the distance between the points where the density of phospholipids and water are equal (○), and the distance between the maxima in the total electron densities (●). The errors are of the order of a few percent.

An examination of Fig. 2.4 shows that the total empty free volume and therefore also the average free area per molecule decrease monotonically with χ. So far so good: in the spirit of free area theory, we should intuitively expect that less free area per molecule leads to slower diffusion. This, of course, requires that a_0 is largely independent of χ, or at least does not decrease significantly with χ. In the case of the rigid and bulky cholesterol

molecule, χ probably has very little influence on a_0. Predicting the behavior of the average cross-sectional area of DPPC with χ is more difficult. The ordering of the tails and a possible reorientation of the headgroup may well imply an increasing or decreasing a_0.

It appears that we cannot proceed without actual numbers. By mapping bilayers onto grids [48], we can find estimates for a_f and a_0. The calculation is such that the average free and cross-sectional areas will be calculated separately for thin slices in the normal direction, i.e., we will end up with $a_\mathrm{f}(z)$ and $a_0(z)$. We will thus be able to check the assumption about homogeneity in the normal direction.

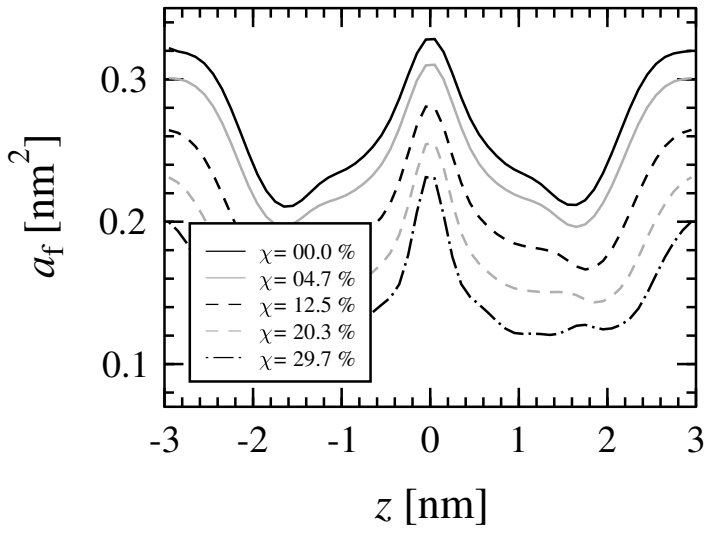

Figure 2.5. Average empty free areas per molecule as functions of position along bilayer normal [48]. The center of the bilayer corresponds to $z = 0$. The errors are smaller than a percent.

The average free areas per molecule as functions of position along the bilayer normal—the free area profiles—for different χ are portrayed in Fig. 2.5. The first important observation is that the normal direction is by no means homogeneous. There is more free space in the bilayer center or in the water phase than at a distance $z \approx 2\,\mathrm{nm}$ from the bilayer center, just behind the headgroups. Second, the average amount of free area per molecule is, for all values of z, quite large. By multiplying the average free area per molecule by the total number of DPPCs and cholesterols in a monolayer and comparing this figure with the average areas of the bilayer patches [48], we can conclude

that at least 30 % of the bilayer must be free space. Finally, the amount of free area is reduced by an increasing cholesterol concentration for all z.

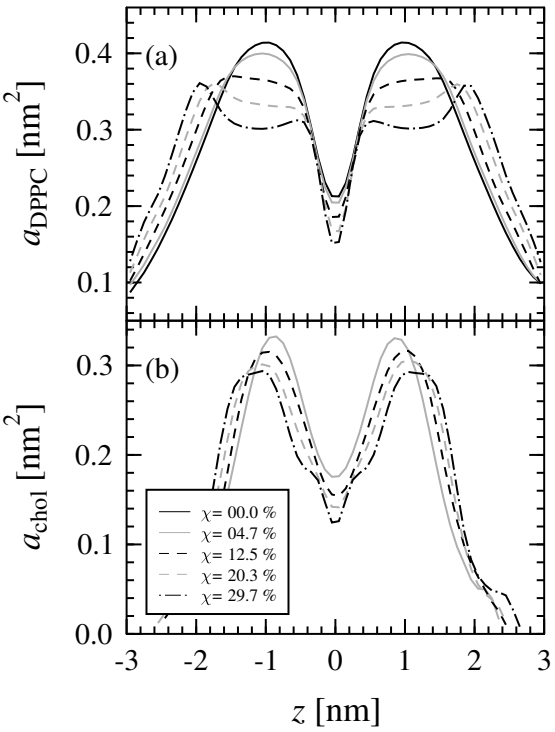

Figure 2.6. Average cross-sectional close-packed areas for (a) DPPC and (b) cholesterol as functions of position along bilayer normal [48]. The errors are of the order of a few percent. In the water phase, the relative errors of a_{chol} are somewhat larger.

The heterogeneity in the free area profiles suggests that not even in the average sense are the DPPC and cholesterol molecules cylindrical. Figure 2.6, showing the average close-packed cross-sectional areas for DPPC and cholesterol as functions of position along the bilayer normal, confirms this hypothesis. These cross-sectional area profiles have been obtained by dividing the average area occupied by, say, DPPC in a given slice by the number of DPPC molecules in that slice, see Ref. [48]. The cross-sectional area profiles for DPPC reflect the ordering of the chains and the reorientation of the headgroups with an increasing χ. As expected, all $a_{\mathrm{chol}}(z)$ irrespective of χ are quite similar. The slight changes are caused by the reduced tilt of the cholesterol molecules.

Let us, despite the heterogeneity in the normal direction, for a while insist on using Eq. (2.11) to describe lateral diffusion of DPPCs and cholesterols. As the free area per molecule and the cross-sectional areas for DPPC and cholesterol vary with z, the choice of scalar values for a_f and a_0 becomes ambiguous. We could, e.g., use values extracted at $z = 1\,\mathrm{nm}$ from the bilayer center. This region contains the phospholipid tails and the cholesterol ring structures, and must be important to interactions between cholesterol and DPPC molecules. Plugging the numbers into Eq. (2.11) results in a prediction for the behavior of the lateral diffusion coefficients: when χ increases from 0 % to 30 %, the lateral diffusion coefficients should decrease by a factor of two or three at most. As a matter of fact, using any numbers from the free and cross-sectional area profiles results in a reduction of the same magnitude. At the same time Fig. 2.3 clearly shows that the diffusion coefficients decrease by an order of magnitude.

Is there any way to improve the prediction for the behavior of the diffusion coefficients with χ? Possibly. Apart from a large enough free site to jump to, a molecule attempting a jump needs enough energy to overcome the activation barrier E_a. In free area theory this is accounted for by the familiar Boltzmann factor: $D_\mathrm{T} \sim \exp(-E_\mathrm{a}/k_\mathrm{B}T)$. As E_a probably increases with χ, see Ref. [48] for a discussion, the reduction of D_T for both DPPC and cholesterol presumably becomes larger than a factor of two or three. Quantitative testing of this hypothesis is, unfortunately, an expensive exercise, since it requires computing lateral diffusion coefficients as functions of both χ and T.

The kind of semi-quantitative chat we have engaged in above should not blind us to the important conclusion: any two-dimensional mean-field theory is too crude to quantitatively describe diffusion in bilayers. In addition to the fact that the bilayer is truly heterogeneous in the normal direction, characterizing complicated structures and processes from a mean-field point of view turns out to be too simplistic. A figure for the average free area per molecule or the average amount of free volume in the bilayer does not tell us anything about the distribution and fluctuations of free volume in the bilayer. Is there one large, stable hole in the bilayer or are there many tiny ones that are created and destroyed with characteristic times in the nanosecond range? Distinguishing between these two scenarios is extremely important from the point of view of permeation and lateral diffusion. Further, the average cross-sectional area profiles do not tell us much about the conformations of individual molecules or possible DPPC-

cholesterol complexes. Finally, the detailed mechanism of diffusion jumps must be fascinatingly complex, involving collective motion of several DPPCs and cholesterols, as well as redistribution of free volume. Exciting diffusion mechanisms have been observed, e.g., on metal surfaces [136–138] and in supercooled liquids [139]. No one has yet studied such mechanisms in membrane systems.

The incompleteness of free area theories thus opens up several interesting directions for new research. We are currently studying the ones sketched in the previous paragraph. In the following we shall concentrate on one of these: the detailed distribution of free volume in phospholipid bilayers, and in particular, the effect of cholesterol on this distribution.

2.5.4 Voids

Rather than two-dimensional assemblies of disk-like molecules, membranes are porous three- or quasi-two-dimensional structures with free volume pockets or voids. As we shall see, lipid bilayers contain voids of different sizes, shapes, and orientations. These voids are dynamic: they can be generated or annihilated by trans-gauche isomerizations in the hydrocarbon tails of lipid molecules, or less frequently, by the movement of whole lipids or sterols [114].

Voids are very significant for dynamic processes in lipid bilayers [117]. Lateral diffusion of lipids and sterols [111, 112], as well as diffusion of small solutes within or across membranes are such processes. More specific examples of the latter include passive permeation of water, oxygen, small organic molecules, and small ions to and from cells [81–83, 85, 108, 114, 117, 140], and diffusion of the electron carrying quinone in mitochondria and chloroplasts [141]. MD simulations indicate that diffusion of small solutes proceeds via jumps between neighboring voids [66, 82].

MD simulations are an excellent tool for studying the detailed free volume properties of lipid bilayers. Bassolino-Klimas et al. [114, 142] used the size distribution of voids to explain the motion of benzene molecules in lipid bilayers. The first and so far only detailed analysis of the properties of voids in lipid bilayers was reported by Marrink et al. [116]. They looked at the size, shape, and orientation of the voids in a DPPC bilayer, and pointed out that these properties vary strongly in the direction of the bilayer normal. More recently, Shinoda et al. [86] addressed the effect of chain branching

on the size distribution of voids, concluding that branching reduces the probability of observing large voids. Jedlovszky et al. [108], in their MC simulations of DMPC/cholesterol bilayers, briefly looked at the impact of cholesterol on the number of large voids.

Equipped with our DPPC/cholesterol MD data, we focus on the impact of cholesterol on the properties of voids in bilayers consisting of DPPC. The technical details of how the voids were identified and characterized using a union/find algorithm [143] and principal component analysis (PCA) [144] can be found in Ref. [119]. Before describing the results of our analysis, we should explain a few important concepts.

The first important notion is that of accessible free volume [116], the free volume relevant for solute diffusion in bilayers. In the previous Section we were dealing with empty free volume, i.e., all volume outside the van der Waals radii of the atoms. Accessible free volume corresponds to the free volume accessible to the CM of the diffusing solute, and is calculated by adding the van der Waals radius of the diffusing solute molecule to the van der Waals radii of the atoms in the bilayer. We have used different solute sizes with radii r ranging between 0 and 0.2 nm. These sizes are of the same magnitude as the effective van der Waals radii of, e.g., bare Na^+, K^+, and Cl^- ions; water and oxygen molecules; and the general anesthetic xenon.

A further prerequisite for understanding the subsequent discussion on voids is the so-called four region model originally introduced by Marrink et al. [81,116]. As the free volume properties vary with the position along the bilayer normal [116,119], it is not optimal to study the properties of voids averaged over the whole bilayer. Instead, we have discretized the bilayer into regions with more homogeneous compositions, slightly modifying the original partition, see Fig. 2.7. Region 1 ranges from the point where the mass density of water starts to deviate from the bulk value to the point where the densities of DPPC and water are equal. This region contains mostly water molecules and some DPPC headgroups. Region 2 extends from the point where the densities of water and DPPC coincide to the point where the density of cholesterol ring structures is half of its maximum plateau value [48]. This region is dominated by the DPPC headgroups: the choline, phosphate, and glycerol densities peak here. In addition a finite density of DPPC tails and the major part of cholesterol hydroxyl groups can be found in Region 2. Region 3 is defined between the points where the cholesterol steroid ring density assumes half of its maximum value, and contains in addition the middle parts of the DPPC tails. The remaining

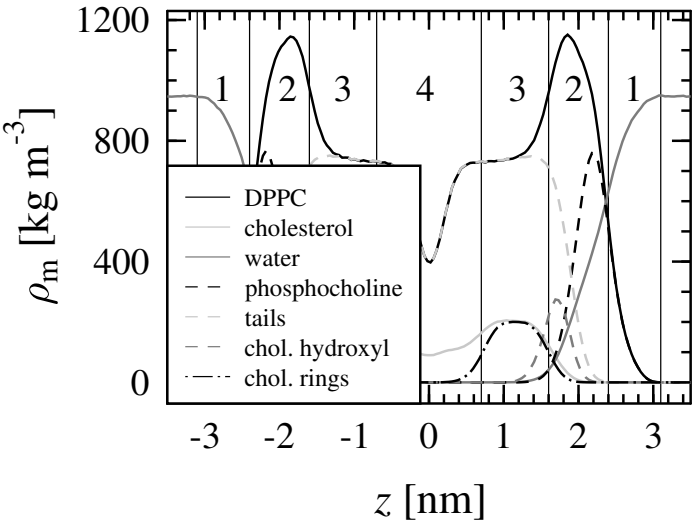

Figure 2.7. Mass density profiles of molecules and atomic groups at $\chi = 20.3\,\%$ [48]. The mass density of the cholesterol hydroxyl groups has been scaled by a factor of ten. The division into four regions, indicated here by numbers 1–4, is based on the mass density profiles, see the text.

part of the bilayer, i.e., the center of the bilayer, is Region 4, with a low density of DPPC and cholesterol tails. Since an increasing χ shifts the various atomic groups away from the bilayer center [48], the boundaries between the regions vary with cholesterol concentration. As the densities of DPPC and water are very similar in the pure DPPC bilayer and the bilayer with 4.7 % cholesterol [48], the boundaries for pure DPPC have been taken to be the same as in the case of 4.7 % cholesterol.

Let us take a closer look at the voids in the four regions. Figure 2.8 shows the most important void properties in a system with $\chi = 20.3\,\%$ with a permeant radius $r = 0.09\,\mathrm{nm}$. Panel (a) contains the unnormalized size distributions for voids; $N(V)$ is the average number of voids of volume V. Panel (b) characterizes the shape of the voids with $4 \times 10^{-3}\,\mathrm{nm}^3 < V < 0.13\,\mathrm{nm}^3$. As opposed to larger voids with more complicated shapes, these voids can be considered ellipsoidal, and therefore may be characterized using PCA. PCA allows us to extract σ_1, σ_2, and σ_3, which are proportional to the lengths of the principal axes of an ellipsoidal void. From these we can compute $P(\sigma_i/\sigma_j)$, the probability of finding a void with a given value of σ_i/σ_j irrespective of σ_k, $k \neq i, j$ [119]. Finally, panel (c) describes the

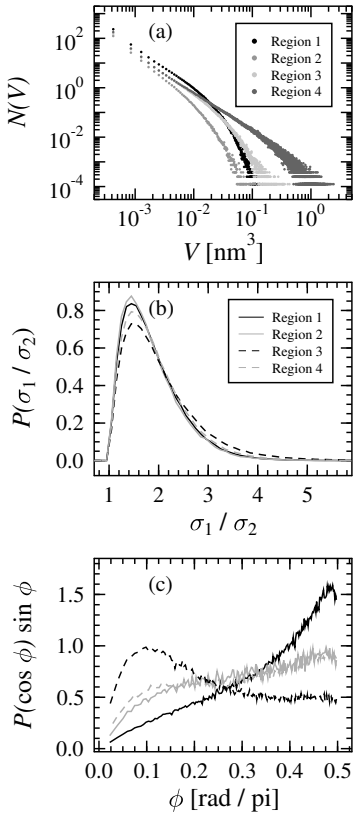

Figure 2.8. Properties of voids in Regions 1–4 for $\chi = 20.3\,\%$ and $r = 0.09\,\mathrm{nm}$ [119]. (a) Size distributions, see Fig. 2.9 for errors. (b) $P(\sigma_1/\sigma_2)$ with errors smaller than two percent for $\sigma_1/\sigma_2 < 3$, and between two and five percent for $3 < \sigma_1/\sigma_2 < 6$. (c) $P(\cos\phi)\sin\phi$, see Fig. 2.11 for errors.

orientation of non-spherical voids with $4 \times 10^{-3}\,\mathrm{nm}^3 < V < 0.13\,\mathrm{nm}^3$. The orientations of the principal axes of the ellipsoidal voids can be extracted from PCA. The quantity $P(\cos\phi)\sin\phi$ is the probability that an elongated void is oriented such that the angle between its longest axis and the bilayer normal is ϕ [119].

Region 1 contains more small voids with radii of the order of a few angstroms than any other region, and virtually no voids larger than $0.10\,\mathrm{nm}^3$. Region 2 is similar, except the number of voids with small or intermediate V is almost an order of magnitude smaller than in Region 1. Region 3 features larger voids than do Regions 1 and 2. The largest voids, however, can be found in Region 4, with sizes up to to $V \approx 2\,\mathrm{nm}^3$. The bilayer as a whole

contains very few spherical voids, i.e., in most cases $\sigma_1/\sigma_2 \neq 1$. The voids with $4 \times 10^{-3}\,\mathrm{nm}^3 < V < 0.13\,\mathrm{nm}^3$ are most elongated in Region 3, and the void shapes in Region 4 appear to differ from Regions 1 and 2 only slightly. This is true for small voids with $V < 0.13\,\mathrm{nm}^3$; we should keep in mind that Region 4 also contains larger voids, see panel (a) of Fig. 2.8. The shapes of these holes are not ellipsoidal but more complex. As for orientations, in Region 1 there are no voids such that the principal axis would be oriented along the bilayer normal: the most probable orientation of the principal axis is in the plane of the membrane. Region 2 is, again, rather similar to Region 1, although the distribution is more uniform and $\phi = \pi/2$ not so much favored. Region 3 is significantly different: orientation along the bilayer normal or close to it is preferred and orientation in the plane of the membrane is rare. Finally, Region 4 contains mostly voids that are oriented in the plane of the bilayer.

How does changing the penetrant size r from $r = 0.09\,\mathrm{nm}$ affect this picture? If $r = 0.09\,\mathrm{nm}$, the free volume does not percolate in either x, y, or z direction [119]. By percolation in, e.g., x direction, we mean that there is a large void stretching, in the x direction, from one side of our patch of bilayer to the opposite side. For a more detailed discussion on percolation theory and percolation in infinite and finite systems, see Refs. [116,119,145]. With $0.05\,\mathrm{nm} \lesssim r \lesssim 0.08\,\mathrm{nm}$, the free volume percolates in Region 4 in the xy plane, and for $r \lesssim 0.04\,\mathrm{nm}$ in addition in the z direction [119]. The presence of a percolating cluster is reflected in the size distribution and orientational distribution in Region 4: the percolating cluster is clearly visible in $N(V)$ and $P(\cos\phi)\sin\phi$ has a peak close to $\phi = 0$, see Ref. [119] for details.

The rest of this Section deals with how a changing cholesterol concentration χ affects the voids. As these effects are restricted to Regions 3 and 4, where the cholesterol steroid ring structures and tails reside, we will focus on these regions.

The behavior of the size distribution of voids with an increasing χ is illustrated in Fig. 2.9. As the vicinity of the percolation transitions is significant for the form of the distribution, we have identified two cases that represent the most biologically relevant regimes: $r = 0.05\,\mathrm{nm}$ at which xy percolation takes place in Region 4 and $r = 0.09\,\mathrm{nm}$ with no percolation. The regime where xyz percolation occurs is quite similar to the case of $r = 0.05\,\mathrm{nm}$. Besides, even though our results are qualitative rather than quantitative in nature, penetrant radii smaller than 0.05 nm are unphysical.

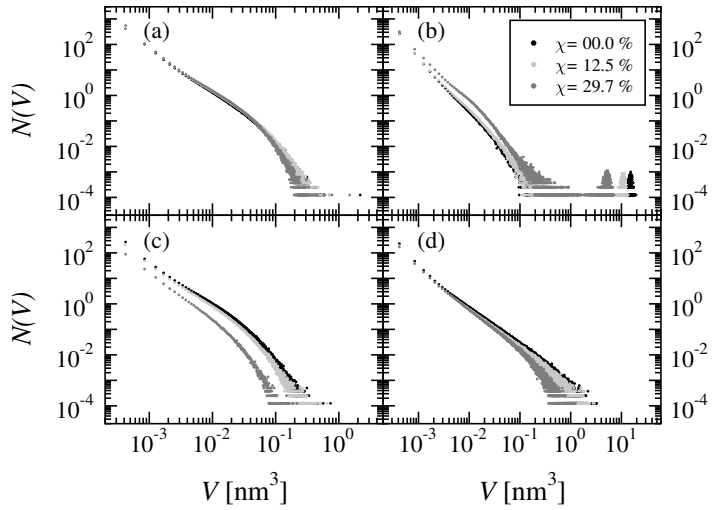

Figure 2.9. Effect of cholesterol concentration on void size distributions [119]. (a) Region 3 and $r = 0.05\,\mathrm{nm}$. (b) Region 4 and $r = 0.05\,\mathrm{nm}$. (c) Region 3 and $r = 0.09\,\mathrm{nm}$. (d) Region 4 and $r = 0.09\,\mathrm{nm}$. Percolation in the plane of the bilayer is seen in panel (b) as a separate cluster of points in the right-hand corner. The finite statistics lead to relative errors that grow with V. For $V < 0.01\,\mathrm{nm}^3$ the errors in $N(V)$ are smaller than a percent, and in the range $0.01\,\mathrm{nm}^3 < V < 0.1\,\mathrm{nm}^3$ smaller than ten percent. If V is of the order of $1\,\mathrm{nm}^3$, the relative errors may be 100–300 %. As the data are shown on a log-log scale, this is hardly a problem.

The case of $r = 0.05\,\mathrm{nm}$, representing all r below the xyz percolation threshold and above the xy threshold, is portrayed in panels (a) and (b) of Fig. 2.9. The most notable effect in raising χ from 0 % to 29.7 % is the reduced connectivity of free volume. This is manifested in the size of the percolating cluster, which decreases by a factor of three to $V \approx 5\,\mathrm{nm}^3$, approximately ten times the average close-packed volume of a cholesterol molecule, $V_{\mathrm{chol}} \approx 0.459(2)\,\mathrm{nm}^3$ [48]. At the same time the number of non-percolating voids of all sizes in Region 4 increases: although the total free volume decreases, the number of voids increases by a factor of three. The effects in Region 3 also reflect the reduced connectivity, but are very minor. Here the number of large voids with $V \approx V_{\mathrm{chol}}$ decreases somewhat, while the number of voids from those with radii of the order of 0.1 nm to $V \approx V_{\mathrm{chol}}/10$ increases slightly.

The situation with no percolating cluster, more specifically with $r = 0.09\,\mathrm{nm}$, is illustrated in panels (c) and (d) of Fig. 2.9. The effects of

cholesterol are very pronounced in Region 3. Comparing the case of $\chi = 29.7\,\%$ with pure DPPC we note that there are fewer voids of all sizes. The number of voids is reduced at least by a factor of three, but especially for larger voids the reduction can be as large as a factor of twenty. The largest voids with $V \approx V_{\mathrm{chol}}$ are removed completely. The effects are similar, although more minor, in Region 4. Voids with radii up to 0.1 nm are unaffected, while the number of intermediate and large voids decreases. Here cholesterol removes the voids with $1\,\mathrm{nm}^3 \lesssim V \lesssim 3\,\mathrm{nm}^3$, larger than its own close-packed size.

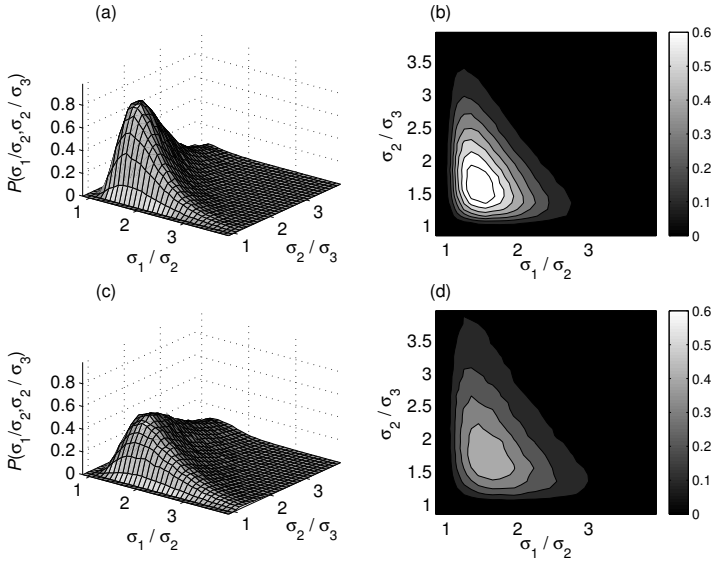

Figure 2.10. $P(\sigma_1/\sigma_2, \sigma_2/\sigma_3)$ at $\chi = 0\,\%$ and $\chi = 29.7\,\%$ in Region 3 [119]. The penetrant size is 0.05 nm. (a) Surface plot at $\chi = 0.0\,\%$. (b) Contour plot at $\chi = 0.0\,\%$. (c) Surface plot at $\chi = 29.7\,\%$. (d) Contour plot at $\chi = 29.7\,\%$. The relative errors are smaller than ten percent.

To characterize the effect of cholesterol on the shape of the voids with $4 \times 10^{-3}\,\mathrm{nm}^3 < V < 0.13\,\mathrm{nm}^3$, we focus on $P(\sigma_1/\sigma_2, \sigma_2/\sigma_3)$, the probability that a void has given values of σ_1/σ_2 and σ_2/σ_3. The distribution has been normalized such that integration over it gives unity. The behavior of $P(\sigma_1/\sigma_2, \sigma_2/\sigma_3)$ in Region 3 with $r = 0.05\,\mathrm{nm}$ is portrayed in Fig. 2.10. Cholesterol does not significantly influence the shape of the voids in any other region, and other penetrant sizes give very similar results. Panels (a) and (b) show the probability distribution for pure DPPC and panels (c) and (d) for a bilayer with $\chi = 29.7\,\%$. In both cases elongated voids dominate

the distribution; spherical or nearly spherical voids with $\sigma_1/\sigma_2 \approx \sigma_2/\sigma_3 \approx 1$ are rare. The presence of cholesterol makes the voids more elongated: larger values of σ_1/σ_2 and σ_2/σ_3 occur with a higher probability.

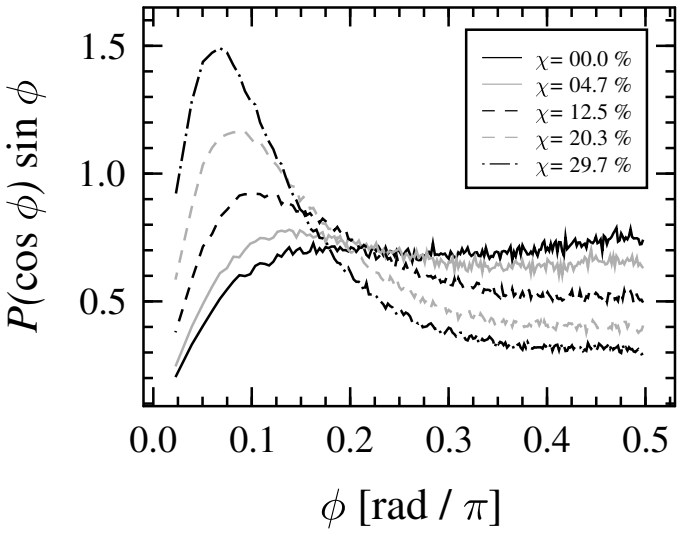

Figure 2.11. Orientational distribution $P(\cos\phi)\sin\phi$ in Region 3 for $r = 0.05\,\mathrm{nm}$ at different cholesterol concentrations [119]. The relative errors are of the order of five percent.

The impact of cholesterol concentration on the orientation of the elongated voids is most conspicuous in Region 3 and largely independent of r. The behavior of the orientational distribution $P(\cos\phi)\sin\phi$ with an increasing χ in the case of $r = 0.05\,\mathrm{nm}$ is portrayed in Fig. 2.11. In pure DPPC, angles $\phi > 0.1\pi$ are favored, while orientation along the bilayer normal, i.e. $\phi = 0$, hardly occurs at all. At $\chi = 29.7\,\%$, orientation along the bilayer normal or close to it is favored; alignment of the principal axis in the plane of the bilayer is rare. At cholesterol concentrations between 0 and $29.7\,\%$, the orientational distributions change systematically from one extreme to the other. In Region 4 the effects of cholesterol are less pronounced and depend on r, see Ref. [119].

The above conclusions on the properties of voids may be used for predicting how cholesterol influences, e.g., solute permeation across DPPC bilayers. The permeability of a solute depends on both its solubility into the bilayer, as well as its diffusion across it. As bilayers are heterogeneous in the normal direction, the solubilities and diffusion coefficients of solutes vary with the

position along the bilayer normal. This effect is captured by the so-called inhomogeneous solubility-diffusion model [81].

The permeability of a solute across a given bilayer depends on its size, shape, and hydrophobicity [81–84]. Here we are not so much interested in how the properties of solutes influence the permeation process across a given bilayer. Instead, we wish to make qualitative predictions about how an increasing cholesterol concentration affects the permeation of solutes.

Most solutes have radii at least of the order of 0.1 nm, and we will therefore concentrate on the regime without percolating clusters of free volume. In this case the influence of cholesterol on the properties of the voids is restricted to Region 3, where the cholesterol ring structures and DPPC tails are located. From a permeation point of view, too, Region 3 is very important [81]: this is where the largest resistance to the permeation of hydrophilic solutes, as well as the anomalous size dependence of permeability, originate.

In Region 3 the presence of 29.7 % cholesterol reduces the number of voids of all sizes. In addition, large voids comparable in size with cholesterol molecules are completely removed. An increasing cholesterol concentration also makes the voids in Region 3 elongated, and transforms the isotropic orientational distribution of voids in pure DPPC to an anisotropic one favoring orientation of the principal axes of the voids along the bilayer normal.

The reduced number of voids in Region 3 may affect both the solubility and diffusion of solutes. As $\chi = 29.7\,\%$ implies that the number of voids of all sizes $V < V_{\text{chol}}$ decreases at least by a factor of three and in most cases more, one would expect the solubility of *small hydrophilic* molecules in Region 3 to be reduced. As for diffusion, the matrix of voids is thought to be fairly static [81], and diffusion of small solutes therefore a series of jumps between neighboring voids [114]. Given a lower density of voids of all sizes, one would anticipate the diffusion coefficients of both hydrophobic and hydrophilic *small* solutes, with radii, say, less than 0.2 nm, to be suppressed. Concluding, $\chi \gtrsim 20\,\%$ should, compared with pure DPPC, significantly reduce the permeability coefficients of small solutes, more so for hydrophilic solutes than for hydrophobic ones.

The diffusion coefficients of larger molecules are expected to behave quite differently from those of small molecules. As the number of large voids is small for all values of χ, the diffusion of *larger* molecules may be of the

nonhopping type [81]. In this case the influence of the number of voids of various sizes on the diffusion coefficients and therefore also permeability is far from straight-forward.

The elongation and re-orientation of voids in Region 3 with an increasing χ may also affect the permeation of solutes. Consider first the case of two solutes with similar sizes and hydrophobicities, one of which is spherical and the other elongated. When χ grows, we expect the permeability coefficient of the elongated solute scaled by the permeability coefficient of the spherical solute to increase slightly. Further, the permeation of very small solutes of any shape may be speeded up by the more elongated voids oriented in the direction of the bilayer normal. In pure DPPC, with less elongated voids oriented mainly in the plane of the bilayer, small solutes have to jump between voids to cross the bilayer. With $\chi = 29.7\,\%$, in which case the voids are more elongated and aligned with the bilayer normal, the small solutes may diffuse unhindered within a void in the normal direction. This should slightly increase the permeability of the bilayer to small solutes. We expect this effect, at least for $\chi \gtrsim 20\,\%$, to be much less significant than the permeability-reducing effect of the smaller number of voids. Hence, our earlier conclusion that $\chi \gtrsim 20\,\%$ should suppress permeabilities holds. For low cholesterol concentrations, where the $N(V)$ are only slightly modified, the situation is less clear.

Experiments on large unilamellar vesicles show that water permeation in DMPC/cholesterol systems above the main phase transition is, compared with pure DMPC, suppressed for cholesterol concentrations 5–27 % [107]. The reduction in water permeability becomes truly significant when $\chi = 20-27\,\%$, in agreement with our predictions. Bhattacharya et al. [106] have examined the permeation of carboxyfluorescein in small unilamellar vesicles made of DMPC in the fluid phase, finding that a cholesterol concentration $\chi = 10 - 30\,\%$ noticeably reduces the permeability of the bilayer. Our predictions are also in accord with the experiments of Subczynski et al. [109], who have studied the permeation of water in bilayers consisting of saturated phosphatidylcholines and cholesterol.

The above discussion shows that more research into the detailed mechanisms of dynamic processes in DPPC/cholesterol bilayers is needed. In addition to the highly interesting mechanisms of lateral diffusion, and the role of voids in these, it would be interesting to study permeation in these systems.

3

Approaching Mesoscale: Systematic Coarse-Graining

3.1 From Atomistic to Coarse-Grained

Classical molecular dynamics currently allows us to study systems containing of the order of $10^5 - 10^6$ atoms. Converted to units of length and time this means, in membrane systems, roughly tens of nanometers and around ten nanoseconds, or five nanometers and hundreds of nanoseconds. If state-of-the-art hardware and simulation software are used, this translates to approximately one year of wall clock time on a single processor.

Lots of interesting phenomena in membranes take place at much larger scales, at the so-called mesoscale. By mesoscale we mean spatial and temporal scales between atomistic and macroscopic, say, in the range 10–1000 nm and 10–1000 ns. Examples of mesoscopic phenomena in membranes include domain formation, cooperative motions of lipids associated with phase changes, and bilayer fusion.

To study mesoscopic phenomena, we have to simplify or *coarse-grain* our classical atomic-scale models. This is analogous to what was discussed in Chapter 2: instead of QM models, in many cases of biological relevance classical atomic-scale models should be used. This leads us to the concept of multiscale modeling. The phenomena in, e.g., cells, tissues, or organs, taking place at a myriad of spatial and temporal scales, are best described by a hierarchy of techniques ranging from QM to continuum or finite element models. Ideally, these different levels of description should be connected by systematic links. The links could take us from microscopic to macroscopic or vice versa: in the former case we talk about coarse-graining and in the

latter about fine-graining. In the remainder of this Chapter, we will focus on coarse-graining.

The links from finer to coarser systems are by no means uniquely defined. There are different ways of systematically reducing the degrees of freedom in a given system [10, 146]. In addition, the degree or level of coarse-graining may vary: we may wish to coarse-grain our atomistic phospholipid description to point-particles in two dimensions, or opt for less coarse-grained phospholipids consisting of ten connected blobs. It all really depends on what we want to study with the resulting coarse-grained model. The essential idea, however, is to decide what kind of interacting coarse-grained particles would be useful for the problem at hand, and by some means, using information from a more microscopic level, derive the interactions between those coarse-grained particles.

The term coarse-graining is not exclusively reserved for the act of finding systematic ways to connect different levels of description. In some cases coarse-graining implies the construction of a phenomenological model containing fewer degrees of freedom than, say, an atomistic model. This kind of coarse-graining is by no means inferior to the systematic linking procedure, just different. Cleverly constructed coarse-grained models, which are general enough, can be used to study the generic properties of a wide variety of soft systems. We should, however, keep in mind that they are no faithful models of any particular system.

In the following the label 'systematic coarse-graining' will be used for the linking process described above, and 'coarse-graining' denotes the construction of any model where the smallest interacting units are larger than atoms. This categorization is, unfortunately, not very clear-cut. On one hand, some coarse-graining procedures are semi-systematic: at least some attempt has been made to mimic real systems, but the linking is far from systematic. A good example of such a case is the coarse-graining from QM models to classical atomic-scale models; ideally, the classical atomic-scale force fields could be derived from QM simulations alone. More examples will be mentioned below. On the other hand, even in atomic-scale models a single interacting unit can be larger than an atom, united atom force fields being a case in point.

In this Chapter we will come across both kinds of coarse-graining—systematic and phenomenological—and everything in between. The emphasis will, however, be on systematic coarse-graining. After describing

the state of the art of coarse-grained approaches in membrane systems, we will discuss systematic coarse-graining, focusing on a coarse-graining technique called inverse Monte Carlo (IMC) [20]. Finally we will describe the use of IMC in the DPPC/cholesterol system introduced in the previous Chapter.

3.2 Coarse-Graining in Membrane Systems

One of the first off-lattice coarse-grained bilayer models was introduced in the mid-1990s by Nielsen et al. [113, 147–149]. This phenomenological model is very useful in the study of lipid/sterol bilayers, most notably in the theoretical interpretation of their experimental phase diagrams. As phase behavior is targeted, the degree of coarse-graining must be high: lipids and sterols are hard-core particles with internal degrees of freedom. The model is a two-dimensional off-lattice one, and statistics are obtained from MC simulations. The model has also been used for studies of the effect of phospholipase A_2 on lipid bilayers [150].

Another phenomenological model with a high degree of coarse-graining, also describing lipid/sterol systems, but at the high-concentration solubility limit of cholesterol, has been published by Huang et al. [151,152]. It is somewhat similar to the model of Nielsen et al., the most notable difference being that Huang et al. use a lattice description as opposed to an off-lattice one. The aim of these computer experiments is to look for so-called superlattice structures in lipid/sterol bilayers, structures whose existence has been suggested by Somerharju et al. [153–156]. Superlattices of cholesterol are indeed observed, but this could be a lattice artifact [147]. These studies have been recently complemented by a two-dimensional off-lattice study with point-like lipids and sterols [157]. Even here superlattice structures are observed. The actual existence of superlattices, however, is at this point not established: the experimental evidence in favor of superlattices might be due to probes.

Moving towards less coarse-grained but still phenomenological models, we should mention the amphiphile simulations by Loison et al. [158, 159]. They have performed MD simulations of simple chain-like amphiphiles consisting of two hydrophilic and hydrophobic beads in an explicit solvent. Under suitable conditions, the amphiphiles self-assemble into a lamellar phase. Loison et al. have studied the thermal fluctuations [158] and pore

formation [159] in their self-assembled stack of bilayers, comparing their results to predictions of theoretical models.

A similar phenomenological model has been constructed by Lipowsky et al. [160, 161]. The details of the interactions differ from those in Refs. [158, 159], and in addition to flexible chain-like molecules, more complicated amphiphiles with tunable chain stiffness and either one or two tails are studied. Using a combination of MC and MD, Lipowsky et al. investigate the self-assembly and physical properties of their coarse-grained lipid membranes. Diffusion coefficients for water and amphiphiles, pressure profiles across the bilayer, as well as interfacial tensions and compressibility moduli are computed. An extension of the model [162] features two kinds of macromolecules, long lipid-like and short cholesterol-like amphiphiles.

Lipowsky's group has also developed a second phenomenological coarse-grained bilayer model [163]. This model is studied using dissipative particle dynamics (DPD) [164–166], and as often is the case in DPD simulations, the non-bonded interactions are soft, i.e., they do not have a hard core. The so far reported results include equilibrium structure properties and lateral stress profiles. The model is currently being used for studies of vesicle fusion, a topic far beyond the reach of atomistic MD simulations. Vesicle fusion of coarse-grained amphiphiles has also been investigated by Stevens et al. [167]. Their amphiphiles are a little less coarse-grained than those of Lipowsky et al., and they use MD rather than DPD. The model by Stevens et al. has also very recently been used for studies of bilayer assembly and structure [168].

The DPD methodology seems to be rather popular in coarse-grained bilayer studies; further examples of its use are the publications by Groot et al. [169] and Kranenburg et al. [170–172]. These two groups use essentially the same model, where the level of coarse-graining is very similar to that in Refs. [160, 161, 163]: an amphiphile consists of approximately ten coarse-grained particles. The model, however, is less phenomenological. The repulsive interaction parameters were originally chosen by Groot et al. [169, 173] to reproduce the compressibilities and mutual solubilities in the experimental soft systems to be modeled. Groot et al. [169] used their DPD model to qualitatively study systems consisting of lipids and nonionic surfactants, focusing on the rupture of the lipid bilayer with added surfactants. Kranenburg et al. [170–172], in turn, have been mostly preoccupied with interdigitation of amphiphiles in various circumstances.

The first more specific, rather than qualitative, coarse-grained model in our narrative is that of Shelley et al. [174–176]. They have constructed an interesting model for a DMPC bilayer in water, attempting to capture certain key properties of the water and lipid molecules known from experiments and atomistic simulations. For instance the force field parameters for the coarse-grained water molecules were tuned to match the melting temperature, vapor pressure, and density of real water. The most interesting part are the non-bonded, nonelectrostatic interactions between the coarse-grained particles comprising the DMPC molecules. The parametrization of these interactions was based on radial distribution functions (RDFs) from atomistic simulations. This model is therefore an example of semi-systematic coarse-graining, where at least part of the interactions originate from a more microscopic level. The coarse-grained lipid model has recently been used in simulations of the insertion and function of a nanosyringe in a bilayer [177].

The novel coarse-grained model designed by Marrink et al. [178] is another example of more quantitative approaches. Here, as in the case of Shelley et al., the parametrization is achieved by comparison to experimental and simulation results. The systematic or semi-systematic linking, however, is missing; the parameters are tuned such that the model yields results in accord with experiments and atomistic simulations. The construction is, in fact, very similar to that of classical atomic-scale force fields. The model is versatile: it can be used to model a variety of phospholipids, and it works well in both lamellar and nonlamellar—inverted hexagonal and micellar—phases. It is fast, giving the user a speed-up of more than three orders of magnitude compared to atomistic MD. Finally, it can be said to be at least semi-quantitative, with results in fair agreement with structural, elastic, dynamic, and thermodynamic data for a range of bilayers.

The perhaps most interesting venture so far is the systematic multiscaling effort for solvent/bilayer systems by Voth et al. [179–184]. The first publication in this ambitious series [179] introduces a methodology, the material point method, for interfacing "atomistic" MD with continuum dynamics. The "atomistic" bilayer simulations are not truly atomistic: for instance the lipids are ellipsoids with a dipolar charge distribution in one end. A second paper [182] consummates the project, replacing the simple water molecules and ellipsoidal lipids by fully atomistic pure DMPC and DMPC/cholesterol simulations. Another direction for Voth et al. is to bridge atomistic and DPD-like mesoscopic models. In Ref. [181] DPD is

cast in a new membrane formulation called elastic membrane DPD (EM-DPD). The interaction parameters between the mesoscopic particles, which are in a sense replicas of the original MD simulation box, are derived from atomistic MD and NEMD simulations [180]. An additional novel mesoscopic bilayer model from the Voth group is presented in Ref. [184]. One of the latest publication from Voth et al. [183] introduces a mesoscopic model for studying lateral diffusion in bilayers. Briefly, a probe is inserted to an atomistic MD simulation, and the dynamics of the probe is then used to construct a new coarse-grained model.

3.3 Systematic Coarse-Graining and Inverse Monte Carlo

Modeling soft condensed matter by a hierarchy of models rigorously connected to each other, each model being applicable over certain spatial and temporal scales, is indeed desirable. However, there is no unique rule for how this hierarchy should be constructed. As exemplified in Sec. 3.2, the choice of the coarse-grained particles depends on the objectives of the coarse-grained simulations. To study phase behavior in bilayers it is convenient to have a high degree of coarse-graining, the coarse-grained particles being whole lipids or sterols [113, 147–149]. On the other hand, in studies of vesicle fusion real three-dimensional amphiphiles with headgroups and tails are clearly needed [167]. Even after the coarse-grained particles have been defined, there is no unique way of deriving the interactions between these particles. Several techniques exist, see Refs. [31, 146] for further references.

Inverse Monte Carlo (IMC) [20, 185] is a method for obtaining interactions between coarse-grained particles using information from a more detailed description. The idea is to solve an inverse problem; to reconstruct the Hamiltonian of a system using canonical averages from either simulations or experiments. The corresponding direct problem is to, computationally or analytically, calculate averages for a system with a given Hamiltonian.

In isotropic systems, radial distribution functions (RDFs) are a convenient choice for the canonical averages to be used as a starting point for reconstructing the Hamiltonian $\mathcal{H}$. It has been shown [186] that two pair potentials that result in the same RDFs for a given system can differ from each other by only a constant. This constant can be fixed by the requirement that the potentials vanish at infinite interparticle distances.

In practise the reconstruction of the coarse-grained Hamiltonian from the RDFs is achieved iteratively. We assume for simplicity that our model contains only pairwise interactions and that all coarse-grained particles in our system are of the same kind. The Hamiltonian can then be written as

$$\mathcal{H} = \sum_{i,j;i\neq j} V(r_{ij}), \tag{3.1}$$

where the kinetic energy part has been left out. Here $V(r_{ij})$ is the so far unknown interaction potential for a pair of coarse-grained particles at a distance r_{ij} from each other.

To proceed it is convenient to work with discretized interaction potentials. Let us assume that the pairwise interaction potential $V(r)$ can be set to zero for $r > r_{\text{cut}}$, where r_{cut} is a cutoff distance. We divide the interval where $V(r)$ is finite to N_{bins} equally large bins, whose widths thus become $\delta r = r_{\text{cut}}/N_{\text{bins}}$. For $(\alpha-1)\delta r \leq r < \alpha\delta r$, $\alpha = 1, \ldots, N_{\text{bins}}$, we set $V(r) \to V_\alpha \equiv V[r_\alpha \equiv (\alpha - 1/2)\delta r)]$. The Hamiltonian can be written as

$$\mathcal{H} = \sum_{\alpha} V_\alpha S_\alpha, \tag{3.2}$$

where S_α is the number of pairs whose interparticle distance r satisfies the condition $(\alpha-1)\delta r \leq r < \alpha\delta r$.

The $\{S_\alpha\}_{\alpha=1}^{N_{\text{bins}}}$ are closely related to the RDFs. The RDF at a distance $r_\alpha = (\alpha - 1/2)\delta r$ is obtained by scaling the canonical average of S_α by the number of pairs with $(\alpha-1)\delta r \leq r < \alpha\delta r$ in an ideal gas with the same average density as that of the system under study. The scaling factor is dimension-dependent, e.g., in two dimensions we have:

$$g_\alpha \equiv g(r_\alpha) = \frac{\langle S_\alpha \rangle A}{\pi N(N-1)(\delta r)^2\left[\alpha^2 - (\alpha-1)^2\right]}, \tag{3.3}$$

where the angular brackets denote a canonical average, A is the total area of the system, and N is the number of particles.

Assume now that we have obtained $\{g_\alpha\}$ either experimentally or from, say, atomistic simulations. Using Eq. (3.3) we can compute the corresponding unscaled quantities, which we will call $\{S^*_\alpha\}$. The task of reconstructing the Hamiltonian now boils down to finding the $\{V_\alpha\}$ between the coarse-grained particles that yield $\{S_\alpha\}$ very close to the $\{S^*_\alpha\}$.

As the $\{S_\alpha\}$ must be functions of the pair potential, we can expand

$$\Delta\langle S_\alpha\rangle = \sum_\gamma \left\{ \frac{\partial\langle S_\alpha\rangle}{\partial V_\gamma}\Delta V_\gamma + \mathcal{O}\left[(\Delta V_\gamma)^2\right] \right\}, \tag{3.4}$$

where the sum is over all bins. The partial derivatives are easily obtained using basic statistical mechanics, more specifically the definition of a canonical average, arriving at

$$\frac{\partial\langle S_\alpha\rangle}{\partial V_\gamma} = \frac{1}{k_\mathrm{B}T}\left(\langle S_\alpha\rangle\langle S_\gamma\rangle - \langle S_\alpha S_\gamma\rangle\right). \tag{3.5}$$

Equations (3.4) and (3.5) allow us to iteratively find the final $\{V_\alpha\}$, or the so-called effective potential.

The iteration starts with an initial guess for the interaction potential, denoted by $\{V_\alpha^{(0)}\}$. It is usually a good idea to use the so-called potential of mean force as an initial guess:

$$V_\alpha^{(0)} = -k_\mathrm{B}T\ln g_\alpha. \tag{3.6}$$

If $g_\alpha = 0$, as is often the case at short distances, the initial guess can be a value a few orders of magnitude higher than the energy scales of the problem at hand. Note that the potential of mean force differs from the final outcome of the iteration, as the effective potential includes corrections from many-particle interactions.

We continue by performing an MC simulation using the $\{V_\alpha^{(0)}\}$ as a discrete interaction potential between the coarse-grained particles. The simulation results in the canonical averages $\{\langle S_\alpha\rangle^{(0)}\}$ and $\{\langle S_\alpha S_\gamma\rangle^{(0)}\}$. These can be inserted in Eq. (3.5) to obtain the partial derivatives in Eq. (3.4). Further, we can calculate the $\{\Delta S_\alpha^{(0)}\}$ on the left-hand-side of Eq. (3.4):

$$\Delta S_\alpha^{(0)} = \langle S_\alpha\rangle^{(0)} - S_\alpha^*. \tag{3.7}$$

The set of N_bins linear equations (3.4) can now be solved for $\{\Delta V_\alpha^{(0)}\}$, and a new interaction potential $\{V_\alpha^{(1)}\}$ emerges from

$$V_\alpha^{(1)} = V_\alpha^{(0)} + \Delta V_\alpha^{(0)}. \tag{3.8}$$

This potential is used in a second round of MC simulations, resulting in $\{\langle S_\alpha\rangle^{(1)}\}$ and $\{\langle S_\alpha S_\gamma\rangle^{(1)}\}$. The iteration progresses until the potential hopefully converges.

The algorithm is easily generalized to systems with K different kinds of particles [185], the main difference being that the notation becomes less elegant and the set of linear equations more challenging to solve with $N_{\text{bins}} \times K \times (K-1)/2$ equations.

The IMC technique is fairly novel, and has so far been used in only a few applications. Laaksonen et al. have utilized it to coarse-grain NaCl solutions [187–189] and ion-DNA systems [190]. Brunner et al. [191] have used it to determine the effective potentials in quasi-two-dimensional colloidal systems of charge-stabilized polystyrene spheres, comparing the IMC approach with a less rigorous way of deducing the effective potentials from RDFs: an inversion method based on the Ornstein-Zernike equations [191, 192]. Acuña-Campa et al. [193] have employed a method vaguely similar to IMC, also in quasi-two-dimensional colloidal systems. Their procedure is not explained in detail and seems to be less systematic than IMC. Also Shelley et al. [175], see Sec. 3.2, have used a technique reminiscent of IMC to construct a coarse-grained model of DMPC.

Techniques closely related to IMC are also gaining popularity in the field of computational polymer science, see Ref. [146] for a recent review. Several different systematic coarse-graining techniques where RDFs are used to derive effective potentials between coarse-grained particles have been devised. Examples of such methods are simplex mapping techniques [194, 195], as well as techniques that stem from the physics of the problem, e.g., the inverse Boltzmann technique [196,197], the structure-based coarse-graining approach introduced by Akkermans and Briels [198], and the semigrand canonical Monte Carlo method by Bathe and Rutledge [199].

3.4 Case Study: Coarse-Graining of DPPC/Cholesterol System

3.4.1 Motivation

As explained in Chapter 2, binary mixtures of DPPC and cholesterol show rich phase behavior. A particularly interesting feature in the phase diagram, see Fig. 2.1, is the **ld-lo** coexistence region. The coexistence region is expected to contain domains of **lo** and **ld** phases [200]. The size of these domains in DPPC/cholesterol bilayers or the very similar

DMPC/cholesterol bilayers has remained elusive. Quite recently, Loura et al. [200], using a combination of fluorescence techniques and MC simulation, were able to study the domain sizes in large unilamellar vesicles of DMPC/cholesterol. In the cholesterol-poor end of the phase diagram, they were able to detect small **lo** domains, with linear sizes less than 20–25 nm. In the cholesterol-rich end, the **ld** domains had larger sizes. We would expect this to apply to the DPPC/cholesterol system, as well.

Domains are perhaps not the only ordering phenomenon in fluid DPPC/cholesterol bilayers. As mentioned in Sec. 3.2, the existence of superlattice structures in these systems has been suggested [153–156, 201]. In brief, the superlattice model states that the sterols become maximally separated and regularly distributed in a hexagonal lipid matrix. Domains with hexagonal order are supposed to coexist with completely disordered domains [201]. At certain critical concentrations [154, 201], the ratio of regularly distributed and disordered domains is said to peak. Also other propositions exist. Nielsen et al. [148] have reported an observation of threadlike structures in their MC simulations. Cholesterols seem to form one-dimensional threads, which tend to be surrounded by lipids. The threads are short, consisting of only a few molecules, and their orientation does not show any long-range correlations.

Our aim is to study (quasi-)long-range structure in DPPC/cholesterol bilayers. As the domain sizes in the **ld-lo** coexistence region are expected to be of the order of tens of nanometers or larger, our computer model should be able to reach linear sizes of the order of hundreds of nanometers. The atomistic MD model discussed in Chapter 2 therefore has to be coarse-grained, and the degree of coarse-graining needs to be high. In the following, we will discuss the construction and validation of a planar, off-lattice, two-dimensional model, where each molecule is described by a point-like particle. More specifically, each DPPC and cholesterol molecule is represented by its CM position. The solvent degrees of freedom are integrated out, i.e., the model contains no explicit solvent. The interactions between the coarse-grained DPPC and cholesterol particles are derived from the RDFs of the atomistic system described in Sec. 2.5.2 using IMC.

3.4.2 Construction of Coarse-Grained Model

Let us first briefly state the underlying assumptions of our model, see Ref. [202] for more details. First, as we consider the upper and lower

monolayers of our original bilayer only weakly interacting, we focus on one monolayer only. Second, neglecting the out-of-plane fluctuations, we assume our monolayer to be strictly planar. We further assume that the interactions between DPPCs and cholesterols are adequately described using pairwise, radially symmetric effective potentials. Finally, we fix the area per molecule in the coarse-grained model, separately for each cholesterol concentration, to be the same as the average area per molecule calculated from the atomistic MD simulations [48]. The coarse-grained simulations are therefore conducted in the canonical ensemble.

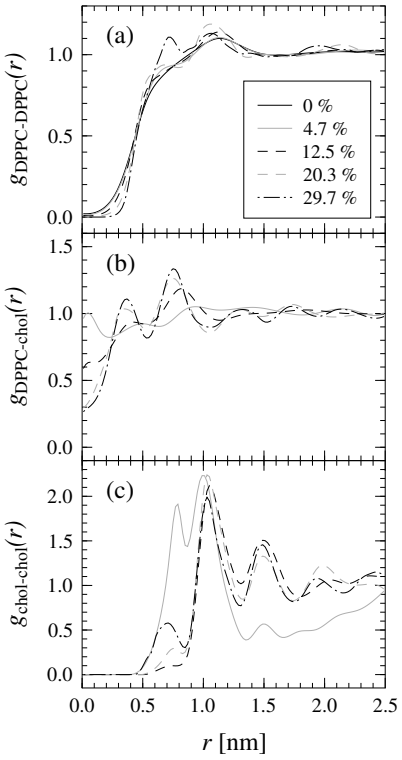

Figure 3.1. Two-dimensional RDFs from atomistic MD simulations for (a) DPPC-DPPC, (b) DPPC-cholesterol and (c) cholesterol-cholesterol pairs [202]. The errors are of the order of a few percent, only somewhat higher for the DPPC-cholesterol and cholesterol-cholesterol RDFs at $\chi = 4.7\,\%$. The curves have been smoothed using an algorithm from Ref. [203].

The interaction potentials for DPPC-DPPC, DPPC-cholesterol, and cholesterol-cholesterol pairs at cholesterol concentrations $\chi = 0 - 29.7\,\%$ are derived using the IMC technique outlined in Sec. 3.3. The input for

the IMC algorithm are the RDFs for the CM positions of the DPPCs and cholesterols computed from the atomistic simulations described in Sec. 2.5.2. The RDFs for DPPC-DPPC, DPPC-cholesterol, and cholesterol-cholesterol pairs at different χ are shown in Fig. 3.1. Note that these RDFs are two-dimensional, i.e., the CM positions of the molecules have been projected to the plane of the bilayer. The RDFs clearly indicate liquid-like behavior: the systems are, as they should, in the **ld**, **lo**, or **ld-lo** phase. As the cholesterol concentration increases, the range of ordering increases slightly and the maxima and minima become sharper.

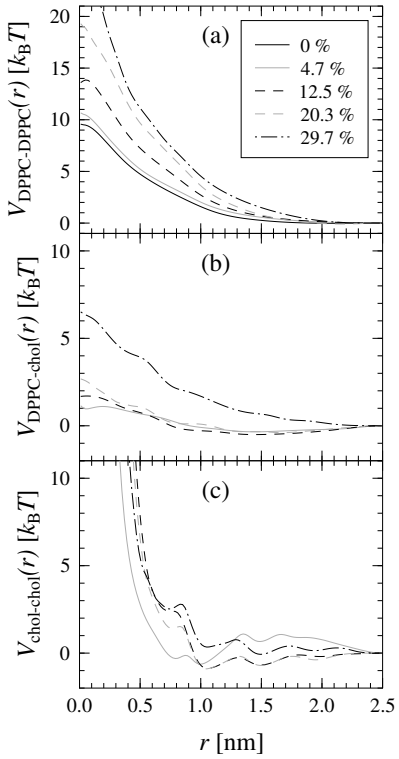

Figure 3.2. Effective potentials for (a) DPPC-DPPC, (b) DPPC-cholesterol, and (c) cholesterol-cholesterol pairs [202]. The curves have been smoothed using an algorithm from Ref. [203]. The errors are of the order of a few percent.

After approximately 50 iterations of IMC with the RDFs from Fig. 3.1 as input, the effective pair potentials converge. Wherever the RDFs vanish, i.e., at short interparticle distances r, the quantitative values emerging from the IMC procedure are meaningless. The exact values play no role

whatsoever, as the interparticle distances never become quite as short. The only requirement is that the values must be higher than at distances where the RDFs are finite. We can therefore, at distances where the RDFs vanish, replace the potential given by IMC by polynomials such that the potential and its first derivative are continuous at the edge of the region.

The potentials thus obtained, for different χ, are shown in Fig. 3.2. Because the degree of coarse-graining is high, the effective potentials decay rapidly. As a consequence of the two-dimensional nature of the RDFs, some of the DPPC-DPPC and all DPPC-cholesterol interactions are soft; they do not have a hard core. The DPPC-DPPC potentials are almost entirely repulsive at low cholesterol concentrations, and become more so with an increasing χ. The DPPC-cholesterol potentials at low cholesterol concentrations have an attractive well at $r \sim 1.5\,\mathrm{nm}$ and a very soft core. As χ increases, the well disappears and the potentials become more repulsive at short distances. The cholesterol-cholesterol potentials are harder than the other potentials and quite complex with multiple local minima. The cases $\chi = 4.7\,\%$, $\chi = 12.5\,\%$, and $\chi = 20.3\,\%$ have an attractive component at short distances, while the cholesterol-cholesterol potential at $\chi = 29.7\,\%$ is mostly repulsive.

An obvious way of verifying that the effective pair potentials really reproduce the original RDFs is to perform coarse-grained simulations using these potentials and compute the RDFs. As we are focusing on large-scale *structure*, we have chosen to use Metropolis MC in the canonical ensemble to calculate averages. Figure 3.3 shows a comparison of the RDFs from the atomistic MD simulations and those obtained from the coarse-grained MC simulations. The coarse-grained system contains the same number of lipid and sterol molecules as does the atomistic one. The two concentrations shown in Fig. 3.3 are representative of all the systems we have studied: the RDFs from atomistic and coarse-grained simulations are essentially identical. When the system size is increased, there are minor changes in the coarse-grained RDFs, see Ref. [202]. These changes are most probably finite-size effects that originate in the limited sizes of the original atomistic MD simulations. It is likely that atomistic simulations on larger systems would result in similar changes to the atomistic RDFs.

3.4.3 Ordering in DPPC/Cholesterol Bilayers

To observe the possible long-range ordering phenomena, the system size was raised from the original 64 molecules per monolayer to 36864 molecules per

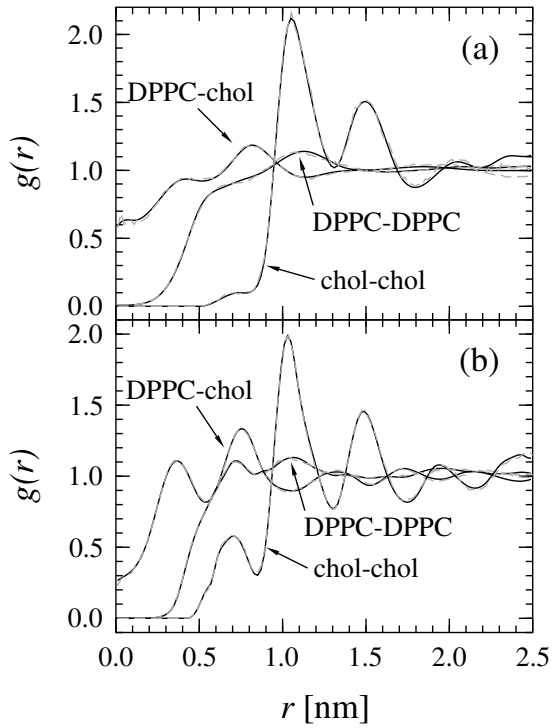

Figure 3.3. Comparison of RDFs from atomistic (solid black lines) and coarse-grained (dashed grey lines) simulations [202]. Two cholesterol concentrations are shown: (a) $\chi = 12.5\,\%$ and (b) $\chi = 29.7\,\%$. The errors are of the order of a few percent.

monolayer. This means simulating systems with linear sizes of 120–160 nm, 24 times larger than in the atomistic systems. Equilibration and sampling of the larger systems required 50–100 CPU hours on a desktop computer.

The static structure factor, also called the scattering function, is used in studying ordering by means of scattering experiments or simulations. For a system consisting of N particles with positions $\{\mathbf{r}_i\}$, the scattering intensity at the scattering vector $\mathbf{k} \equiv \mathbf{k}_f - \mathbf{k}_i$, $\mathbf{k}_i$ and $\mathbf{k}_f$ being the wave vectors of the incident and scattered beams, can be written as

$$S(\mathbf{k}) = \frac{1}{N^2} \sum_{i,j} \langle \exp\left[\imath \mathbf{k} \cdot (\mathbf{r}_i - \mathbf{r}_j)\right] \rangle. \tag{3.9}$$

In our system the wave vector $\mathbf{k}$ is two-dimensional. Since the structure factors are radially symmetric [202], we will discuss the circularly averaged structure factors $S(k)$. These are easier to visualize.

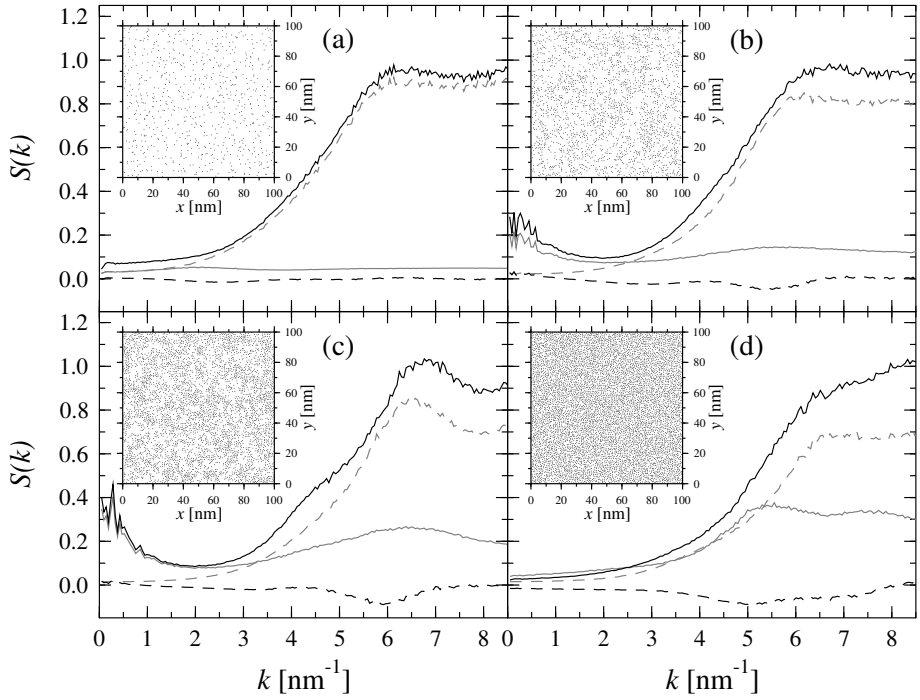

Figure 3.4. Static structure factors and snapshots of systems at different cholesterol concentrations: (a) $\chi = 4.7\,\%$, (b) $\chi = 12.5\,\%$, (c) $\chi = 20.3\,\%$, and (d) $\chi = 29.7\,\%$ [202]. In each panel, the structure factors computed for DPPC-DPPC (dashed grey), DPPC-cholesterol (dashed black), and cholesterol-cholesterol (solid grey) pairs, as well as the total structure factor computed for all pairs of particles irrespective of their molecular species (solid black), are shown. In the snapshots each cholesterol is represented as a dot, and DPPCs are not shown.

The structure factors have been calculated for DPPC-DPPC, DPPC-cholesterol, and cholesterol-cholesterol pairs, as well as for all pairs irrespective of molecular species. The circularly averaged structure factors at each cholesterol concentration, together with snapshots of the systems showing the positions of cholesterol molecules, are shown in Fig. 3.4. At $\chi = 12.5\,\%$ and $\chi = 20.3\,\%$, the snapshots suggest the existence of domains where the local cholesterol concentration is higher than elsewhere. At these concentrations the cholesterol-cholesterol structure factor has a rather broad maximum at small k, supporting our interpretation of the presence of cholesterol-rich and cholesterol-poor domains. The location of the maximum indicates domain sizes of approximately 20 nm or larger. Acquiring more

accurate figures is difficult. Even for the largest systems we have studied, with linear sizes of approximately 280 nm, the maximum is still quite broad, and the small k side of the peak is, because of fluctuations at large length scales, not very distinct. It is, however, possible to study how the maximum behaves if the system size is varied. To do so, we have computed the static structure factors for systems with linear sizes 6, 12, 24, and 48 times that of the original atomic-scale simulation box. This finite size scaling analysis indicates no clear changes in either the position or shape of the maximum.

According to the DPPC/cholesterol phase diagram, see Refs. [103, 104] and Fig. 2.1, the **ld-lo** coexistence phase is present above the main phase transition temperature and at intermediate cholesterol concentrations. The precise location of the phase boundaries is not known: phase diagrams constructed by different groups differ a little at this point. We cannot therefore state which cholesterol concentrations should be in the **ld-lo** coexistence phase at $T = 323\,\mathrm{K}$. Another complication is the underlying atomistic force field: it is simply not good enough to allow us to claim that we are *exactly* reproducing the experimental phase behavior of the system. Despite these reservations, the phase diagram does lend support to our observations.

As we have not included the ordering of the DPPC tails in our coarse-grained mode, we cannot directly distinguish between the **ld** and **lo** phases. Yet it is plausible that the cholesterol-rich phase should be **lo** and the cholesterol-poor **ld**. The ordering effect of cholesterol on the phospholipid tails has been clearly demonstrated: the higher the cholesterol concentration, the more ordered the tails [48, 49, 204]. This ordering effect appears to be local, i.e., the tails become more ordered in the vicinity of cholesterol molecules [204]. It is thus conceivable that the cholesterol-rich regions should be **lo**. Based on this reasoning, our coarse-grained systems with $\chi = 12.5\,\%$ and $\chi = 20.3\,\%$ are in the **ld-lo** coexistence phase. The linear sizes of the **lo** domains appear to be approximately 20 nm, in agreement with the sizes suggested by Loura et al. [200]. The other systems with $\chi = 4.7\,\%$ and $\chi = 29.7\,\%$ appear to be in single phases. According to the phase diagram the former must be in the **ld** phase and the latter in **lo**.

In addition to static structure factors, also other quantities were computed, see Ref. [202]. These studies shed no further light on the nature or size of the domains. Neither did we find support for the presence of superlattice structures [202]. This might be because our DPPC particles are radially symmetric. The occurrence of superlattices—if they exist, see Sec. 3.2—

could require a geometry with radially symmetric cholesterols and two radially symmetric hydrocarbon tails.

3.4.4 Remarks on Coarse-Grained Model

IMC clearly is a very appealing approach to systematic coarse-graining. It is adjustable: the level of coarse-graining and the number of degrees of freedom to be included are user-controlled. This allows the user to decide whether accuracy or speed is more critical, and design the model accordingly. We made a minimal model of the DPPC/cholesterol bilayer system, sacrificing a lot of detail to be able to look at mesoscopic systems at rather modest computational costs. The actual speedup of the coarse-grained model compared to the atomistic model was estimated to be eight orders of magnitude, see Ref. [202].

IMC is also general in the sense that it can be applied to a wide range of systems. The only prerequisite is that RDFs for pairs of coarse-grained particles should be ascertained from more microscopic simulations or experiments. This, however, could be a mixed blessing. It may imply that RDFs or other suitable canonical averages must, each time a new coarse-grained model is constructed, be acquired from, say, expensive atomistic simulations. On the other hand, this need not be true, since the coarse-grained potentials derived for a given system may be valid in related systems. For instance pair potentials determined at $\chi = 12.5\,\%$ might be valid at other concentrations, as well. We did investigate whether the effective potentials can be used at concentrations other than those at which they were determined [202]. The results indicate that they may be used at nearby concentrations. If phase boundaries are crossed, problems will indeed arise. This is not necessarily true for less coarse-grained models constructed using IMC.

Another problem was encountered when we attempted to study dynamic quantities such as lateral diffusion. Such studies cannot be conducted using Metropolis Monte Carlo; realistic dynamics has to be incorporated into the system. It is well known that this can be very challenging in coarse-grained systems. We found no simple way of including realistic dynamics into our coarse-grained model, see Ref. [202] for details.

In our opinion the benefits clearly outweigh the problems, and we plan to initiate further IMC-based studies. A possible line of development is

to include conformational degrees of freedom for the DPPCs. This could be done, in the spirit of Nielsen et al. [149], by giving each DPPC two possible states, ordered and disordered. Another modification is to include the two tails of the DPPCs as separate particles and possibly model the headgroup as a third particle. Such modified models should be compared to the minimal model to assess the possible benefits of the additional degrees of freedom, and to gain further insight into the coarse-graining process.

The IMC approach could also be applied to more complex bilayer systems. This, of course, requires input data from additional atomistic simulations. An interesting idea is to coarse-grain a sphingomyelin/cholesterol bilayer, and ultimately a phospholipid/sphingomyelin/cholesterol ternary mixture. The study of these ternary systems at large length scales should be rewarding, since such studies could help to explain the formation of lipid rafts [6–9]. Also simple bilayers containing proteins, and perhaps ternary lipid systems with proteins, should be feasible.

4

Coarse-Grained Dynamics

4.1 Complex Fluids and Coarse-Grained Dynamics

In this Chapter we must extend our rather loose definition of coarse-graining. So far, coarse-graining has been explained as follows. Starting from, say, an atomistic system, new coarse-grained particles or superatoms have been defined. By some means—using more or less systematic coarse-graining methods or intuition—interactions between these particles have been derived. In the following, we will also discuss *coarse-graining of solvent dynamics*. Coarse-graining will in this context, as previously, imply that details not necessary for the problem at hand are left out.

Imagine simulating a complex fluid such as a colloidal or polymeric solution, or as in Chapters 2 and 3, an amphiphilic mixture. Usually the goal of such simulations is to study the dynamics of the solute, e.g., the folding dynamics of a protein. The detailed motions of the solvent particles are in most cases much less interesting. In an MD simulation of a single polymer in solution, a decent-sized simulation box, preferably one whose linear size L is significantly larger than the radius of gyration of the polymer, is needed. Otherwise the finite size of the box will seriously affect the results. With, say, 10^2 monomers and 10^5 solvent particles, it is not hard to figure out that a substantially longer time is spent on resolving the solvent-solvent interactions than on resolving the monomer-monomer or monomer-solvent ones. As the most time-consuming part of an MD simulation is the force calculation, see Sec. 2.3, the solvent-solvent force computation is a bottleneck for the whole simulation.

Ideally, complex fluids should be studied on long time scales and over long distances. For instance folding a rather simple protein requires several

microseconds, in most cases more [18]. With small time steps, see Sec. 2.3, and an enormous amount of solvent-solvent force computations, the MD method with an explicit solvent becomes unfeasible.

A possible solution would be to integrate out the solvent altogether by means of, e.g., IMC. In systems where *hydrodynamic* or solvent-mediated interactions play an important role, this is a very bad idea. For instance in the case of polymer collapse in solution, in essence a simpler version of protein folding, hydrodynamic interactions have been shown to play a significant role in the collapse dynamics [205, 206]. We must therefore not remove the solvent, but coarse-grain it such that the exact hydrodynamic equations of motion for the conserved fields—mass, momentum, and energy—remain valid. A convenient way of achieving this is to model the solvent by stochastic rotation dynamics (SRD) [21, 22]. There are other methods that will lead to similar results, see e.g., Refs. [207, 208]. SRD, as we will see, has several appealing features.

Even though the solvent is coarse-grained, it would be desirable to preserve the microscopic character of the solute. Some monomers may be hydrophobic, others hydrophilic, and we may wish to include this information in our model. The word microscopic does not have to allude to an atomistic force field aimed at mimicking a specific system: any explicit pair or many-body interactions will do. The microscopic solute degrees of freedom should somehow be coupled to the coarse-grained solvent. This leads us to the MD/SRD hybrid model, where the solute is described using ordinary microcanonical MD and the solvent using SRD.

This Chapter is about modeling mesoscopic systems where hydrodynamic interactions are relevant. We will first explain the basics of the SRD and MD/SRD techniques, give references to analytical work on SRD, and review the applications where SRD has been used. Two two-dimensional simulation studies, a dilute polymer solution and a colloidal solution, where the MD/SRD algorithm has been exploited, will then be discussed.

4.2 Stochastic Rotation Dynamics and MD/SRD

Stochastic rotation dynamics, also known as multi-particle collision dynamics, real-coded lattice gas, or Malevanets-Kapral model, was first

introduced by Malevanets and Kapral [21,22]. In brief, SRD is a mesoscopic fluid model, where the fluid comprises particles with continuous positions and velocities. The system is coarse-grained into cells of a regular lattice, the simplest tessellation being a hypercubic grid with a mesh size a. The dynamics of the system consists of a superposition of streaming and collision steps. It can be shown that this dynamics conserves the momentum and energy in each cell, and gives a correct description of the hydrodynamics of the velocity field [21].

Assume a solvent consisting of N_b particles with positions $\{\mathbf{r}_i\}$ and velocities $\{\mathbf{v}_i\}$. During a streaming step at time t each particle i is propagated a distance $\tau\mathbf{v}_i(t)$, where τ is a discretized time step, also called the collision step. After the streaming step, the particles are sorted into cells: $\boldsymbol{\xi}_i(t+\tau)$ denotes the coordinates of the cell where particle i is found after the streaming step. The mean velocities $\mathbf{u}(\boldsymbol{\xi})$ of the particles in each cell $\boldsymbol{\xi}$ are then computed. The actual collision is performed by randomly rotating the relative velocity $\mathbf{v}_i(t) - \mathbf{u}[\boldsymbol{\xi}_i(t+\tau)]$ of each particle i. The velocities of the particles residing in the same cell are rotated by the same rotation matrix, while different cells have different randomly chosen matrices. The equations describing the dynamics read

$$\mathbf{r}_i(t+\tau) = \mathbf{x}_i(t) + \tau\mathbf{v}_i(t), \tag{4.1}$$

$$\mathbf{v}_i(t+\tau) = \mathbf{u}[\boldsymbol{\xi}_i(t+\tau)] + \boldsymbol{\omega}[\boldsymbol{\xi}_i(t+\tau)] \cdot \{\mathbf{v}_i(t) - \mathbf{u}[\boldsymbol{\xi}_i(t+\tau)]\}\,, \tag{4.2}$$

where $\boldsymbol{\omega}[\boldsymbol{\xi}_i(t+\tau)]$ is a random rotation matrix. Any random rotations consistent with detailed balance can be used. In two dimensions a rotation by either an angle $+\alpha$ or $-\alpha$, each with a probability $1/2$, is a typical choice. In three dimensions, rotation by $\pm\alpha$ around a randomly chosen unit vector is often used, see Refs. [209, 210] for a detailed explanation. Even other implementations of the collision step have been studied [209–211].

The above dynamics works well as long as the mean free path $\lambda = \tau\sqrt{k_\mathrm{B}T}$—a measure of the distance the particles travel between two collisions—of the particles is larger than the mesh size a. If this is not the case, e.g., at low temperatures, the particles in a given cell collide repeatedly with each other before any of the particles leaves the cell or new particles enter the cell [207, 212]. The first consequence is that Galilean invariance is broken [207]: transport coefficients measured in a system moving with velocity $\mathbf{U}$ will depend on $\mathbf{U}$. Second, a basic assumption in the analysis of Ref. [21], that of molecular chaos, meaning that particles have no memory of their earlier collisions, breaks down. Fortunately, there is a fix to these problems

suggested by Ihle and Kroll [212]. Before a collision all solvent particles are shifted by the same randomly chosen vector with components in the interval $[-a/2, a/2]$. This shift randomizes the collision environment of the particles, removing their memory of earlier collisions. After the collision, particles must be shifted back to their original positions. The collision step can now be written as

$$\mathbf{v}_i(t+\tau) = \mathbf{u}[\boldsymbol{\xi}_i^{\mathrm{s}}(t+\tau)] + \boldsymbol{\omega}[\boldsymbol{\xi}_i^{\mathrm{s}}(t+\tau)] \cdot \{\mathbf{v}_i(t) - \mathbf{u}[\boldsymbol{\xi}_i^{\mathrm{s}}(t+\tau)]\}\,, \qquad (4.3)$$

where $\boldsymbol{\xi}_i^{\mathrm{s}}(t+\tau)$ denotes the coordinates of the cell particle i has been shifted to.

Apart from the seminal Refs. [21, 22], there exist a few analytical and numerical studies of the SRD method. Ihle et al. [207, 210, 212–214] have presented a detailed analytical and numerical analysis of SRD with shifting. In Ref. [207] they complement the work of Malevanets and Kapral [22] by rederiving the equations of motion for the correlation functions of coarse-grained hydrodynamic variables. Also new Green-Kubo relations for the kinematic shear and bulk viscosities and the thermal transport coefficient are given: shifting introduces a new contribution to the Green-Kubo relations. In Ref. [213] approximate analytic expressions for the transport coefficients in two dimensions are derived and compared to numerical results. The long-time tails of velocity and stress autocorrelation functions in two dimensions are studied numerically and found to be in excellent agreement with mode-coupling predictions. This analytical and numerical analysis is extended to three dimensions in Ref. [210]. Finally, in Ref. [214], Ihle et al., inspired by Kikuchi et al. [208], refine their analytic approximations for the transport coefficients. Kikuchi et al. [208] have also studied transport coefficients in two and three dimensions, deriving analytic expressions for the kinematic shear viscosity and comparing these to numerical calculations where a shear has been applied to the system. Another series of studies is that of Gompper et al. [209, 211, 215–217], where flows in channels and around obstacles are studied numerically using SRD. Finally, Malevanets and Yeomans [218] and Hashimoto et al. [219] have employed the SRD algorithm to model binary fluid flow.

One advantage of SRD is that its rules are simple enough to allow analytical work that contains few approximations and compares favorably to numerics. Another advantage is that SRD can be easily coupled to a solute which is described using MD. Compared to, e.g., combining MD and Lattice-Boltzmann approaches [220], the MD/SRD hybrid method introduced by Malevanets and Kapral [22] is easy to describe and implement.

We now introduce solute particles with continuous positions and velocities to the hydrodynamic bath of solvent molecules. The solute-solute and solute-solvent interactions, E_{ss} and E_{sb}, can be chosen as in MD, while the interaction potential E_{bb} between two solvent particles is always zero. Instead of undergoing free streaming described by Eq. (4.1) between collisions, the system evolves according to Hamilton's equations of motion, see Eqs. (2.7) and (2.8), where we set $E = E_{\mathrm{ss}} + E_{\mathrm{sb}}$. As $E_{\mathrm{bb}} = 0$, unless solvent particles interact with solutes, their motion is reduced to free streaming. The effective solvent-solvent interactions take place as multi-particle collisions at intervals of τ: the velocities of the solvent particles are transformed according to Eq. (4.2) or (4.3).

Especially in the case of dilute solutions, the hybrid MD/SRD introduced in Ref. [22] significantly reduces computation times of ordinary MD simulations. An even faster variant of the hybrid algorithm has been introduced by Malevanets and Yeomans [221]. In this case also the direct solute-solvent interaction is absent: it is described indirectly through collisions.

Let us briefly list the MD/SRD applications, either with or without explicit solute-solvent interactions, published so far. Malevanets and Kapral chose to demonstrate the use of their novel hybrid model by simulating nanocolloidal particles in solution [22]. In a later publication, Lee and Kapral [222] studied the structural and dynamic properties of clusters of nanocolloidal particles in an SRD solvent. Yeomans et al. have studied the dynamics of short polymer chains in dilute solutions [221] and the collapse of a single polymer chain in solution [205]. Ripoll et al. [223] have, too, studied short polymer chains in solution. Approaches to combining a solute and an SRD solvent that differ from the MD/SRD presented in Refs. [22, 221] have been put forward by Ohashi et al. [224, 225].

The above discussion might suggest that SRD/MD simulations are simple indeed. In a way, they are: modifications required to existing MD codes are rather minor. On the other hand, a lot of insight and work are needed to design, and in particular, to parametrize a sensible SRD/MD simulation. The parameters that determine the collision dynamics—the mesh size a, the collision step τ, and the rotation operator—influence the properties of the coarse grained solvent, e.g., its viscosity and Schmidt number, see Sec. 4.4.2. Also spatial and temporal scales inherent to the problem at hand are part of the equation: for instance τ should be chosen small enough to correctly describe the effect of solvent dynamics on solute particles [22].

The choices are not independent of each other; if a is altered, the solvent viscosity is affected, and we might have to reconsider the choice of τ to make sure the hydrodynamic interactions between the solute particles are described correctly. A more comprehensive discussion on parametrization can be found in Ref. [226]. In the following we will describe our MD/SRD studies in two dimensions, and illustrate how MD/SRD studies are designed and executed in practise.

4.3 Case Study: Two-Dimensional Polymer in Solution

4.3.1 Anomalous Dynamic Scaling?

The MD/SRD method is not yet quite ready to be used in modeling specific systems such as a β-hairpin from protein G, or a strand of DNA with a bunch of counterions, in water. It is, however, already a very useful tool in generic, phenomenological simulations that capture the behavior of a large range of systems. A good example of such systems is a two-dimensional polymer in a solvent with full hydrodynamics [227].

The dynamics of a two-dimensional polymer in solution, unbelievable as it may sound, is a very controversial issue. The corresponding three-dimensional system is well understood; simulations and experiments support the existing theories for polymer dynamics in three dimensions [19, 228]. The dispute in two dimensions has to do with the theory of dynamic scaling, a fundamental theory describing the dynamics of polymers [19]. To understand what the debate is all about, we have to briefly discuss the static and dynamic scaling for polymers in dilute solution.

There are three key quantities to consider. The first is the radius of gyration, a measure of the area or volume the polymer occupies. It is defined as

$$R_{\mathrm{g}} \equiv \sqrt{\frac{1}{N}\sum_{i=1}^{N}\langle(\mathbf{r}_i - \mathbf{R}_{\mathrm{CM}})^2\rangle}, \tag{4.4}$$

where N is the degree of polymerization, $\{\mathbf{r}_i\}$ are the positions of the monomers, and $\mathbf{R}_{\mathrm{CM}}$ is the CM of the polymer. A second important

quantity is the CM diffusion coefficient of the polymer

$$D_{\mathrm{CM}} \equiv \lim_{t\to\infty} \frac{1}{2dt}\langle[\mathbf{R}_{\mathrm{CM}}(t) - \mathbf{R}_{\mathrm{CM}}(0)]^2\rangle, \tag{4.5}$$

where d is the dimensionality of the system. A third central quantity is the intermediate scattering function, the time correlation function of the intensity of the scattered light from scattering experiments, see Eq. (3.9),

$$S(\mathbf{k}, t) \equiv \frac{1}{N}\sum_{i,j}\langle\exp\left[\imath\mathbf{k}\cdot(\mathbf{r}_i(t) - \mathbf{r}_j(0))\right]\rangle, \tag{4.6}$$

where $\mathbf{k}$ is a wave vector.

The radius of gyration and the CM diffusion coefficient scale with the degree of polymerization as

$$R_{\mathrm{g}} \sim N^{\nu} \tag{4.7}$$

and

$$D_{\mathrm{CM}} \sim N^{-\nu_{\mathrm{D}}}, \tag{4.8}$$

where ν and ν_{D} are *universal* scaling exponents. The circular average of the intermediate scattering function, see Sec. 3.4.3, scales as

$$S(k, t) \sim k^{-1/\nu}F(tk^x) \tag{4.9}$$

for $k \in (2\pi/R_{\mathrm{g}}, 2\pi/b)$, where b describes the size of a monomer. The new exponent x, the so-called dynamic scaling exponent, is related to ν and ν_{D} through

$$x = 2 + \frac{\nu_{\mathrm{D}}}{\nu}. \tag{4.10}$$

Equations (4.9) and (4.10) are the cornerstones of dynamic scaling of polymers, and they should hold true in all dimensions $d > 1$.

Universality implies that the values of the two exponents ν and ν_{D} should capture the generic behavior of any polymer system. Details such as the chemistry of the polymers are largely insignificant in this respect. Only three properties dictate the exponent values: dimensionality, whether or not excluded volume interactions play a role, and whether or not hydrodynamic interactions are present. For instance DNA molecules confined to the surface of a fluid lipid membrane [229] form a two-dimensional system where excluded volume interactions, but not hydrodynamic interactions, are significant. The exponents are, as we shall see, in excellent agreement with simple scaling theories: $\nu = 0.79 \pm 0.04$ and $\nu_{\mathrm{D}} = 0.95 \pm 0.06$ [229].

The Rouse model [19] describes systems with neither excluded volume effects nor hydrodynamic interactions. In systems without excluded volume interactions, only monomers that are close neighbors along the chain interact with each other. This scenario is valid for polymer melts. In the absence of excluded volume interactions $\nu = 1/2$ in all dimensions [19]. The exclusion of hydrodynamic interactions leads to $\nu_{\mathrm{D}} = 1$, regardless of dimensionality or the presence of excluded volume interactions [19] . Hence, according to Eq. (4.10), we must have $x = 4$.

Excluded volume interactions, that are screened in polymer melts, are crucial in describing systems such as a polymer chain in solution [19]. In such cases steric interactions should be taken into account: as real monomers have finite sizes, two monomers cannot come arbitrarily close to each other. If excluded volume effects are taken into account, ν becomes dimension-dependent, $\nu \approx 0.75$ in two and $\nu \approx 0.59$ in three dimensions [19, 230].

In a model that features excluded volume interactions, but no hydrodynamic interactions, we have a dimension-dependent ν and, as in the Rouse model, $\nu_{\mathrm{D}} = 1$. In this case Eq. (4.10) gives $x \approx 2.75$ in two and $x \approx 2.59$ in three dimensions. An example of a system best described by such a model is DNA on the surface of a fluid lipid membrane, see above. Hydrodynamic interactions are not present because of the experimental setup; a glass plate supporting the membrane makes the system dissipative.

The Zimm model [19], which takes the hydrodynamic interactions into account, is the model of choice for describing polymer chains in solution. The model can be formulated either with or without excluded volume interactions. In both cases, $\nu_{\mathrm{D}} = \nu$ in three dimensions [19], and we have $\nu = \nu_{\mathrm{D}} = 1/2$ without and $\nu = \nu_{\mathrm{D}} \approx 0.59$ with excluded volume interactions. Thus $x = 3$, irrespective of the presence of excluded volume interactions.

The problem arises in the two-dimensional case with hydrodynamics. Vianney and Koelman [231] state that in the so-called non-draining limit the polymer should behave as an obstacle around which the solvent must go. Hence in three dimensions the CM diffusion coefficient should scale as that of a spherical particle, inversely proportional to the size of the particle. This is exactly what the Zimm model predicts: $\nu_{\mathrm{D}} = \nu$ or $D_{\mathrm{CM}} \sim R_{\mathrm{g}}^{-1}$. Analogously, in two dimensions D_{CM} should scale as the diffusion coefficient of a disk-like particle. In practise, this implies that D_{CM} should, in two dimensions, depend *logarithmically on the size of the*

particle and the linear size of the system. The lattice-gas simulations of Vianney and Koelman, however, suggest that in two dimensions with excluded volume and hydrodynamics $\nu = 0.75$ and $\nu_{\mathrm{D}} = 0.78 \pm 0.05$. After demonstrating that their simulations suffer from no artifacts, but without any finite size scaling analysis, the authors pronounce that two-dimensional hydrodynamics "cannot be described within the nondraining concept".

Shannon and Choy [232] think along similar lines. They use MD to study the scaling of $S(k,t)$ in two dimensions with excluded volume and hydrodynamic interactions, arriving at $\nu = 0.72$ and $x = 2$. The latter they call "a value not predicted by the Rouse or Zimm models", a statement which would certainly be correct in *three dimensions*. The result $x = 2$ should, according to Eq. (4.10), imply that $\nu_{\mathrm{D}} = 0$, i.e., logarithmic scaling of D_{CM} with N, in agreement with the original hypothesis of Vianney and Koelman. Shannon and Choy have also studied the scaling of D_{CM} with N, with confusing results. Their MD simulations suggest that $\nu_{\mathrm{D}} > 0$, contradicting the scaling theory. They have also numerically solved the Zimm equations in two dimensions, verifying that $x = 2$, but finding that now $\nu_{\mathrm{D}} < 0$. These results prompt the authors to suggest that dynamical scaling is *broken* for two-dimensional polymers. Their preliminary re-examination of the two-dimensional dynamic scaling theory lends support to this suggestion. Unfortunately neither their simulations nor their theory take into account finite size effects, in the latter case resulting in formulae that make little sense from the point of view of dimensional analysis.

In the following, we will describe the use of the MD/SRD hybrid model in verifying the validity of dynamical scaling for two-dimensional polymers. We have extracted the exponents ν, ν_{D}, and x through extensive mesoscopic simulations of a two-dimensional polymer with excluded volume and hydrodynamic interactions. In particular, we have been able to carefully consider the system size dependence of the CM diffusion coefficient. An extensive finite size scaling analysis would have been impossible with a conventional MD solvent.

4.3.2 Model System

We simulated a polymer chain immersed in a two-dimensional solvent. The chain was described using MD and the solvent using SRD, resulting in an MD/SRD hybrid model. The monomer-monomer interactions were

modeled by truncated Lennard-Jones (LJ) potentials, also called WCA potentials [233]:

$$U_{\text{Lennard-Jones}}(r) = \begin{cases} 4\epsilon \left[\left(\frac{\sigma}{r}\right)^{12} - \left(\frac{\sigma}{r}\right)^{6} \right] + \epsilon, & r \leq 2^{1/6}\sigma; \\ 0, & r > 2^{1/6}\sigma. \end{cases} \tag{4.11}$$

In some of the simulations the monomer-solvent interactions, too, were described by truncated LJ potentials. However, computing the CM diffusion coefficients was very time consuming, and in that case the monomer-solvent interaction potentials were set to zero and the monomers included in the collision dynamics, see Sec. 4.2. In addition to the LJ potentials, nearest-neighbor monomers interacted through anharmonic, attractive FENE potentials [234]

$$U_{\text{FENE}}(r) = -\frac{cR_0^2}{2} \ln\left(1 - \frac{r^2}{R_0^2}\right), \tag{4.12}$$

where $c = 7\,\epsilon\,\sigma^{-2}$ and $R_0 = 2\,\sigma$.

The mass of a solvent particle was set to m and the mass of a monomer was $2\,m$. The parameters σ and ϵ together with m define the LJ unit system, where the unit of time is defined as $\tau_{\text{LJ}} \equiv \sigma\sqrt{m/\epsilon}$.

The mass density of the solvent was set to $\rho_{\text{b}} = 0.581\,m\sigma^{-2}$ and the temperature to $k_{\text{B}}T = 1.2\,\epsilon$. Hamilton's equations of motion were integrated using the velocity Verlet algorithm with a time step $\delta t = 0.005\,\tau_{\text{LJ}}$. The size of the polymer chain was from 20 to 150 monomers, and the linear size of the system L from $40\,\sigma$ to $420\,\sigma$. Periodic boundary conditions were employed.

The central parameters of the SRD collision dynamics, the mesh size and the collision step, were chosen to be $a = 2\,\sigma$ and $\tau = \tau_{\text{LJ}}$. The mesh size was a compromise. On one hand, it is inefficient to have, on the average, very few colliding particles in a cell. On the other hand, to prevent correlations in the intermediate-time dynamics of the monomers, a cell cannot accommodate a large number of monomers, especially if monomer-solvent interactions are modeled through collisions. The mean free path was approximately as large as the mesh size, and hence no grid shifting was implemented. The random rotation angles were selected from a uniform distribution in $[0, 2\pi)$. These choices result in a solvent shear viscosity $\eta \approx 1\,m\tau_{\text{LJ}}^{-1}$.

The value of the shear viscosity is needed to determine a lower bound for the length scales that can be modeled reasonably accurately. The

hydrodynamics is not adequately described on time scales smaller or of the order of the collision step τ [22]; time scales of $\tau_{\mathrm{H}} = 3 - 5\,\tau$ are the smallest to be considered. As the kinematic shear viscosity η/ρ_{b} is the diffusivity of momentum [17], the distance traveled by momentum during a time interval τ_{H} is approximately $\ell \sim \sqrt{\eta\tau_{\mathrm{H}}/\rho_{\mathrm{b}}}$, in our case $\ell \approx 3\,\sigma$. This implies that the description of dynamic quantities with $k = 2\,\pi/\ell < 3\,\sigma^{-1}$ should be valid. Hence, the CM diffusion coefficient and the scaling of the intermediate scattering function, see Fig. 4.2 for details, can be studied using this parametrization of MD/SRD.

4.3.3 Scaling from Stochastic Rotation Dynamics Simulations

In this Section we shall, for convenience, drop the dimensions from R_{g}, D_{CM}, k, and so on. First we establish that the excluded volume interactions are correctly included in our model. This can be done, e.g., by checking the scaling of R_{g} with N. This scaling is portrayed in Fig. 4.1. The slope of $\ln R_{\mathrm{g}}$ vs. $\ln N$ gives $\nu = 0.76 \pm 0.01$, as it should.

We proceed by verifying the result of Shannon and Choy [232] for the dynamic exponent x. The scaling of the intermediate scattering function is depicted in Fig. 4.2. The scaling relation (4.9) implies that if the exponents ν and x are chosen correctly, all $k^{1/\nu}S(k,t)$ vs. $k^x t$ should collapse on a single curve. As ν is already fixed, we may only vary the dynamic exponent. The best data collapse is obtained with $x = 2.0 \pm 0.1$.

Having verified that $\nu \approx 0.75$ and $x \approx 2$, we focus on the controversial exponent ν_{D}. For a detailed account on how to define and compute transport coefficients such as D_{CM} in two dimensions, see Sec. 4.4 and Refs. [226, 227]. As the nondraining argument of Vianney and Koelman suggests, it is not enough to study D_{CM} as a function of N or R_{g} for a fixed system size L. Instead, both N and L should be varied to detect the possible logarithmic scaling with the chain and system sizes.

Using the so-called memory expansion technique [235], we first determined D_{CM} for fixed $N \in [20, 80]$ with varying L. For instance in the case of $N = 30$ we considered the system sizes $L \in \{60, 90, 120, 150, 180, 210, 240\}$. For each N, D_{CM} was found to be linearly proportional to $\ln(b/L)$. The conventional trick, which is used in three dimensions where $D_{\mathrm{CM}} \sim b/L$, would be to let $L \to \infty$ and thus extrapolate an asymptotic value for D_{CM}.

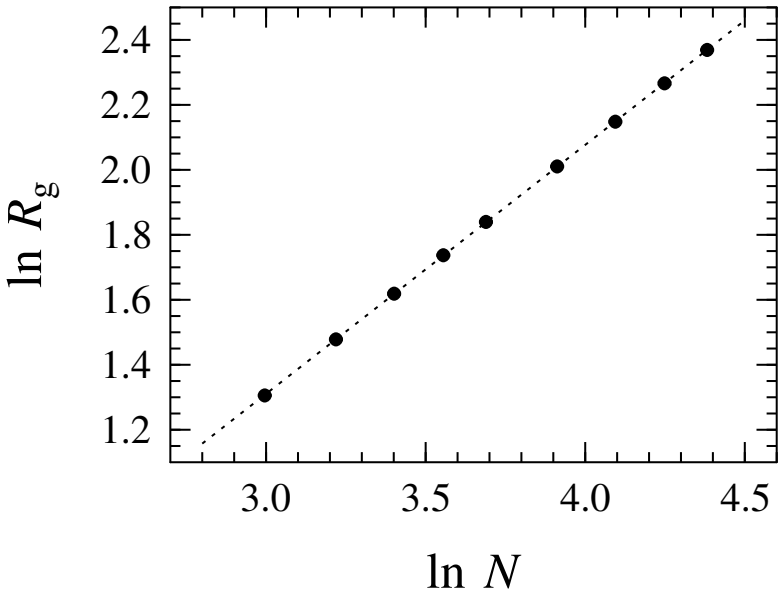

Figure 4.1. Scaling of radius of gyration with degree of polymerization. The closed circles are the simulation data and the dashed line is a linear fit to the data. The errors are of the order of a few tenths of a percent.

With the logarithmic dependence, however, this is no option. We therefore chose cutoff values $L_{\mathrm{cut}} \in \{10^2, 10^3, 10^4, 10^5, 10^6\}$ and extrapolated a value $D_{\mathrm{CM}}(N, L_{\mathrm{cut}})$ for each chain size and cutoff.

If our data complies with Eq. (4.8), we will, when plotting $D_{\mathrm{CM}}(N, L_{\mathrm{cut}})$ vs. $\ln N$, obtain a set of equally spaced straight lines. Each line should correspond to a given value of L_{cut}, and the lines should all have the same slope. As panel (a) of Fig. 4.3 shows, this indeed is the case within the statistical uncertainties of our data. Hence, D_{CM} scales logarithmically with N or R_{g} and L,

$$D_{\mathrm{CM}} \sim -\ln\left(\frac{R_{\mathrm{g}}}{L}\right), \tag{4.13}$$

which, in the language of scaling, means that $\nu_{\mathrm{D}} \approx 0$. To quantify the last statement, we may examine the slopes of $\ln D_{\mathrm{CM}}(N, L_{\mathrm{cut}})$ vs. $\ln N$ for different values of L_{cut}. Taking logarithms on both sides of Eq. (4.13), using $R_{\mathrm{g}} = bN^{\nu}$ [19], and Taylor-expanding shows that for large values of L_{cut} we should have $\ln D_{\mathrm{CM}} \sim -\ln N / \ln(L/b)$. On the other hand, according to Eq. (4.8), $\ln D_{\mathrm{CM}} \sim -\nu_{\mathrm{D}} \ln N$. Hence, the larger the value of L_{cut} is, the

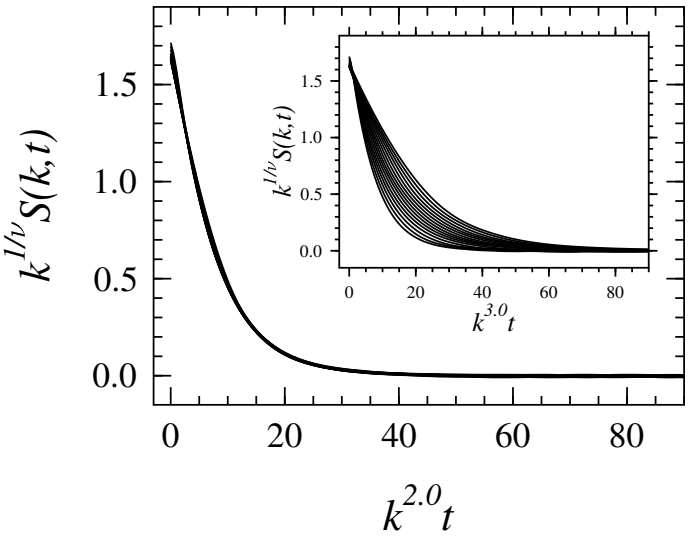

Figure 4.2. Scaling of $S(k,t)$ for different values of N, L, and k [227]. Part of the curves represent chains with $N \in \{30, 40, 60, 80, 120, 150\}$, computed such that the ratio $L/R_\mathrm{g} > 10$ has been kept constant. The rest has been computed for a chain of $N = 40$ with different $L \in \{40, 80, 120, 60, 200\}$. When $x = 2$ the 120 curves corresponding to different $k \in [1.0, 2.4]$, N, and L coalesce. The inset shows a scaling plot of $S(k,t)$ with $x = 3$. This curve has been computed for a system where $N = 40$ and $L = 120$.

closer to zero the slope of $\ln D_\mathrm{CM}(N, L_\mathrm{cut})$ vs. $\ln N$, or the exponent ν_D, should be. Panel (b) of Fig. 4.3 shows that ν_D decreases steadily with L_cut, as it should. For the largest L_cut studied here, we find $\nu_\mathrm{D} \approx 0.05 \pm 0.05$.

Our numerical evidence for the behavior of the CM diffusion coefficient can be backed up by analytical arguments based on the Zimm theory in two dimensions. The preliminary theoretical results for D_CM we published in Ref. [227] have recently been refined [4]. The Zimm-model based analytical calculations of Punkkinen et al. [4] clearly show that D_CM scales logarithmically with R_g/L. Furthermore, a quantitative comparison of the numerical and analytic results is possible. Plugging in numbers to the analytic prediction of Ref. [4] yields $D_\mathrm{CM} = 0.1\,\sigma^2\tau_\mathrm{LJ}^{-1}\ln(R_\mathrm{g}/L)$. The data displayed in Fig. 4.3 give $D_\mathrm{CM} = 0.1\,\sigma^2\tau_\mathrm{LJ}^{-1}\ln(R_\mathrm{g}/L)$, in excellent agreement with the analytic prediction.

We conclude that there is no reason to suppose that dynamic scaling should be broken in two dimensions. Analytic predictions [4, 230] for the scaling exponents in two dimensions, with excluded volume and hydrodynamic

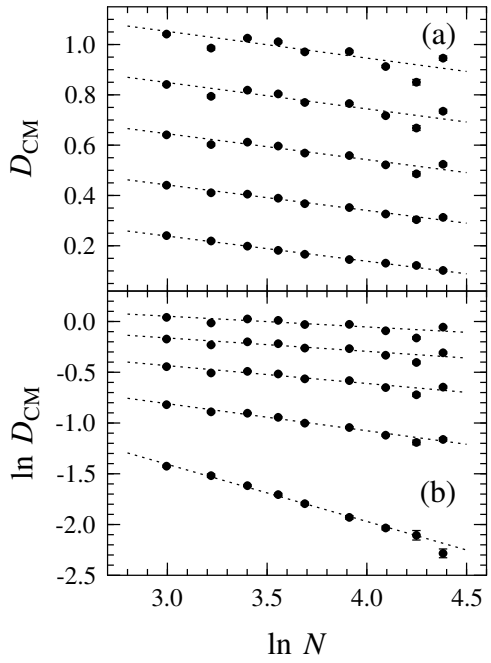

Figure 4.3. Dependence of D_{CM} on N for different cutoffs L_{cut} [227]. The sets of data correspond to $L_{\mathrm{cut}} \in \{10^2, 10^3, 10^4, 10^5, 10^6\}$ from bottom to top. The closed circles are the simulation data and each dashed line is a linear fit to the data set with a given L_{cut}. The errors, where invisible, are smaller than the markers.

interactions, are $\nu \approx 0.75$, $\nu_{\mathrm{D}} \approx 0$, and $x \approx 2$. By correctly taking into account the effect of system size, these exponents can be obtained from numerical simulations.

4.4 Case Study: Two-Dimensional Colloidal Diffusion

4.4.1 Introduction to Colloid Dynamics in Two Dimensions

In this Section we will continue discussing two-dimensional transport phenomena in soft systems. Instead of polymers in solution, we will study diffusion in two-dimensional nanocolloidal systems, and in particular, the

role of hydrodynamic interactions in colloid dynamics. Colloids in confined geometries are attractive from both experimental and modeling points of view. Experiments are quite convenient, since two-dimensional trajectories of colloidal particles can be followed using video imaging [236]. Interesting issues, such as the form of the effective pairwise interactions between colloidal particles [191–193] or the effect of hydrodynamics on tracer diffusion of colloidal particles [237–244], are currently under debate. Our emphasis will be on *tracer and collective diffusion* of colloidal particles in solution, at finite particle densities and with full hydrodynamic interactions.

Quite a few groups studying colloidal diffusion in confined geometries have focused on tracer or self diffusion. Even if the hydrodynamic interactions are neglected, understanding tracer diffusion of Brownian particles at finite densities is far from trivial, see, e.g., Refs. [245–247]. Taking the hydrodynamic interactions into account further complicates the situation. In quasi-two-dimensional colloidal systems, hydrodynamic interactions have been suggested to slow down tracer diffusion of colloidal particles with short-range interactions [237, 238, 242, 243]. On the other hand, in quasi-two-dimensional colloidal suspensions where interactions are softer and more long-ranged, the presence of hydrodynamic interactions appears to speed up tracer diffusion [238–241, 244].

Much less is known about collective or chemical diffusion in two-dimensional colloidal suspensions. The collective diffusion coefficient measures the decay rate of density fluctuations in a system. Hence, it is an important quantity in describing processes such as spreading and phase separation. There is evidence that hydrodynamic interactions do influence density fluctuations in confined colloidal systems, see Refs. [238–240, 242, 243]. These publications describe the effect of hydrodynamic interactions on the exponential *short-time* decay of the intermediate scattering function. This effect is captured by the so-called hydrodynamic function $H(k)$ [248], which is unity in the absence of hydrodynamic interactions. It appears that hydrodynamic interactions contribute differently to the short-time relaxation of particle fluctuations at different reciprocal length scales k, and that the deviations from unity become more major with an increasing density. Measurement or computation of the actual collective diffusion coefficients in colloidal suspensions has, to our knowledge, not yet been reported. Numerical data for collective diffusion coefficients exist in the absence of hydrodynamic interactions for the case of Brownian particles with short-range direct interactions [246].

We have studied tracer and collective diffusion in two-dimensional nanocolloidal suspensions by means of extensive MD/SRD simulations. The direct interactions between our model colloids are short-ranged and repulsive. The efficient MD/SRD method allows us to consider a wide range of particle densities and investigate how hydrodynamic interactions affect diffusion at *intermediate and long time scales*. The effect of hydrodynamic interactions is quantified through comparisons to numerical studies of the corresponding dissipative systems [246].

4.4.2 On Transport Properties

Before describing the simulations or their results, we need to define and discuss two-dimensional transport properties. These are conveniently defined through so-called Green-Kubo relations.

The tracer diffusion coefficient D_{T} describes the motion of a tagged tracer particle. It is usually defined through $D_{\mathrm{T}} = \lim_{t\to\infty} D_{\mathrm{T}}(t)$, where

$$D_{\mathrm{T}}(t) = \frac{1}{dN} \sum_{i=1}^{N} \int_0^t \mathrm{d}t' \langle \mathbf{v}_i(t') \cdot \mathbf{v}_i(0) \rangle. \tag{4.14}$$

Here N is the number of particles and $\mathbf{v}_i(t)$ is the velocity of particle i at time t. This definition of D_{T} is equivalent to the so-called Einstein definition, see Eq. (2.12).

In practise D_{T} was not determined using Eq. (4.14) or the Einstein definition. Instead we used the computationally superior memory expansion technique [235]. In brief, a memory expansion for a transport coefficient consists of a sum of contributions, each describing memory effects in a given time interval. This technique thus allows one to monitor the decay of memory effects in time.

In *infinite two-dimensional systems with momentum-conservation* the asymptotic limit is not well defined; all transport coefficients should diverge as $t \to \infty$ [213, 215, 217, 249–253]. A solution to this problem is to treat the transport coefficients as time-dependent.

When tracer diffusion in colloidal suspensions is investigated experimentally, it is common to single out the effects of the hydrodynamic interactions by concentrating on the so-called short-time diffusion coefficients, see e.g.,

Refs. [237, 242, 243]. These are measured at times $\tau_B \ll t \ll \tau_I$ [248]. Here τ_B is a typical time scale for the relaxation of the velocity of a colloidal particle. This relaxation is induced by the solvent friction. The time scale τ_I is the structural relaxation time, the time it takes a colloidal particle to diffuse a distance comparable to its own size. In MD/SRD simulations the time interval between τ_B and τ_I tends to be narrow. Further, as the SRD solvent model has been developed for studies in the hydrodynamic regime, i.e., $t \gg \tau_I$, we should not expect it to give a very accurate description of the dynamics at time scales $t \approx \tau_B$. Computing short-time diffusion coefficients is therefore not going to solve our problems.

Instead, we consider transport coefficients measured at times $t > \tau_I$, i.e., intermediate- and long-time diffusion coefficients [248]. Despite a predicted divergence of the form $D_T(t) \sim \sqrt{\ln t}$, see, e.g., Ref. [252], our data show that tracer diffusion coefficients $D_T(\phi_c, t)$, measured at different colloidal area fractions ϕ_c, converge in the long time limit, see Ref. [226]. Although at intermediate time scales we observe that $D_T(\phi_c, t) \sim \sqrt{\ln t}$, in the limit $t \to \infty$ this tail is cut off by the *finite system size*, as it should [215,217]. The tail is also masked by statistical noise. Effective values $D_T(\phi_c)$ for the tracer diffusion coefficients can thus be extracted from the time regime where $D_T(\phi_c, t)$ appears to be constant. In the dilute limit, this plateau region yields the effective single-particle diffusion coefficient $D_0 \equiv D_T(\phi_c \to 0)$. Both $D_T(\phi_c)$ and D_0 depend on system size.

Scaled effective tracer diffusion coefficients are defined as $D_T(\phi_c)/D_0$. Since both $D_T(\phi_c)$ and D_0 should have similar—logarithmic—system size dependences, we expect that the scaled quantities do not depend on the system size. This indeed seems to be the case, see Ref. [226].

Having dealt with the tracer diffusion coefficient, we may define the other relevant transport coefficients in an analogous manner. The next transport coefficient to be discussed is the collective diffusion coefficient, which characterizes the decay rate of collective density fluctuations. It is usually defined as $D_C = \lim_{t\to\infty} D_C(t)$, where

$$D_C(t) = \xi D_{CM}(t) = \xi \frac{1}{dN} \int_0^t \mathrm{d}t' \langle \mathbf{J}(t') \cdot \mathbf{J}(0) \rangle. \tag{4.15}$$

The current flux $\mathbf{J}(t) = \sum_{i=1}^{N} \mathbf{v}_i(t)$ is proportional to the CM velocity of the N particles comprising the system, and therefore $D_{CM}(t)$ can be interpreted as the time-dependent CM diffusion coefficient of the N-particle system.

Scaled effective CM mobilities $D_{\mathrm{CM}}(\phi_{\mathrm{c}})/D_0$ have been determined in the spirit of scaled effective tracer diffusion coefficients $D_{\mathrm{T}}(\phi_{\mathrm{c}})/D_0$, see above. The prefactor $\xi = \langle N\rangle/[\langle N^2\rangle - \langle N\rangle^2]$ is the so-called thermodynamic factor, which is inversely proportional to the isothermal compressibility. It is a static quantity, and is not, within our numerical accuracy, affected by the presence of hydrodynamic interactions. We have determined ξ using both MD/SRD simulations and the so-called Boublik approximation [254]. These are in excellent agreement, see Fig. 4.5 and Ref. [246].

The third transport coefficient to be considered is the kinematic shear viscosity of the solvent $\eta/\rho_{\mathbf{b}}$. As mentioned in Sec. 4.3.2, this quantity can be interpreted as the diffusion coefficient of linear momentum. The numerical evaluation of the kinematic shear viscosity for the two-dimensional SRD solvent model with grid shifting is discussed in detail in Refs. [207, 208, 210, 212, 213]. As all the other transport coefficients in two dimensions, the kinematic shear viscosity is, in principle, a time-dependent quantity. Its long-time tails have been studied in Ref. [213].

The dimensionless ratio of the momentum and mass diffusivities of a fluid is called its Schmidt number Sc. For the solvent it is defined as

$$Sc \equiv \frac{\eta}{\rho_{\mathrm{b}} D_{\mathrm{b}}}, \tag{4.16}$$

where D_{b} is the tracer diffusion coefficient of the solvent particles. In two dimensions this definition must be effective in the same sense as the scaled effective tracer diffusion coefficient $D_{\mathrm{T}}(\phi_{\mathrm{c}})/D_0$.

When analytical arguments are formulated, it is often assumed that hydrodynamic fluctuations have reached a steady state at the time scale of the motion of the colloidal particles [253], i.e., $Sc \to \infty$. In real fluids hydrodynamic interactions do not act instantaneously, but nevertheless, $Sc \gg 1$. For instance for water $Sc \approx 10^3$. The situation can be quite different in mesoscopic simulations: because of the soft direct interactions, a DPD solvent typically has $Sc \approx 1$ [255]. In this case the hydrodynamic interactions are still developing at the time scales of colloidal diffusion; the dynamics of the colloids and the solvent velocity field are coupled. The consequences for the colloid dynamics are not fully understood [255].

Certain mesoscopic simulation techniques such as the Lowe-Andersen method [256] do allow for a wider range of Schmidt numbers. However, the numerical effort of updating the positions and velocities of all colloidal

and solvent particles can be enormous. Efficient techniques that could be used for modeling systems with hydrodynamic interactions under a variety of conditions, including dilute and concentrated solutions, and cases where Sc must be varied, are needed. The MD/SRD approach is a step in this direction.

4.4.3 Model System

We simulated an ensemble of disks immersed in a two-dimensional solvent. In the spirit of the MD/SRD model, the colloidal particles were described using MD and the solvent using SRD. The direct interactions between the colloidal particles were repulsive and short-ranged

$$V_{\mathrm{cc}}(r) = \begin{cases} \epsilon_{\mathrm{cc}} \left(\frac{\sigma_{\mathrm{cc}}}{r}\right)^n, & r \leq r_{\mathrm{c}} \equiv 2.5\sigma; \\ 0, & r > r_{\mathrm{c}}, \end{cases} \tag{4.17}$$

with $n = 12$, permitting a direct comparison with previous calculations without hydrodynamics [246]. In most simulations there were no direct colloid-solvent interactions, but the colloids participated in the multi-particle collisions, see Sec. 4.2. Whenever colloid-solvent interactions were included, they were of the form

$$V_{\mathrm{cb}}(r) = \begin{cases} \epsilon_{\mathrm{cb}} \left(\frac{\sigma_{\mathrm{cb}}}{r}\right)^n, & r \leq r_{\mathrm{c}}; \\ 0, & r > r_{\mathrm{c}}. \end{cases} \tag{4.18}$$

The colloid-colloid interaction parameters were set to $\sigma_{\mathrm{cc}} = 2\,\sigma$ and $\epsilon_{\mathrm{cc}} = \epsilon$, and the colloid-solvent ones to $\sigma_{\mathrm{cb}} = \sigma$ and $\epsilon_{\mathrm{cb}} = \epsilon$.

The masses of colloidal and solvent particles were chosen to be $m_{\mathrm{c}} = 5\,m$ and $m_{\mathrm{b}} = m$. As in Sec. 4.3.2, the parameters σ, ϵ, and m define our system of units, where the unit of time is defined as $\tau_{\mathrm{LJ}} \equiv \sigma\sqrt{m/\epsilon}$.

The temperature was set to $k_{\mathrm{B}}T = 2\,\epsilon$. Hamilton's equations of motion were integrated using the velocity Verlet algorithm with a time step $\delta t = 0.005\,\tau_{\mathrm{LJ}}$. Periodic boundary conditions were employed.

The dimensionless solvent density or solvent area fraction was chosen to be $\phi_{\mathrm{b}} = 1$. The colloidal and solvent area fractions are defined as $\phi_{\mathrm{c}} \equiv N_{\mathrm{c}}\,\sigma_{\mathrm{cc}}^2/A$ and $\phi_{\mathrm{b}} \equiv N_{\mathrm{b}}\,\sigma_{\mathrm{cb}}^2/A$. Here A is the total area of the system, N_{c} the number of colloidal particles, and N_{b} the number of solvent particles. With these definitions the colloidal area fraction of a closed-packed system is $\phi_{\mathrm{c}} \approx 1.15$.

Sc	$\eta/\rho_{\mathbf{b}}\,[\sigma^2\tau_{\mathrm{LJ}}^{-1}]$	$\tau\,[\tau_{\mathrm{LJ}}]$	$a\,[\sigma]$	α	$L\,[\sigma]$
1	0.82(1)	0.5	2	$\pm 90°$	200
100	9.11(2)	0.1	2	$\pm 170°$	100

Table 4.1. Summary of parameter sets used in colloid simulations. See the text for details.

The choice of the SRD parameters needs more thought than in the case of the two-dimensional polymer. In addition to attending to the usual constraints, we wanted to control the Schmidt number. This can be achieved by tuning the SRD parameters. We concentrated on two systems, one with $Sc \approx 1$ and another with $Sc \approx 100$. An additional system with $Sc \approx 20$ is discussed in Ref. [226]. The two different parameter sets corresponding to $Sc \approx 1$ and $Sc \approx 100$, as well as the resulting relevant solvent properties, are shown in Table 4.1.

The mesh size was set to $a = 2\,\sigma$ in both systems. As the solvent area fraction was $\phi_{\mathrm{b}} = 1$, there were on the average four solvent molecules in each cell, which is reasonably efficient. On the other hand, with the diameter of the colloidal particles set to $\sigma_{cc} = 2\,\sigma$, at most one colloidal particle was to be found in each cell. The collision step τ was assigned a value of either $0.5\,\tau_{LJ}$ or $0.1\,\tau_{LJ}$, implying that the system with $Sc \approx 100$ had a mean free path $\lambda \approx 0.1\,a$. To avoid unphysical correlations at short spatial and temporal scales, we employed the random grid shifting procedure, see Sec. 4.2. The rotation angles were such that either an angle $+\alpha$ or $-\alpha$ was chosen, each with probability 1/2. These choices together result in solvent shear viscosities that guarantee a valid description of the dynamics at length scales $\ell \gtrsim \sigma_{\mathrm{cc}}$.

4.4.4 Influence of Hydrodynamics on Tracer Diffusion

Figure 4.4 contains a summary of our results for the scaled effective tracer diffusion coefficient $D_{\mathrm{T}}(\phi_{\mathrm{c}})/D_0$ as a function of the area fraction ϕ_{c}. For comparison we also present data from purely dissipative systems of Brownian particles with short-ranged, repulsive interactions [246]. These data have been manipulated such that they correspond to the interaction potential and temperature used in the MD/SRD simulations, see Refs. [226, 246] for details.

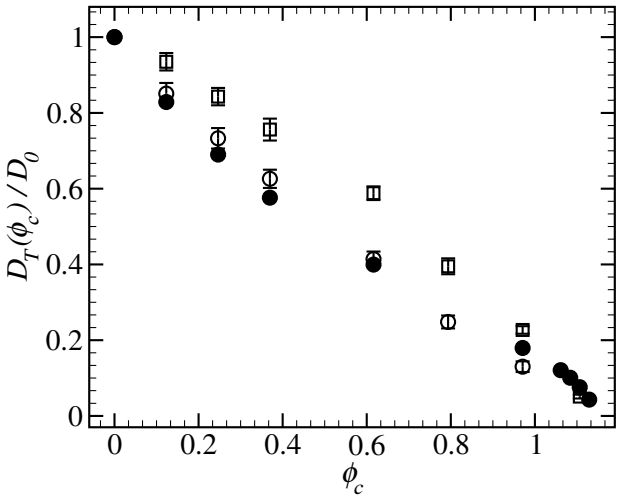

Figure 4.4. Scaled effective tracer diffusion coefficients as functions of colloidal area fraction for $Sc \approx 1$ (○) and $Sc \approx 100$ (□) [226]. Results from simulations without hydrodynamic interactions [246] are also shown (●).

The scaled effective tracer diffusion coefficients decrease monotonously with an increasing colloidal area fraction; tracer diffusion is considerably slower in the concentrated regime than in the dilute limit. This is the case regardless of the Schmidt number or the presence of hydrodynamic interactions, and the reduction must therefore originate in the direct interactions.

The effect of the hydrodynamics on long-time tracer diffusion can be singled out by comparing the results generated using MD/SRD to the ones from the purely dissipative Brownian dynamics (BD) simulations. At low values of Sc, hydrodynamics has virtually no effect on tracer diffusion. When Sc is increased to approximately 100, we observe a minor enhancement in $D_T(\phi_c)/D_0$. The enhancement is largest at intermediate area fractions, i.e., $\phi_c \approx 0.4 - 0.7$.

How do these findings compare with experimental and other simulation studies? Experimental studies [237, 241–244] are always quasi-two-dimensional, and the interactions between the colloidal particles, in most cases polystyrene spheres, can be tuned such that they are either short- or long-ranged. The simulation studies [238–241] aim at closely mimicking the experiments, and hence are, too, quasi-two-dimensional. Our simulations have been conducted in a very generic, ideal two-dimensional system. Although comparison of such systems with quasi-two-dimensional ones

should be meaningful [252], we should be mindful that there exist subtle differences between different kinds of confined systems, e.g., in the decay of the velocity fluctuations [257, 258].

In experimental studies, hydrodynamic interactions just cannot be "turned off"; comparison between two otherwise similar systems, but with and without hydrodynamics is not possible. Experimentalists, and some simulators, too, believe that at high dilution and short time scales, hydrodynamic interactions between colloidal particles alone explain deviations from the diffusion coefficient at infinite dilution [237, 241–244]. The larger the area fraction of colloidal particles, the more important the role played by the hydrodynamic interactions. Hence, if the short-time tracer diffusion coefficient decreases with an increasing area fraction, hydrodynamic interactions are said to suppress tracer diffusion. This appears to be the case for colloidal particles with short-range interactions [237, 242, 243]. Analogously, an increase in the short-time tracer diffusion coefficient with an increasing area fraction is interpreted as enhancement by hydrodynamic interactions. This applies for colloidal particles with long-range interactions [241, 244].

To our knowledge, there exists only one set of simulations where the same systems with and without hydrodynamic interactions between colloidal particles have actually been compared: the Stokesian dynamics simulations by Pesché et al. [238]. In accordance with Refs. [237, 242, 243], the short-time tracer diffusion coefficient for colloidal particles with hard-sphere interactions was found to decrease with an increasing area fraction. What is more interesting, at intermediate and long time scales, hydrodynamic interactions seemed to suppress tracer diffusion of particles with hard-sphere interactions. This was the case for moderately charged particles interacting with Yukawa-like potentials, as well. With stronger charges, intermediate- and long-time tracer diffusion was very slightly enhanced. The intermediate- and long-time results in Ref. [238] are all for low area fractions $\phi_c \lesssim 0.05$.

We find that for colloidal particles with short-range interactions of the form $V(r) \sim 1/r^{12}$, hydrodynamics might have a slight enhancing effect on intermediate- and long-time tracer diffusion. In our opinion, the low Schmidt number result, i.e., essentially no significant effect, may be more reliable than the slight enhancement from simulations with $Sc \approx 100$. The reason is that in our experience, with MD/SRD, finite size artifacts seem to be more severe in systems with $Sc \gg 1$. On the other hand, as explained in Sec. 4.4.2, $Sc \approx 1$ may have unforeseen consequences for the solute dynamics. As for comparison to Refs. [237, 241–244], we are not completely

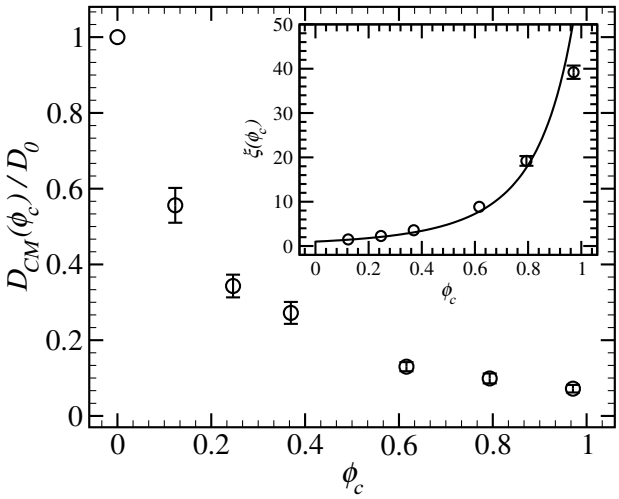

Figure 4.5. Scaled effective CM mobility as function of colloidal area fraction for $Sc \approx 1$ [226]. The inset shows the thermodynamic factor ξ from our MD/SRD simulations (○) and the Boublik approximation [254] (solid line).

convinced that the influence of direct interactions can be ruled out at short time scales, especially as the area fraction increases. Pesché et al. [238] do not make such assumptions, but their intermediate- and long-time results are for rather dilute systems.

We conclude that more research into tracer diffusion in confined geometries is needed. Two issues are of special interest. First, it would be interesting to compare tracer diffusion in bulk three-dimensional, quasi-two-dimensional, and ideal two-dimensional systems. This could be realized by starting from a three-dimensional system and systematically reducing the linear size in the, say, z direction. There are, however, certain fairly severe technical problems with conducting MD/SRD simulations in a quasi-two-dimensional geometry. Another line of inquiry would be to systematically alter the form of the direct interactions between colloidal particles.

4.4.5 Hydrodynamics and Collective Diffusion Coefficient

The collective diffusion coefficient, as explained in Sec. 4.4.2, is a product of the thermodynamic factor ξ and the CM diffusion coefficient of the

system of colloidal particles. In the case of dissipative hard spheres on a smooth surface, the CM mobility is independent of the area fraction [259]: $D_{\mathrm{CM}}(\phi_{\mathrm{c}}) = D_{\mathrm{CM}}(0) = \text{const}$. With hydrodynamic interactions in place, this no longer holds true. As Fig. 4.5 shows, in our MD/SRD simulations the scaled effective CM mobility *decreases* monotonously with ϕ_{c}. The decrease is more rapid than that of $D_{\mathrm{T}}(\phi_{\mathrm{c}})/D_0$, see Fig. 4.4. Unlike $D_{\mathrm{T}}(\phi_{\mathrm{c}})/D_0$, the scaled effective CM mobility does not appear to depend on the value of the Schmidt number.

The thermodynamic factor is shown in the inset of Fig. 4.5. It is a monotonously *increasing* function of ϕ_{c}. In the dissipative system with a constant $D_{\mathrm{CM}}(\phi_{\mathrm{c}})/D_0$, the thermodynamic factor alone dictates the behavior of the scaled effective collective diffusion coefficient, see Fig. 4.6. With a decreasing $D_{\mathrm{CM}}(\phi_{\mathrm{c}})/D_0$, we may expect to see an interesting interplay of the thermodynamic factor and the CM mobility.

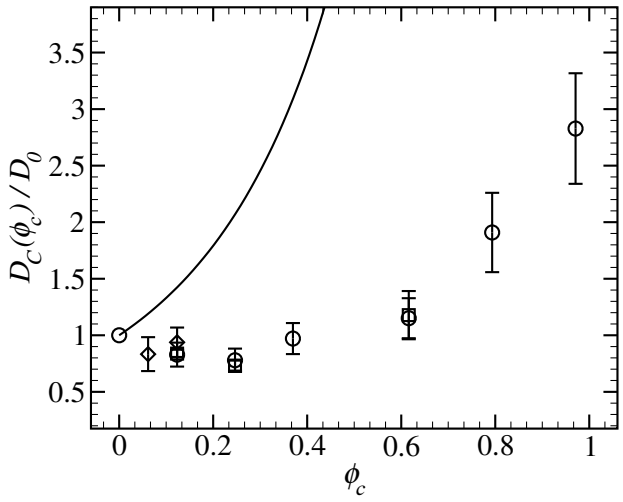

Figure 4.6. Scaled effective collective diffusion coefficients as functions of colloidal area fraction: $Sc \approx 1$ from simulations without direct colloid-solvent interactions ($\circ$), $Sc \approx 1$ with direct colloid-solvent interactions ($\diamond$), and $Sc \approx 100$ without direct colloid-solvent interactions ($\square$) [226]. Scaled effective collective diffusion coefficients from simulations without hydrodynamic interactions [246] are shown for reference (solid lines).

The scaled effective collective diffusion coefficient from MD/SRD simulations is depicted in Fig. 4.6. The intriguing interplay is indeed there: $D_{\mathrm{C}}(\phi_{\mathrm{c}})/D_0$ displays a slight *minimum* at low area fractions. Although ξ increases monotonously, below $\phi_{\mathrm{c}} \approx 0.2 - 0.3$ the initial decay of

$D_{\mathrm{CM}}(\phi_{\mathrm{c}})/D_0$ dictates the shape of the scaled effective collective diffusion coefficient. At these low area fractions, the scaled tracer and collective diffusion coefficients are essentially identical. This is expected, since in the dilute limit $D_{\mathrm{C}} \approx D_{\mathrm{T}}$. Above $\phi_{\mathrm{c}} \approx 0.2 - 0.3$, the behavior of $D_{\mathrm{C}}(\phi_{\mathrm{c}})/D_0$ is dominated by the diverging thermodynamic factor.

Most of the data we have presented are from simulations where the direct colloid-solvent interactions have been replaced by multi-particle collisions, see Sec. 4.2. We have ascertained that the minimum seen in $D_{\mathrm{C}}(\phi_{\mathrm{c}})/D_0$ vs. ϕ_{c} is no artifact originating from the omission of the direct colloid-solvent interactions. Scaled effective collective diffusion coefficients for $\phi_{\mathrm{c}} \leq 0.2$ from MD/SRD simulations with direct colloid-solvent interactions are shown in Fig. 4.4. Within our numerical accuracy, both schemes yield identical values for $D_{\mathrm{C}}(\phi_{\mathrm{c}})/D_0$. Consequently, in both cases a minimum close to $\phi_{\mathrm{c}} \approx 0.2 - 0.3$ is observed. For a more extensive discussion on the consequences of including vs. excluding the direct colloid-solvent interactions, see Ref. [226].

Concluding, the presence of hydrodynamic interactions appears to have a striking effect on collective diffusion. The value of the Schmidt number, on the other hand, does not have any influence on the value of the scaled effective collective diffusion coefficient. Our simulations suggest that the phenomenon observed here—the competition between the CM mobility and the thermodynamic factor—could be generic in colloidal suspensions and might also be observed in experiments. The actual form of $D_{\mathrm{C}}(\phi_{\mathrm{c}})/D_0$ may vary from one system to another, depending, e.g., on the detailed form of the direct interactions. Recent mode coupling calculations seem to support this idea [260]. Nevertheless, further studies and experiments in particular are needed.

5

Conclusions

The theme of this Thesis was computer simulation of biological and soft matter at different spatial and temporal scales. Modeling at different scales was illustrated through examples or case studies. Each case study was complemented by a brief introduction to the relevant simulation algorithms, as well as an overview of the most recent progress in related studies and model development.

The first set of case studies was into classical atomic-scale MD simulations of lipid membrane systems. Here we focused on the effect of cholesterol on phospholipid bilayers, especially on their free volume, packing, and diffusive properties. The complementary material consisted of an introduction to classical atomic-scale models of biological matter, a description of the principles of MD simulations, and a summary of the latest literature on computational modeling of membrane systems.

The topic of the second case study was coarse-graining of models of soft condensed matter, with an aim to reach larger system sizes. More specifically, we coarse-grained the atomic-scale phospholipid/cholesterol systems from the previous case studies, subsequently using the coarse-grained models to study the lateral structure of bilayers at mesoscale, in our case at length scales up to hundreds of nanometers. The background material included a sketch of the motivation and strategies of coarse-graining, a review of coarse-grained membrane models in the literature, as well as a description of a novel approach to systematic coarse-graining: inverse Monte Carlo.

The third set of studies illustrated the use of important, emerging tools in computer modeling: hybrid models that combine two or several descriptions at different resolutions. Another leitmotiv here was coarse-grained modeling of hydrodynamic interactions. We presented two systems, a polymer

chain in solution and a colloidal suspension. Both were modeled using MD/SRD, a novel hybrid approach that combines an MD description for the solute with a coarse-grained solvent model called stochastic rotation dynamics (SRD). In addition to the case studies, we introduced the SRD and MD/SRD techniques, and presented a literature review of the development and application of these very novel techniques.

At the end of each set of case studies, we mentioned possible ideas for future research. There are many interesting directions to take, but the most intriguing ones are perhaps the following. In the field of atomic-scale MD modeling, a promising project for the near future would be to look at the microscopic diffusion processes of phospholipid and cholesterol molecules, and to perhaps investigate the role of voids in these processes. The systematic coarse-graining methodology should be used for studies of phospholipid/sphingomyelin/cholesterol bilayers, as well as for membrane systems with proteins. Different degrees of coarse-graining should also be attempted. Finally, an ambitious project, which is more long-term, would be the development of novel hybrid models to be used in, e.g., membrane simulations.

Bibliography

[1] M. Patra, M. Karttunen, M. T. Hyvönen, E. Falck, P. Lindqvist, and I. Vattulainen, Biophys. J. **84**, 3636 (2003).

[2] M. Patra, M. Karttunen, M. T. Hyvönen, E. Falck, and I. Vattulainen, J. Phys. Chem. B **108**, 4485 (2004).

[3] M. Patra, M. Karttunen, M. T. Hyvönen, E. Falck, and I. Vattulainen, Long-Range Interactions in Molecular Simulations: Accuracy and Speed, 2005, submitted to J. Chem. Phys., pre-print cond-mat/0410210.

[4] O. Punkkinen, E. Falck, I. Vattulainen, and T. Ala-Nissila, Dynamics and Scaling in Polymers in a Dilute Solution: Analytical Treatment in Two and Higher Dimensions, 2005, to appear in J. Chem. Phys.

[5] B. Alberts, D. Bray, J. Lewis, M. Raff, K. Roberts, and J. D. Watson, *Molecular Biology of the Cell*, 3rd ed. (Garland Publishing, New York, 1994).

[6] R. F. M. de Almeida, A. Fedorov, and M. Prieto, Biophys. J. **85**, 2406 (2003).

[7] M. Edidin, Annu. Rev. Biophys. Biomol. Struct. **32**, 257 (2003).

[8] S. Mayor and M. Rao, Traffic **5**, 231 (2004).

[9] K. Simons and E. Ikonen, Nature **387**, 569 (1997).

[10] I. Vattulainen and O. G. Mouritsen, in *Diffusion in Condensed Matter*, 2nd ed., edited by D. Hejtans and J. Karger (Springer-Verlag, Berlin, 2004).

[11] S. König, W. Pfeiffer, T. Bayerl, D. Richter, and E. Sackmann, J. Phys. II France **2**, 1589 (1992).

[12] S. König and E. Sackmann, Curr. Opin. Colloid Interface Sci. **1**, 78 (1996).

[13] J. Korlach, P. Schwille, W. W. Webb, and G. W. Feigenson, Proc. Natl. Acad. Sci. USA **96**, 8461 (1999).

[14] D. Axelrod, D. E. Koppel, J. Schlessinger, E. Elson, and W. W. Webb, Biophys. J. **16**, 1055 (1976).

[15] D. M. Soumpasis, Biophys. J. **41**, 95 (1983).

[16] M. P. Allen and D. J. Tildesley, *Computer Simulation of Liquids* (Oxford University Press, New York, 1990).

[17] D. Frenkel and B. Smit, *Understanding Molecular Simulation: From Algorithms to Applications*, 2nd ed. (Academic Press, San Diego, 2002).

[18] T. Schlick, *Molecular Modeling and Simulation* (Springer, New York, 2002).

[19] M. Doi and S. F. Edwards, *The Theory of Polymer Dynamics* (Clarendon Press, Oxford, 1986).

[20] A. P. Lyubartsev and A. Laaksonen, Phys. Rev. E **52**, 3730 (1995).

[21] A. Malevanets and R. Kapral, J. Chem. Phys. **110**, 8605 (1999).

[22] A. Malevanets and R. Kapral, J. Chem. Phys. **112**, 7260 (2000).

[23] J.-G. Lee, C. Sagui, and C. Roland, J. Am. Chem. Soc. **126**, 8384 (2004).

[24] P. Carloni, U. Rothlisberger, and M. Parrinello, Acc. Chem. Res. **35**, 455 (2002).

[25] W. Andreoni, A. Curioni, and T. Mordasini, IBM J. Res. Develop. **45**, 397 (2001).

[26] D. Chivian, T. Robertson, R. Bonneau, and D. Baker, Methods Biochem. Anal. **44**, 547 (2003).

[27] M. Colombo, L. Guidoni, A. Laio, A. Magistrato, P. Maurer, S. Piana, U. Röhrig, K. Spiegel, M. Sulpizi, J. VandeVondele, M. Zumstein, and U. Rothlisberger, CHIMIA **56**, 13 (2002).

[28] D. van der Spoel, E. Lindahl, B. Hess, A. R. van Buuren, E. Apol, P.-J. Meulenhoff, D. P. Tielemann, A. L. T. M. Sijbers, K. A. Feenstra, R. van Drunen, and H. J. C. Berendsen, *Gromacs User Manual version 3.2*, www.gromacs.org, 2004.

[29] G. D. Smith and W. Paul, J. Phys. Chem. A **102**, 1200 (1998).

[30] D. P. Tieleman, S. J. Marrink, and H. J. C. Berendsen, Biochim. Biophys. Acta **1331**, 235 (1997).

[31] I. Vattulainen and M. Karttunen, in *Computational Nanotechnology*, edited by M. Rieth and W. Schommers (American Scientific Publishers, USA, 2005), in press.

[32] A. L. Fetter and J. D. Walecka, *Theoretical Mechanics of Particles and Continua* (Dover Publications, New York, 2003).

[33] H. J. C. Berendsen, J. P. M. Postma, W. F. van Gunsteren, A. DiNola, and J. R. Haak, J. Chem. Phys. **81**, 3684 (1984).

[34] W. G. Hoover, Phys. Rev. A **31**, 1695 (1985).

[35] S. Nosé, Mol. Phys. **52**, 255 (1984).

[36] S. Nosé and M. L. Klein, Mol. Phys. **50**, 1055 (1983).

[37] M. Parrinello and A. Rahman, J. Appl. Phys. **52**, 7182 (1981).

[38] U. Essmann, L. Perera, M. L. Berkowitz, H. L. T. Darden, and L. G. Pedersen, J. Chem. Phys. **103**, 8577 (1995).

[39] B. Hess, H. Bekker, H. J. C. Berendsen, and J. G. E. M. Fraaije, J. Comput. Chem. **18**, 1463 (1997).

[40] E. Egberts, S.-J. Marrink, and H. J. C. Berendsen, Eur. Biophys. J. **22**, 423 (1994).

[41] L. R. Forrest and M. S. P. Sansom, Curr. Opin. Struct. Biol. **10**, 174 (2000).

[42] S. E. Feller, Curr. Opin. Colloid Interface Sci. **5**, 217 (2000).

[43] H. L. Scott, Curr. Opin. Struct. Biol. **12**, 495 (2002).

[44] L. Saiz and M. L. Klein, Bioscience Rep. **22**, 151 (2002).

[45] L. Saiz and M. L. Klein, Acc. Chem. Res. **35**, 482 (2002).

[46] R. B. Gennis, *Biomembranes: Molecular Structure and Function* (Springer-Verlag, New York, 1989).

[47] S. W. Chiu, E. Jakobsson, R. J. Mashl, and H. L. Scott, Biophys. J. **83**, 1842 (2002).

[48] E. Falck, M. Patra, M. Karttunen, M. T. Hyvönen, and I. Vattulainen, Biophys. J. **87**, 1076 (2004).

[49] C. Hofsäß, E. Lindahl, and O. Edholm, Biophys. J. **84**, 2192 (2003).

[50] S. A. Pandit, D. Bostick, and M. L. Berkowitz, Biophys. J. **86**, 1345 (2004).

[51] A. M. Smondyrev and M. L. Berkowitz, Biophys. J. **80**, 1649 (2001).

[52] S. W. Chiu, S. Vasudevan, E. Jakobsson, R. J. Mashl, and H. L. Scott, Biophys. J. **85**, 3624 (2003).

[53] E. Mombelli, R. Morris, W. Taylor, and F. Fraternali, Biophys. J. **84**, 1507 (2004).

[54] P. Niemelä, M. T. Hyvönen, and I. Vattulainen, Biophys. J. **87**, 2976 (2004).

[55] S. A. Pandit, S. Vasudevan, S. W. Chiu, R. J. Mashl, E. Jakobsson, and H. L. Scott, Biophys. J. **87**, 1092 (2004).

[56] S. A. Pandit, E. Jakobsson, and H. L. Scott, Biophys. J. **87**, 3312 (2004).

[57] J. R. Silvius, Biochim. Biophys. Acta **1610**, 174 (2003).

[58] R. S. Cantor, Biophys. J. **76**, 2625 (1999).

[59] R. G. Eckenhoff, Mol. Interv. **1**, 258 (2001).

[60] M. Pasenkiewicz-Gierula, T. Ròg, J. Grochowski, P. Serda, R. Czarnecki, T. Librowski, and S. Lochynski, Biophys. J. **85**, 1248 (2003).

[61] L. Koubi, L. Saiz, M. Tarek, D. Scharf, and M. L. Klein, J. Phys. Chem. B **107**, 14500 (2003).

[62] M. Patra, E. Salonen, E. Terama, I. Vattulainen, R. Faller, B. W. Lee, J. Holopainen, and M. Karttunen, Under the Influence of Alcohol: The Effect of Ethanol and Methanol on Lipid Bilayers, 2004, submitted to Biophys. J., pre-print cond-mat/0408122.

[63] C. S. Pereira, R. D. Lins, I. Chandrasekhar, L. C. G. Freitas, and P. H. Hünenberger, Biophys. J. **86**, 2273 (2004).

[64] A. K. Sum and J. J. de Pablo, Biophys. J. **85**, 2830 (2003).

[65] P. Mukhopadhyay, H. J. Vogel, and D. P. Tieleman, Biophys. J. **86**, 337 (2004).

[66] J. Repáková, P. Čapková, J. M. Holopainen, and I. Vattulainen, J. Phys. Chem. B **108**, 13438 (2004).

[67] B. W. Lee, R. Faller, A. K. Sum, I. Vattulainen, M. Patra, and M. Karttunen, Fluid Phase Eq. **225**, 63 (2004).

[68] W. L. Ash, M. R. Zlomislic, E. O. Oloo, and D. P. Tieleman, Biochim. Biophys. Acta **1666**, 158 (2004).

[69] R. A. Böckmann, A. Hac, T. Heimburg, and H. Grubmüller, Biophys. J. **85**, 1647 (2003).

[70] R. A. Böckmann and H. Grubmüller, Angew. Chemie Int. Ed. **43**, 1021 (2004).

[71] S. A. Pandit, D. Bostick, and M. L. Berkowitz, Biophys. J. **84**, 3743 (2003).

[72] J. N. Sachs, H. Nanda, H. I. Petrache, and T. B. Woolf, Biophys. J. **86**, 3772 (2004).

[73] S. A. Pandit and M. L. Berkowitz, Biophys. J. **82**, 1818 (2002).

[74] P. Mukhopadhyay, L. Monticelli, and D. P. Tieleman, Biophys. J. **86**, 1601 (2004).

[75] S. A. Pandit, D. Bostick, and M. L. Berkowitz, Biophys. J. **85**, 3120 (2003).

[76] S. Bandyopadhyay, M. Tarek, and M. L. Klein, J. Phys. Chem. B **103**, 10075 (1999).

[77] A. A. Gurtovenko, M. Patra, M. Karttunen, and I. Vattulainen, Biophys. J. **86**, 3461 (2004).

[78] B. Ilan, E. Tajkhorshid, K. Schulten, and G. A. Voth, Proteins: Struct. Funct. Bioinf. **55**, 223 (2004).

[79] M. Sotomayor and K. Schulten, Biophys. J. **87**, 3050 (2004).

[80] B. Roux and K. Schulten, Structure **12**, 1343 (2004).

[81] S.-J. Marrink and H. J. C. Berendsen, J. Phys. Chem. **98**, 4155 (1994).

[82] S.-J. Marrink and H. J. C. Berendsen, J. Phys. Chem. **100**, 16729 (1996).

[83] D. Bemporad, C. Luttmann, and J. W. Essex, Biophys. J. **108**, 4875 (2004).

[84] D. Bemporad, C. Luttmann, and J. W. Essex, Biophys. J. **87**, 1 (2004).

[85] J. Ulander and A. D. J. Haymet, Biophys. J. **85**, 3475 (2003).

[86] W. Shinoda, M. Mikami, T. Baba, and M. Hato, J. Phys. Chem. B **108**, 9346 (2004).

[87] W. Shinoda, M. Mikami, T. Baba, and M. Hato, J. Phys. Chem. B **107**, 14030 (2003).

[88] M. Bachar, P. Brunelle, D. P. Tieleman, and A. Rauk, J. Phys. Chem. B **108**, 7170 (2004).

[89] N. V. Eldho, S. E. Feller, S. Tristram-Nagle, I. V. Polozov, and K. Gawrisch, J. Am. Chem. Soc. **125**, 6409 (2003).

[90] S. E. Feller, K. Gawrisch, and A. D. MacKerell, Jr., J. Am. Chem. Soc. **124**, 318 (2002).

[91] A. H. de Vries, A. E. Mark, and S.-J. Marrink, J. Phys. Chem. B **108**, 2454 (2004).

[92] H. Leontiadou, A. E. Mark, and S.-J. Marrink, Biophys. J. **86**, 2156 (2004).

[93] F. Y. Jiang, Y. Bouret, and J. T. Kindt, Biophys. J. **87**, 182 (2004).

[94] P. M. Kasson and V. S. Pande, Biophys. J. **86**, 3744 (2004).

[95] K. Åman, E. Lindahl, O. Edholm, P. Håkansson, and P.-O. Westlund, Biophys. J. **84**, 102 (2004).

[96] C. F. Lopez, S. O. Nielsen, and M. L. Klein, J. Phys. Chem. B **108**, 6603 (2004).

[97] E. Tüchsen, M. Ø. Jensen, and P. Westh, Chem. Phys. Lipids **123**, 107 (2003).

[98] A. H. de Vries, A. E. Mark, and S.-J. Marrink, J. Am. Chem. Soc. **126**, 4488 (2004).

[99] D. P. W. McMullen and R. N. McElhaney, Curr. Opin. Colloid Interface Sci. **1**, 83 (1996).

[100] H. Ohvo-Rekilä, B. Ramstedt, P. Leppimäki, and J. P. Slotte, Prog. Lipid Res. **41**, 66 (2002).

[101] M. B. Sankaram and T. E. Thompson, Biochemistry **29**, 10670 (1990).

[102] M. B. Sankaram and T. E. Thompson, Biochemistry **29**, 10676 (1990).

[103] M. R. Vist and J. H. Davis, Biochemistry **29**, 451 (1990).

[104] M. B. Sankaram and T. E. Thompson, Proc. Natl. Acad. Sci. USA **88**, 8686 (1991).

[105] H. I. Petrache, K. Tu, and J. F. Nagle, Biophys. J. **76**, 2479 (1999).

[106] S. Bhattacharya and S. Haldar, Biochim. Biophys. Acta **1467**, 39 (2000).

[107] A. Carruthers and D. L. Melchior, Biochemistry **22**, 5797 (1983).

[108] P. Jedlovszky and M. Mezei, J. Phys. Chem. B **107**, 5322 (2003).

[109] W. K. Subczynski, A. Wisniewska, J.-J. Yin, J. S. Hyde, and A. Kusumi, Biochemistry **33**, 7670 (1994).

[110] T.-X. Xiang, J. Phys. Chem. B **103**, 385 (1999).

[111] P. F. F. Almeida, W. L. C. Vaz, and T. E. Thompson, Biochemistry **31**, 6739 (1992).

[112] H.-J. Galla, W. Hartmann, U. Theilen, and E. Sackmann, J. Membrane Biol. **48**, 215 (1979).

[113] J. M. Polson, I. Vattulainen, H. Zhu, and M. J. Zuckermann, Eur. Phys. J. E **5**, 485 (2001).

[114] D. Bassolino-Klimas, H. E. Alper, and T. R. Stouch, J. Am. Chem. Soc. **117**, 4118 (1995).

[115] A. Bondi, J. Phys. Chem. **58**, 929 (1954).

[116] S.-J. Marrink, R. M. Sok, and H. J. C. Berendsen, J. Chem. Phys. **104**, 9090 (1996).

[117] K. Rajagopal and V. Sitaramam, J. Theor. Biol. **195**, 245 (1998).

[118] M. H. Cohen and D. Turnbull, J. Chem. Phys. **31**, 1164 (1959).

[119] E. Falck, M. Patra, M. Karttunen, M. T. Hyvönen, and I. Vattulainen, J. Chem. Phys. **121**, 12676 (2004).

[120] M. Pasenkiewicz-Gierula, T. Róg, K. Kitamura, and A. Kusumi, Biophys. J. **78**, 1376 (2000).

[121] T. Róg and M. Pasenkiewicz-Gierula, Biophys. J. **81**, 2190 (2001).

[122] A. M. Smondyrev and M. L. Berkowitz, Biophys. J. **77**, 2075 (1999).

[123] K. Tu, M. L. Klein, and D. J. Tobias, Biophys. J. **75**, 2147 (1998).

[124] O. Berger, O. Edholm, and F. Jahnig, Biophys. J. **72**, 2002 (1997).

[125] M. Höltje, T. Förster, B. Brandt, T. Engels, W. von Rybinski, and H.-D. Höltje, Biophys. Biochim. Acta **1511**, 156 (2001).

[126] D. P. Tieleman and H. J. C. Berendsen, J. Chem. Phys. **105**, 4871 (1996).

[127] H. J. C. Berendsen, J. P. M. Postma, W. F. van Gunsteren, and J. Hermans, in *Intermolecular Forces*, edited by B. Pullman (Reidel, Dordrecht, 1981), pp. 331–342.

[128] E. Lindahl, B. Hess, and D. van der Spoel, J. Mol. Model. **7**, 306 (2001).

[129] U. Essman, L. Perera, M. L. Berkowitz, H. L. T. Darden, and L. G. Pedersen, J. Chem. Phys. **103**, 8577 (1995).

[130] P. B. Macedo and T. A. Litovitz, J. Chem. Phys. **42**, 245 (1965).

[131] D. Turnbull and M. H. Cohen, J. Chem. Phys. **34**, 120 (1961).

[132] D. Turnbull and M. H. Cohen, J. Chem. Phys. **52**, 3038 (1970).

[133] J. E. MacCarthy and J. K. Kozak, J. Chem. Phys. **77**, 2214 (1982).

[134] W. L. C. Vaz, R. M. Clegg, and D. Hallmann, Biochemistry **24**, 781 (1985).

[135] A. Filippov, G. Orädd, and G. Lindblom, Biophys. J. **84**, 3079 (2003).

[136] R. van Gastel, E. Somfai, W. van Saarloos, and J. W. M. Frenken, Nature **408**, 665 (2000).

[137] R. van Gastel, E. Somfai, S. B. van Albada, W. van Saarloos, and J. W. M. Frenken, Phys. Rev. Lett. **86**, 1562 (2001).

[138] F. Montalenti and R. Ferrando, Phys. Rev. Lett. **82**, 1498 (1999).

[139] C. Donati, J. F. Douglas, W. KOb, S. J. Plimpton, P. H. Poole, and S. C. Glotzer, Phys. Rev. Lett. **80**, 2338 (1998).

[140] T. R. Stouch and D. Bassolino, in *Biological Membranes: A Molecular Perspective from Computation and Experiment*, edited by K. M. Merz, Jr. and B. Roux (Birkhäuser, Boston, 1996), pp. 255–280.

[141] J. C. Mathai, Z. E. Sauna, O. John, and V. Sitaramam, J. Biol. Chem. **268**, 15442 (1993).

[142] D. Bassolino-Klimas, H. E. Alper, and T. R. Stouch, Biochemistry **32**, 12624 (1993).

[143] M. E. J. Newman and R. M. Ziff, Phys. Rev. E **64**, 016706 (2001).

[144] S. Sharma, *Applied Multivariate Techniques* (Wiley, New York, 1996).

[145] S. Stauffer and A. Aharony, *Introduction to Percolation Theory*, 2nd ed. (Taylor and Francis, London, 1992).

[146] R. Faller, Polymer **45**, 3869 (2004).

[147] L. Miao, M. Nielsen, J. Thewalt, J. H. Ipsen, M. Bloom, M. J. Zuckermann, and O. G. Mouritsen, Biophys. J. **82**, 1429 (2002).

[148] M. Nielsen, L. Miao, J. H. Ipsen, O. G. Mouritsen, and M. J. Zuckermann, Phys. Rev. E **54**, 6889 (1996).

[149] M. Nielsen, L. Miao, J. H. Ipsen, M. J. Zuckermann, and O. G. Mouritsen, Phys. Rev. E **59**, 5790 (1999).

[150] P. Høyrup, K. Jørgens, and O. G. Mouritsen, Comput. Phys. Commun. **147**, 313 (2002).

[151] J. Huang and G. W. Feigenson, Biophys. J. **76**, 2142 (1999).

[152] J. Huang, Biophys. J. **83**, 1014 (2002).

[153] B. Cannon, G. Heath, J. Hyang, P. Somerharju, J. A. Virtanen, and K. H. Cheng, Biophys. J. **84**, 3777 (2003).

[154] P. Somerharju, J. A. Virtanen, and K. H. Cheng, Biochim. Biophys. Acta **1440**, 32 (1999).

[155] J. A. Virtanen, K. H. Cheng, and P. Somerharju, Proc. Natl. Acad. Sci. USA **95**, 4964 (1998).

[156] J. A. Virtanen and P. Somerharju, J. Phys. Chem. B **103**, 10289 (1999).

[157] P. Sengupta, R. R. P. Singh, D. L. Cox, and A. Slepoy, Phys. Rev. E **70**, 021902 (2004).

[158] C. Loison, M. Mareschal, K. Kremer, and F. Schmid, J. Chem. Phys. **119**, 13138 (2003).

[159] C. Loison, M. Mareschal, and F. Schmid, J. Chem. Phys. **121**, 1890 (2004).

[160] R. Goetz and R. Lipowsky, J. Chem. Phys. **108**, 7397 (1998).

[161] R. Goetz, G. Gompper, and R. Lipowsky, Phys. Rev. Lett. **82**, 221 (1999).

[162] A. Imparato, J. C. Shillcock, and R. Lipowsky, Eur. Phys. J. E **11**, 21 (2003).

[163] J. C. Shillcock and R. Lipowsky, J. Chem. Phys. **117**, 5048 (2002).

[164] P. Español and P. Warren, Europhys. Lett. **30**, 191 (1995).

[165] R. D. Groot and P. B. Warren, J. Chem. Phys. **107**, 4423 (1997).

[166] P. J. Hoogerbrugge and J. M. V. A. Koelman, Europhys. Lett. **19**, 155 (1992).

[167] M. J. Stevens, J. H. Hoh, and T. B. Woolf, Phys. Rev. Lett. **91**, 188102 (2004).

[168] M. J. Stevens, J. Chem. Phys. **121**, 11942 (2004).

[169] R. D. Groot and K. L. Rabone, Biophys. J. **81**, 725 (2001).

[170] M. Kranenburg, M. Venturoli, and B. Smit, Phys. Rev. E **67**, 060901(R) (2003).

[171] M. Kranenburg, M. Venturoli, and B. Smit, J. Phys. Chem. B **107**, 11491 (2003).

[172] M. Kranenburg, M. Vlaar, and B. Smit, Biophys. J. **87**, 1596 (2004).

[173] R. D. Groot and T. J. Madden, J. Chem. Phys. **108**, 8713 (1998).

[174] S. O. Nielsen, C. F. Lopez, P. B. Moore, J. C. Shelley, and M. L. Klein, J. Phys. Chem. B **107**, 13911 (2003).

[175] J. C. Shelley, M. Y. Shelley, R. C. Reeder, S. Bandyopadhyay, and M. L. Klein, J. Phys. Chem. B **105**, 4464 (2001).

[176] J. C. Shelley, M. Y. Shelley, R. C. Reeder, S. Bandyopadhyay, P. B. Moore, and M. L. Klein, J. Phys. Chem. B **105**, 9785 (2001).

[177] C. F. Lopez, S. O. Nielsen, P. B. Moore, and M. L. Klein, Proc. Natl. Acad. Sci. USA **101**, 4431 (2004).

[178] S. J. Marrink, A. H. de Vries, and A. E. Mark, J. Phys. Chem. B **108**, 750 (2004).

[179] G. Ayton, S. G. Bardenhagen, P. McMurtry, D. Sulsky, and G. A. Voth, J. Chem. Phys. **114**, 6913 (2001).

[180] G. Ayton, A. M. Smondyrev, S. G. Bardenhagen, P. McMurtry, and G. A. Voth, Biophys. J. **82**, 1226 (2002).

[181] G. Ayton and G. A. Voth, Biophys. J. **83**, 3357 (2002).

[182] G. Ayton, A. M. Smondyrev, S. G. Bardenhagen, P. McMurtry, and G. A. Voth, Biophys. J. **83**, 1026 (2002).

[183] G. Ayton and G. A. Voth, Biophys. J. **87**, 3299 (2004).

[184] J. L. McWhirter, G. Ayton, and G. A. Voth, Biophys. J. **87**, 3242 (2004).

[185] A. P. Lyubartsev and A. Laaksonen, in *Novel Methods in Soft Matter Simulations*, edited by M. Karttunen, I. Vattulainen, and A. Lukkarinen (Springer-Verlag, Berlin, 2004), pp. 219–244.

[186] R. L. Henderson, Phys. Lett. A **49**, 197 (1974).

[187] A. Lyubartsev and A. Laaksonen, J. Phys. Chem. **100**, 16410 (1996).

[188] A. Lyubartsev and A. Laaksonen, Phys. Rev. E **55**, 5689 (1997).

[189] A. P. Lyubartsev, M. Karttunen, I. Vattulainen, and A. Laaksonen, Soft Materials **1**, 121 (2003).

[190] A. Lyubartsev and A. Laaksonen, J. Chem. Phys. **111**, 11207 (1999).

[191] M. Brunner, C. Bechinger, W. Strepp, V. Lobaskin, and H. H. Grünberg, Europhys. Lett. **58**, 926 (2002).

[192] G. C. de León and J. L. Arauz-Lara, Phys. Rev. E **59**, 4203 (1999).

[193] H. Acuña-Campa, M. D. Carbajal-Tinoco, J. L. Arauz-Lara, and M. Medina-Noyola, Phys. Rev. Lett. **80**, 5802 (1998).

[194] H. Meyer, O. Biermann, R. Faller, D. Reith, and F. J. Müller-Plathe, J. Chem. Phys. **113**, 6264 (2000).

[195] M. Tsige, J. G. Curro, G. S. Grest, and J. D. McCoy, Macromolecules **36**, 2158 (2001).

[196] R. Faller and D. Reith, Macromolecules **36**, 5406 (2003).

[197] D. Reith, M. Pütz, and F. J. Müller-Plathe, J. Comput. Chem. **24**, 1624 (2003).

[198] R. L. C. Akkermans and W. J. Briels, J. Chem. Phys. **114**, 1020 (2001).

[199] M. Bathe and G. C. Rutledge, J. Comput. Chem. **24**, 876 (2003).

[200] L. M. S. Loura, A. Fedorov, and M. Prieto, Biophys. J. **80**, 776 (2001).

[201] P. L.-G. Chong, Proc. Natl. Acad. Sci. USA **91**, 10069 (1994).

[202] T. Murtola, E. Falck, M. Patra, M. Karttunen, and I. Vattulainen, J. Chem. Phys. **121**, 9156 (2004).

[203] B. J. Thijsse, M. A. Hollanders, and J. Hendrikse, Computers in Physics **12**, 393 (1998).

[204] P. Jedlovszky and M. Mezei, J. Phys. Chem. B **107**, 5311 (2003).

[205] N. Kikuchi, A. Gent, and J. M. Yeomans, Eur. Phys. J. E **9**, 63 (2002).

[206] E. Pitard, Eur. Phys. J. B **7**, 665 (1999).

[207] T. Ihle and D. M. Kroll, Phys. Rev. E **67**, 066705 (2003).

[208] N. Kikuchi, C. M. Pooley, J. F. Ryder, and J. M. Yeomans, J. Chem. Phys. **119**, 6388 (2003).

[209] E. Allahyarov and G. Gompper, Phys. Rev. E **66**, 036702 (2002).

[210] E. Tüzel, M. Strauss, T. Ihle, and D. M. Kroll, Phys. Rev. E **68**, 036701 (2003).

[211] E. Allahyarov and G. Gompper, Phys. Rev. E **67**, 059901(E) (2003).

[212] T. Ihle and D. M. Kroll, Phys. Rev. E **63**, 020201(R) (2001).

[213] T. Ihle and D. M. Kroll, Phys. Rev. E **67**, 066706 (2003).

[214] T. Ihle, E. Tüzel, and D. M. Kroll, Phys. Rev. E **70**, 035701 (2004).

[215] A. Lamura, G. Gompper, T. Ihle, and D. M. Kroll, Europhys. Lett. **55**, 319 (2001).

[216] A. Lamura, G. Gompper, T. Ihle, and D. M. Kroll, Europhys. Lett. **56**, 768 (2001).

[217] A. Lamura and G. Gompper, Eur. Phys. J. E **9**, 477 (2002).

[218] A. Malevanets and J. M. Yeomans, Comput. Phys. Commun. **129**, 282 (2000).

[219] Y. Hashimoto, Y. Chen, and H. Ohashi, Comput. Phys. Commun. **129**, 56 (2000).

[220] P. Ahlrichs and B. Dünweg, J. Chem. Phys. **111**, 8225 (1999).

[221] A. Malevanets and J. M. Yeomans, Europhys. Lett. **52**, 231 (2000).

[222] S. H. Lee and R. Kapral, Physica A **298**, 56 (2001).

[223] M. Ripoll, K. Mussawisade, R. G. Winkler, and G. Gompper, Europhys. Lett. **68**, 106 (2004).

[224] T. Sakai, Y. Chen, and H. Ohashi, Comput. Phys. Commun. **129**, 75 (2000).

[225] Y. Inoue, Y. Chen, and H. Ohashi, J. Stat. Phys. **107**, 85 (2002).

[226] E. Falck, J. M. Lahtinen, I. Vattulainen, and T. Ala-Nissila, Eur. Phys. J. E. **13**, 267 (2004).

[227] E. Falck, O. Punkkinen, I. Vattulainen, and T. Ala-Nissila, Phys. Rev. E **68**, 050102(R) (2003).

[228] B. Dünweg and K. Kremer, J. Chem. Phys. **99**, 6983 (1993).

[229] B. Maier and J. O. Rädler, Phys. Rev. Lett. **82**, 1911 (1999).

[230] J. P. Flory, J. Chem. Phys. **17**, 303 (1949).

[231] J. M. Vianney and A. Koelman, Phys. Rev. Lett. **64**, 1915 (1990).

[232] S. R. Shannon and T. C. Choy, Phys. Rev. Lett. **79**, 1455 (1997).

[233] J. D. Weeks, D. Chandler, and H. C. Andersen, J. Chem. Phys. **54**, 5237 (1971).

[234] G. S. Gremer and K. Kremer, Phys. Rev. A **33**, 3628 (1986).

[235] S. C. Ying, I. Vattulainen, J. Merikoski, T. Hjelt, and T. Ala-Nissila, Phys. Rev. B **58**, 2170 (1999).

[236] M. Kollmann, R. Hund, B. Rinn, G. Nägele, K. Zahn, H. König, G. Maret, R. Klein, and J. Dhont, Europhys. Lett. **58**, 919 (2002).

[237] M. D. Carbajal-Tinoco, G. C. de León, and J. L. Arauz-Lara, Phys. Rev. E **56**, 6962 (1997).

[238] R. Pesché and G. Nägele, Phys. Rev. E **62**, 5432 (2000).

[239] P. Pesché, M. Kollmann, and G. Nägele, J. Chem. Phys. **114**, 8701 (2001).

[240] P. Pesché, M. Kollmann, and G. Nägele, Phys. Rev. E **64**, 052401 (2001).

[241] B. Rinn, K. Zahn, P. Maass, and G. Maret, Europhys. Lett. **46**, 537 (1999).

[242] J. Santana-Solano and J. L. Arauz-Lara, Phys. Rev. Lett. **87**, 038302 (2001).

[243] J. Santana-Solano and J. L. Arauz-Lara, Phys. Rev. E **65**, 021406 (2002).

[244] K. Zahn, J. M. Méndez-Alcaraz, and G. Maret, Phys. Rev. Lett. **79**, 175 (1997).

[245] H. Aranda-Espinoza, M. Carbajal-Tinoco, E. Urrutia-Banuelo, J. L. Arauz-Lara, and J. Alejandre, J. Chem. Phys. **101**, 10925 (1994).

[246] J. M. Lahtinen, T. Hjelt, T. Ala-Nissila, and Z. Chvoj, Phys. Rev. E **64**, 021204 (2001).

[247] H. Löwen, Phys. Rev. E **53**, R29 (1996).

[248] G. Nägele, Phys. Rep. **272**, 215 (1996).

[249] B. J. Alder and T. E. Wainwright, Phys. Rev. A **1**, 18 (1970).

[250] J. R. Dorfman and E. G. D. Cohen, Phys. Rev. A **6**, 776 (1972).

[251] M. H. Ernst, E. H. Hauge, and J. M. J. van Leeuwen, Phys. Rev. A **4**, 2055 (1971).

[252] M. A. van der Hoef, D. Frenkel, and A. J. C. Ladd, Phys. Rev. Lett. **67**, 3459 (1991).

[253] J. Schofield, A. H. Marcus, and S. A. Rice, J. Phys. Chem. **100**, 18950 (1996).

[254] T. Boublik, Mol. Phys. **29**, 421 (1975).

[255] R. D. Groot and P. B. Warren, J. Chem. Phys. **107**, 4423 (1997).

[256] C. P. Lowe, Europhys. Lett. **47**, 145 (1999).

[257] I. Pagonabarraga, M. H. Hagen, C. P. Lowe, and D. Frenkel, Phys. Rev. E **58**, 7288 (1998).

[258] I. Pagonabarraga, M. H. Hagen, C. P. Lowe, and D. Frenkel, Phys. Rev. E **59**, 4458 (1999).

[259] W. Hess and R. Klein, Adv. Phys. **32**, 173 (1983).

[260] Z. Chvoj, J. M. Lahtinen, and T. Ala-Nissila, J. Stat. Mech.: Theor. Exp. P11005 (2004).